NONLINEAR SPECTROSCOPY OF VANADIUM DIOXIDE

By

José Luis Figueroa Soto

Thesis submitted for the requirements for the degree of

MASTER OF SCIENCE

In

Physics

UNIVERSITY OF PUERTO RICO

MAYAGÜEZ CAMPUS

2016

Approved by:

Sergiy Lysenko, Ph.D. President, Graduate Committee	Date
Pablo J. Marrero, Ph.D. Member, Graduate Committee	Date
Héctor J. Jiménez, Ph.D. Member, Graduate Committee	Date
Carlos Marín, Ph.D. Representative of Graduate Office	Date
Rafael A. Ramos, Ph.D. Chairperson of the Department	Date

To my mother, for always being there to support my endeavors, and for making me the man I am today…

To my father, for showing me how to be a responsible person and taking pride in my accomplishments…

To the rest of my family members and friends for supporting me along the way…

Acknowledgments

I would like to give my most sincere thanks to my advisor Dr. Sergiy Lysenko for taking me as his student since my undergraduate days. He has undertaken the challenge that is guiding a graduate student through the process that has led to this moment. Thanks for imparting your knowledge unto me, I could not have asked for a better mentor. To the graduate members of the committee, Dr. Pablo Marrero and Dr. Héctor Jiménez, their advice is greatly appreciated. To Dr. Félix Fernández, whenever I had a doubt he was always there to answer my questions, and most importantly for providing the XRD analysis. To Dr. Armando Rúa for providing the samples that where the foundation of this work, my thanks. To Alfredo Moreu, his expertise in the area of mechanical engineering is one indispensable tool for this work. Thank you for being a good counselor and a friend.

Finally I would like to thank all of my graduate student friends. Thanks for making these last three years full of fun and good memories.

Abstract

Phase-change materials such as vanadium oxides show strong photorefractive effect on ultrashort time scale which makes these materials attractive for prospective optoelectronic applications such as bistable ultrafast optical switchers and memory. This work is focused on Z-scan study of laser beam self-diffraction and ultrafast angle-resolved light scattering of vanadium oxides. Thin films of vanadium oxides were grown by pulsed laser deposition. "Continuum Nd:YAG" picosecond laser and femtosecond "Spectra-Physics" laser system was used for nonlinear optical measurements. Upon light excitation, vanadium oxide compounds undergo reversible electronically-driven insulator-to-metal phase transition. Strong photo-refraction is caused by rapid change of lattice symmetry, by generation of dense electron-hole plasma and by strong photo-acoustic response. Thus, the lattice symmetry of vanadium dioxide changes from monoclinic to tetragonal on the time scale ranging from hundred femtoseconds to several tens of picoseconds, depending on intensity, duration and wavelength of the optical excitation. Optical constants and effective values of third-order nonlinear susceptibility were obtained using optical Z-Scan technique in closed and open aperture scanning mode. Measurements of nonlinear transmittance in the far field through a finite aperture reveal two-component optical nonlinearity due to Kerr Effect and due to phase transition during the photo-excitation time. Using the standard approach, we obtain effective values of nonlinear index of refraction n_2, nonlinear absorption coefficient and the third order non-linear susceptibility $\chi^{(3)}$. Hemispherical angle-resolved light scattering is used for a statistical analysis of the phase transition process. Evolution of scattering indicatrix, fractal dimension, surface power spectral density, and surface autocorrelation function shows a distinctive behavior which gives a clear understanding on the influence of structural defects, twinning of microcrystallites and domain formation during the phase transition.

Resumen

Materiales que poseen transición de fase, tales como óxidos de vanadio muestran un fuerte efecto foto refractivo en la escala de tiempos ultracortos que hace que estos materiales sean candidatos óptimos para aplicaciones optoelectrónicas tales como conmutadores ópticos ultrarrápidos biestables y memorias. Este trabajo se enfoca en la técnica de escaneo óptico Z para el estudio de la auto difracción causada por un láser. Además se estudió la dispersión de la luz por medio de la técnica ultra rápida ángulo resuelta para óxidos de vanadio. Las películas delgadas de óxidos de vanadio fueron fabricadas por deposición de láser pulsado. Se utilizó un sistema laser de picosegundos "Continuum Nd:YAG" y un sistema láser de femtosegundos "Spectra-Physics" para las mediciones ópticas no lineales. Tras la excitación de luz, compuestos de óxido de vanadio experimentan una transición reversible aislante-metal la cual es accionada electrónicamente. Fuerte foto-refracción es causada por el rápido cambio de simetría en la red cristalina del material, por generación de un denso electrón-hueco plasma y por una fuerte respuesta foto-acústica. Por lo tanto, la simetría de la red cristalina del dióxido de vanadio se ve sometida a un cambio de estructura monoclínica a tetragonal en la escala de tiempo que varía de cien femtosegundos a varias decenas de picosegundos, dependiendo de la intensidad, duración y longitud de onda de la excitación óptica. Las constantes ópticas y valores efectivos de la susceptibilidad eléctrica no lineal de tercer orden fueron obtenidas a partir de la técnica de escaneo óptico Z en el modo de exploración de abertura cerrada y abierta. Las mediciones de transmitancia no lineal en el campo lejano a través de una abertura finita revelan alinealidad óptica de dos componentes debido al efecto Kerr óptico y debido a la transición de fase durante el tiempo de foto excitación. Utilizando el enfoque estándar, se obtuvieron valores efectivos para el índice de refracción no lineal n_2, el coeficiente de absorción non lineal y la susceptibilidad eléctrica de tercer orden no lineal $\chi^{(3)}$. La técnica de ángulo semiesférica de dispersión de luz por resolución temporal se utiliza para un análisis estadístico del proceso de transición de fase. Evolución de la indicatriz de dispersión, la dimensión fractal, la densidad espectral de potencia de la superficie, y la función de auto-correlación de superficie muestra un comportamiento distintivo que da una comprensión clara de la influencia de defectos estructurales, y la formación de dominios durante la transición de fase.

Copyright ©

By

José L. Figueroa Soto

Table of Contents

Chapter 1 Introduction 1

1.1 Motivation 1

1.2 $VO2$ Crystal Structure 2

1.3 Literature Review 5

Chapter 2 Theory 24

2.1 Basic formulation of Nonlinear Optics 24

2.1.1 Interaction of Light and Propagation through a Medium 24

2.1.2 Nonlinear Optical Media 25

2.1.3 Description of Nonlinear Optical Interactions: Third Harmonic Generation 26

2.1.4 Intensity Dependent Refractive Index 27

2.1.5 Self-Focusing of Light 29

2.1.6 Two Photon Absorption 30

2.2 Z-Scan Technique 31

2.2.1 Z-Scan Theory 33

2.3 Scattering Data and Surface Statistics 35

Chapter 3 Methodology 39

3.1 Thin Film Fabrication by PLD 39

3.2 Crystal Structure 40

3.3 Reflection Measurements 40

3.4 Z-Scan Setup 41

3.5 Laser System 43

3.6 Scattering 44

Chapter 4 Results and Discussion 46

4.1 Beam waist radius measurements 46

4.2 X-Ray Diffraction 47

4.3 Angular Dependence of Reflection Measurements 49

4.4 Z-Scan Results for VO_2/SiO_2 Thin Films 51

4.5 Z-Scan Results for VO_2/Al_2O_3 Thin Films in Insulating and Metallic Phase 66

4.6 Scattering Results for VO_2/Al_2O_3 (R-cut and C-cut) 82

4.7 Ultrafast Light Scattering Results for VO_2/Al_2O_3 and VO_2/SiO_2 Thin Films 88

Chapter 5 Conclusion 92
Appendix 94
A.1 Beam waist radius parameter extraction program 94
A.2 Power, Intensity and Fluence extraction program 96
A.3 Z-scan parameter extraction program 97
Biblipography 99

List of Figures

Figure 1.1 Monoclinic structure (M_1) of VO_2 2

Figure 1.2 Rutile structure of VO_2. Red denotes vanadium atoms and blue denotes oxygen atoms. 3

Figure 1.3 Unit cell of VO_2 crystal. Dashed lines represent monoclinic cell while solid lines represents the tetragonal cell 4

Figure 1.4 (a) Measured Z-scan of a 1mm thick CS_2 sample using 300 ns pulses at wavelength 10.6 μm indicating thermal self-defocusing. (b) Measured Z-scan of a 2.4 mm thick BaF_2 sample using 27 ps pulses at wavelength 532 nm, indicating self-focusing due to electronic Kerr effect 8

Figure 1.5 Third order nonlinear susceptibility vs peak pump power for insulator VO_2 at $T = 295\ K$ 14

Figure 1.6 (a) $|\chi^{(3)}|$ as a function of peak intensity of the interference field in the film. (b) $|\chi^{(3)}|$ as a function of particle radius 15

Figure 2.1 Third harmonic generation. (a) Geometry of the interaction. (b) Energy-level description. 26

Figure 2.2 Self-focusing representation for a material with a positive nonlinear index of refraction. 30

Figure 2.3 Diagram of two photon absorption 30

Figure 2.4 Diagram of Z-scan method. D1 and D2 are the detectors in which the ratio $D2/D1$ are recorded as a function of the samples position. 31

Figure 3.1 Schematic of a PLD system 39

Figure 3.2 Schematic view for reflection measurements for thin films 41

Figure 3.3 Schematic drawing of Z-Scan setup built in the laboratory……………………..………42

Figure 3.4 PY61C-10 Laser schematic and layout……………………………………….……44

Figure 3.5 Experimental setup for hemispherical angle-resolved light scattering measurements. ……………………………………………………………………………………………45

Figure 4.1 The profile at focal plane and Gaussian fit for laser beam with wavelength $\lambda = 532\ nm$…………………………………………………………………………..............…46

Figure 4.2 X-ray diffraction patterns of VO_2 films of different thickness deposited on amorphous SiO_2 substrates. (a) is for the 35 nm thick film and (b) is for the 95 nm thick film.…………………………………………………………………….……………………47

Figure 4.3 X-ray diffraction counts vs azimuthal orientation for VO_2/Al_2O_3 (A-cut) thin film.……..…...48

Figure 4.4 Angular dependence of the reflectance for two polarizations for VO_2/SiO_2 at λ=532. (a) is for 35 nm thick film, (b) is for 75 nm thick film and (c) is 95 nm thick film. Symbols are experimental data and lines are calculated reflectance from fit………………………………..…49

Figure 4.5 Closed aperture Z-scans for VO_2/SiO_2 thin films at different laser fluences. (a) is for a 35 nm thick film at room temperature, (b) is for a 75 nm thick film at room temperature and (c) is for a 95 nm thick film at room temperature……………………………………………………52

Figure 4.6 Open aperture Z-scans for VO_2/SiO_2 thin films at different laser fluences. (a) is for a 35 nm thick film at room temperature, (b) is for a 75 nm thick film at room temperature and (c) is for a 95 nm thick film.……………………………………………………………...............54

Figure 4.7 Graphs of both $\Delta\Phi_0$ and ΔT_{p-v} as a function of fluence for VO_2/SiO_2 thin films. (a) is for the 35 nm thin film, (b) is for the 75 nm thin film and (c) is for the 95 nm thin film. …………….……………………………………………………….............................57

Figure 4.8 Graphs of Rayleigh range parameter z_0 for open and closed aperture as a function of fluence for VO_2/SiO_2 thin films. (a) is for the 35 nm thin film, (b) is for the 75 nm thin film and (c) is for the 95 nm thin film. ……………………………………………………………59

Figure 4.9 (a) Graph of nonlinear index of refraction $\gamma\ (m^2/W)$ for the 35 nm thick sample. (b) Graph of $n_2eff(esu)$ and real part of the third order susceptibility $Re\chi^{(3)}(esu)$ as a function of fluence for the 35 nm thick sample…………………………………………………………61

Figure 4.10 (a) Graph of nonlinear index of refraction $\gamma\ (m^2/W)$ as a function of fluence for the 95 nm thick sample. (b) Graph of both $n_2eff(esu)$ and $Re\chi^{(3)}(esu)$ as a function of fluence for the 95 nm thick sample. (c) Graph of both $|\chi^{(3)}|$ and $Im\chi^{(3)}(esu)$ as a function of fluence for the 95 nm thick sample……………………………………………………………………..64

Figure 4.11 (a) Graph of closed aperture Z-scan trace at room temperature for VO_2/Al_2O_3 (M-Cut). (b) Graph of closed aperture Z-scan trace at room temperature for VO_2/Al_2O_3 (M-Cut)………..67

Figure 4.12 (a) Closed aperture Z-scan for metallic VO_2 on $Al_2O_3(M - cut)$. (b) Open aperture Z-scan for metallic VO_2 on $Al_2O_3(M - cut)$..68

Figure 4.13 (a) Graph of closed aperture Z-scan trace at room temperature for VO_2/Al_2O_3 (A-Cut). (b) Graph of closed aperture Z-scan trace at room temperature for VO_2/Al_2O_3 (A-Cut)..70

Figure 4.14 (a) Closed aperture Z-scan for metallic VO_2 on $Al_2O_3(A - Cut)$. (b) Open aperture Z-scan for metallic VO_2 on $Al_2O_3(A - Cut)$..72

Figure 4.15 $\Delta\Phi_0$ and ΔT_{p-v} as a function of fluence at room temperature for VO_2/Al_2O_3 (a) is for the M-cut thin film, (b) is for the A-cut thin film..73

Figure 4.16 Rayleigh range fitting constantz_0 for both open and closed aperture as a function of fluence at room temperature for VO_2/Al_2O_3 (a) is for the VO_2/Al_2O_3 (M-cut) thin film, (b) is for the VO_2/Al_2O_3 (A-cut) thin film..74

Figure 4.17 (a) Graph of nonlinear index of refraction γ (m^2/W) and $n_2eff(esu)$ as a function of fluence for the VO_2/Al_2O_3 (M-cut) sample below the PT temperature. (b) Graph of the third order nonlinear susceptibility $\chi^{(3)}(esu)$ as a function of fluence for the VO_2/Al_2O_3 (M-cut) sample below the PT temperature...76

Figure 4.18 (a) Nonlinear index of refraction γ (m^2/W) and $n_2eff(esu)$ as a function fluence for the VO_2/Al_2O_3 (M-cut) sample in its metallic state. (b) Third order nonlinear susceptibility $|\chi^{(3)}|(esu)$ as a function of fluence for the VO_2/Al_2O_3 (M-cut) sample in its metallic state.......77

Figure 4.19 (a) Graph of nonlinear index of refraction γ (m^2/W) and $n_2eff(esu)$ as a function of fluence for the VO_2/Al_2O_3 (A-cut) sample below the PT temperature. (b) Graph of the third order nonlinear susceptibility $|\chi^{(3)}|(esu)$ as a function of fluence for the VO_2/Al_2O_3 (A-cut) sample below the PT temperature...79

Figure 4.20 (a) Nonlinear index of refraction γ (m^2/W) and $n_2eff(esu)$ as a function fluence for the VO_2/Al_2O_3 (A-cut) sample in its metallic state. (b) Third order nonlinear susceptibility $|\chi^{(3)}|(esu)$ as a function of fluence for the VO_2/Al_2O_3 (A-cut) sample in its metallic state.......80

Figure 4.21 (a) Temperature dependent evolution of light scattering indicatrix for 30 nm thick film VO_2/Al_2O_3 (R-cut). Arrow marks square like pattern at $T = 296\ K$. (b) Power spectral density of the surface at $T = 296\ K$. Central and periphery region was reconstructed using the Gerchberg-Saxton ER algorithm. 82

Figure 4.22 Light scattering for VO_2/Al_2O_3 C-cut thin films. (a) log(BSDF) for 50 nm thick film in insulating and metallic state. (b) log(BSDF) for different areas of 30 nm thick film. Dashed lines indicate preferential directions of scattering..83

Figure 4.23 Morphology of the 30 nm thick film of VO_2/Al_2O_3 (R-cut). (a) $2x2\mu m^2$ AFM topography and (b) $2x2\mu m^2$ surface autocorrelation function ACF_{AFM}. Periodical fringes are marked by dashed lines. (c) Power spectrum extracted from AFM and light scattering data at $T =$

$296\,K$. Dashed lines are fit from equation (2.35). The inset shows a cross section of 2D ACF_{AFM}……………………………………………………………………………………….….84

Figure 4.24 Evolution of scattering pattern and PSD of the surface roughness for the 30 nm thick VO_2/Al_2O_3 R-cut. (a) Cross sections of the BSDF scattering indicatrix and PSD_s at $\varphi = 0^{\circ}$. Inset shows the azimuthally averaged PSD_s function for insulating and metallic phases. Dashed lines are fit. (b) The relative change $\Delta BSDF(T)/BSDF_0$ near the PT point, where $BSDF_0$ is obtained for insulating phase and $\Delta BSDF(T) = BSDF(T) - BSDF_0$. Arrows mark the region of noticeable emergence of diffraction peaks. ……………………………………………………………..........86

Figure 4.25 (a) Autocorrelation function of VO_2 surface for insulating phase at T=296 K and metallic phase (T=353 K). (b) Cross section of ACF_S distribution at different temperatures. Upper inset shows oscillatory component of ACF_s. Lower inset shows evolution of autocorrelation length versus temperature. ……………………………………………………………………….....87

Figure 4.26 Thermally induced BSDF indicatrix for (a) VO_2/Al_2O_3 and (b) VO_2/SiO_2 thin films ……………………………………………………………………….……………………..…..89

Figure 4.27 Relative change $\Delta BSDF(t)/BSDF(0)$ of the scattering signal upon light induced PT for (a) VO_2/Al_2O_3 and (b) VO_2/SiO_2 thin films; $\Delta BSDF(t) = \Delta BSDF(t) - \Delta BSDF(0)$………89

Chapter 1 Introduction

1.1 Motivation

Phase change materials such as metal oxides present many opportunities for applications due to their scientific importance in the field of condensed matter physics [1]. Of great importance is VO_2, whose phase transition characteristics were first discovered by Morin in 1959 [2]. With its unique transformation of structural, electronic and optical properties above room temperature VO_2 has been the subject of many studies [3]. It undergoes an insulator to metal phase transition (PT) at $T_c = 340.15\ K$. During this PT, VO_2 undergoes a lattice transformation from monoclinic phase with crystallographic space group C_{2h}^5 to a tetragonal phase of group D_{4h}^{14}. Accompanied by this phase transition is a change in VO_2 properties, such as conductivity, optical constants and magnetic susceptibility [4]. Despite several studies made on the material, the understanding and origin of the phase transition still eludes scientists and is far from a complete understanding. It was demonstrated that this transition and structural rearrangement occurs in a very short time scale of less than $500\ fs$ [5]. Such changes in the material characteristics make it a suitable candidate for practical applications such as light controlled solid state optical switchers and diffractive elements, ultrafast light controlled electronic devices, among others [4].

The main focus of this work is the use of Z-scan technique introduced by Bahae *et al.* [6] using a picosecond laser to characterize the absorptive and refractive nonlinearities presented in VO_2 thin films of varying thickness and substrate. Closed and open aperture Z-scan measurements allow to extract non-linear optical constants in order to have a better understanding of the third

order nonlinear electrical susceptibility $|\chi^3|$ which contains important information concerning optical electron behavior at high energy excitation [7]. In addition, the use of a hemispherical angle-resolved light scattering technique is used for a statistical analysis of the phase transition process. From angle-resolved measurements the power spectral density and autocorrelation function are obtained near the phase transition temperature. A precise calculation of the Power Spectral Density (PSD) and Autocorrelation (ACF) is possible using the Gerchberg-Saxton error reduction algorithm.

1.2 VO_2 Crystal Structure

As previously stated, VO_2 has a monoclinic structure at room temperature and undergoes a phase transition above $T = 340\ K$ and changes its crystal structure to tetragonal. Figure 1.1 shows the monoclinic M1 structure of VO_2 with crystallographic space group $P2_1/c$ (C_{2h}^5 No.14) [8].

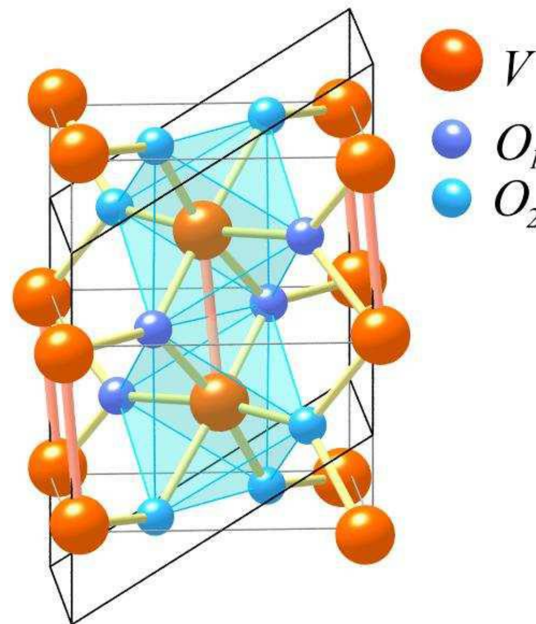

Figure 1.1 Monoclinic structure (M1) of VO_2 [8].

From Longo *et al*. [9] the lattice constants and angle reported values are $a_{M_1} = 5.7517$ Å, $b_{M_1} = 4.5378$ Å, $c_{M_1} = 5.3825$ Å and $\beta_{M_1} = 122.646^{\circ}$. Figure 2.2 shows the rutile structure of metallic VO_2 with a tetragonal lattice of space group $P4_2/mnm$ (D_{4h}^{14}, No. 136) [8].

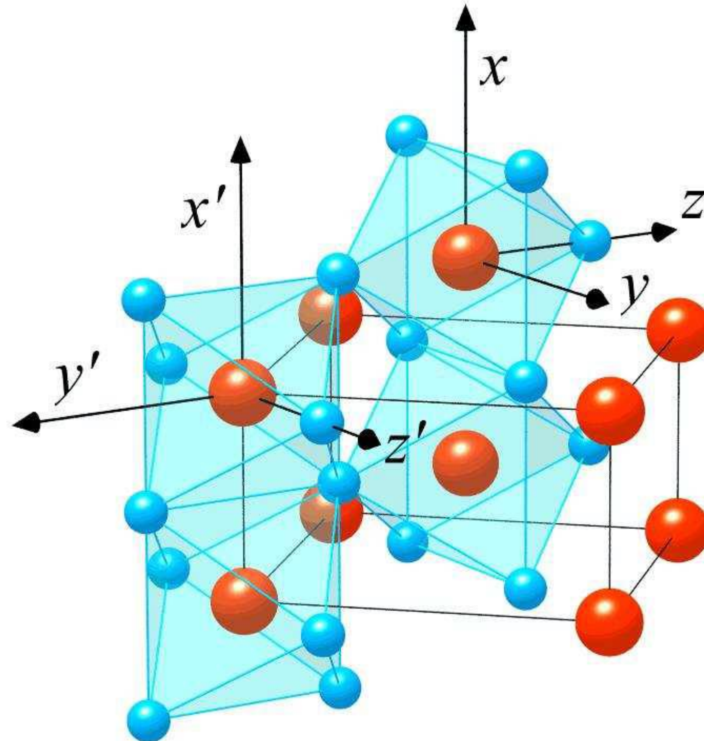

Figure 1.2 Rutile structure of VO_2. Red denotes vanadium atoms and blue denotes oxygen atoms [8].

The lattice parameters and the internal oxygen parameters are given by $a_t = b_t = 4.58$ Å, $c_t = 2.8528$ Å , $u = 0.30000$ with all axial angles measuring 90° as presented by Wentzcovitch *et al*. [10]. Figure 1.3 shows the crystallographic planes for monoclinic VO_2. Once the PT is induced, one has to take into account the small twist of the unit cell, the a_t and the c_t directions

from the figure coincide with b_m and a_m. As can be noted from the figure, the a_m, c_m, b_t and c_t axes are located in the same plane (010) [4].

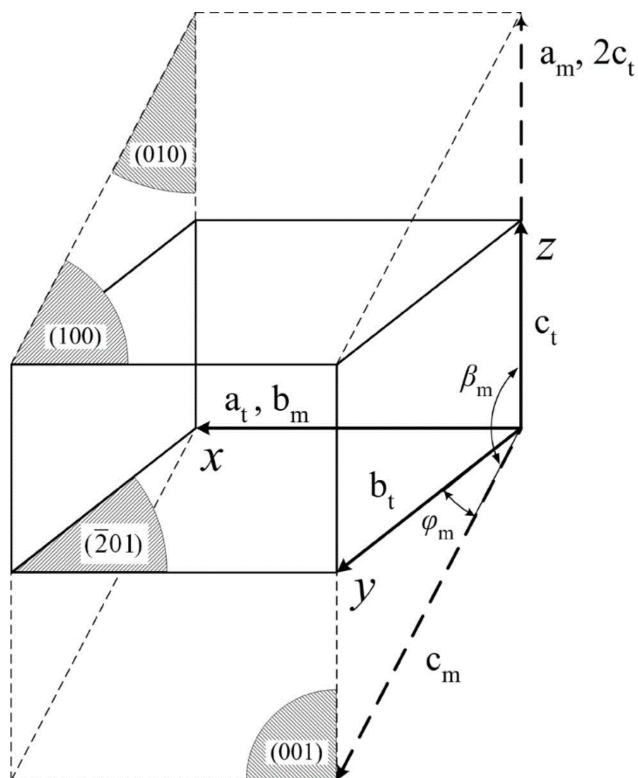

Figure 1.3 Unit cell of VO_2 crystal. Dashed lines represent monoclinic cell while solid lines represent tetragonal cell [4].

1.3 Literature Review

Since as early as the 1950's studies on transition oxides have been of much interest. One of the first studies on vanadium oxides and titanium oxides conducted by Morin *et al.* suggested that these types of materials behave like metals under particular circumstances [2]. The reason for this was because the oxides at the beginning of the 3d series, the nonbonding (t_{2g}) orbitals, extend out far enough to overlap and form a narrow conduction band. To further validate this idea, the researchers reported conductivity measurements made on polycrystalline titanium oxides (TiO) and on single crystals of vanadium oxides (VO, VO_2, V_2O_3) and suggested a model to further explain the transition phenomenon. Morin *et al.* indicate that the reason vanadium oxides are insulators below the transition temperature is related to the fact that each set of bands contains three lower states per atom which are full and three higher states per atom which are empty.

Verleur *et al.* conducted a study to determine the optical constants of VO_2 single crystals and thin films below and above the phase transition temperature [11]. The optical properties of VO_2 were studied in the range of 0.25 to 5 eV and reflectivity and transmission spectra were measured as well. Even though some difference in magnitude was reported for the values of the dielectric constant from both thin films and single crystals, the structural features were in good agreements. It was found that below the transition temperature T_t, VO_2 shows four prominent absorption peaks centered near photon energies of 0.85, 1.3, 2.8, and 3.6 eV. Above T_t, metallic free-carrier absorption is observed below 2.0 eV, and the same absorption peaks observed near 2.8 and 3.6 eV were present. Such results were consistent with the picture in which filled bands that arise from oxygen $2p$ orbitals are separated by approximately 2.5 eV from partially filled bands arising primarily from vanadium $3d$ orbitals.

One of the first ever reported light induced insulator to metal phase transition of VO_2 was made by Roach et al. Using a Q-switched ruby laser, the researchers were able to induced and detect the transition of VO_2 thin films within 20 ns [12]. Not only was this the fastest optically induced I-M PT that is associated with a crystallographic phase transition, but also the first attempt to induce the IM PT in the transition metal oxides by direct carrier excitation. From the results obtained from the optical data, it is apparent that the principle effect of irradiating the VO_2 thin films with ruby laser photons was to excite electrons from the valence d band to the conduction d band. It was also shown that the fast phase transition is induced by photon-electron-phonon energy transfer process.

Further studies on the dynamics of vanadium oxides, especially vanadium dioxide, were performed by Bugaev *et al* [13]. They monitored the reflection coefficient of the film, whose variation was attributed to the development of the PT. They also detected anisotropy in the coefficient of reflection when excited by a picosecond pulse. In order to verify that this phenomenon was not the result of interference interaction of the excited and probing beams, further experiments where conducted. They varied the ratio of the exciting and probing beam, but found the same results. The proposed mechanism for this observed phenomenon is the formation of electron-hole drops (EHD) in the semiconducting phase of VO_2 induced by the powerful pumping pulse. During the drops formation process, the liquid drop with a metallic conductivity is located in the electric field of the light wave. The appearance of the electrostriction effect causes a deformation of the EHD or a stretch along the direction of the electric field.

In order to have a more in depth knowledge on the studies of the phase transitions dynamics of VO_2, Cavalleri *et al.* [5] used femtosecond pulses to probe both structural and electronic dynamics during the PT. The observed phase transition at sub-picosecond levels into the high rutile

phase of the material along an insulator-to-metal transition was observed. Such a fast transition at such time scale may suggest that it may not be entirely initiated by a thermal contribution. It was reported that the solid-solid transformation lasts only a few femtoseconds and is reversible.

Since phase transition dynamics are accompanied by a change in the optical constants of the material, it is of high interest to characterize and identify the change that occurs during this PT. Among different techniques to characterize the materials such as degenerate four-wave mixing to obtain the third order electrical susceptibility, as well as pump and probe reflection measurements among others, there is Z-scan technique, used to obtain the nonlinear optical properties of the material. Proposed by Sheik-Bahae *et al.* [6] in the late 1980's, using a single beam technique, the nonlinear index of refraction n_2 and the nonlinear absorption coefficient β were measured for several materials. For this the transmittance of the sample was measured through a closed or open aperture in the far field as a function of the propagation path z of a focused Gaussian beam. It is shown that for many practical cases, non-linear refraction and its signs can be obtained from a simple linear relationship between the observed transmittance changes and the induced phase distortion without the need of complicated calculations. In other words, the nonlinear refractive index and nonlinear absorption coefficients were obtained directly from the Z-scan data without the need of computer fits. Measurements for non-linear refraction were made for a number of different materials such as CS_2, BaF_2 and $ZnSe$. These were performed using a picosecond Nd:YAG laser and a nanosecond TEA CO_2 laser, both set at different wavelengths ranging from $532nm$, $1.06\mu m$ and $10.6\mu m$. For the case of CS_2, the same value for the non-linear index of refraction was obtained at the three different wavelengths using picosecond pulses. It is reported that because of its simplicity, the technique will become a valuable tool for researchers searching for highly non-linear materials.

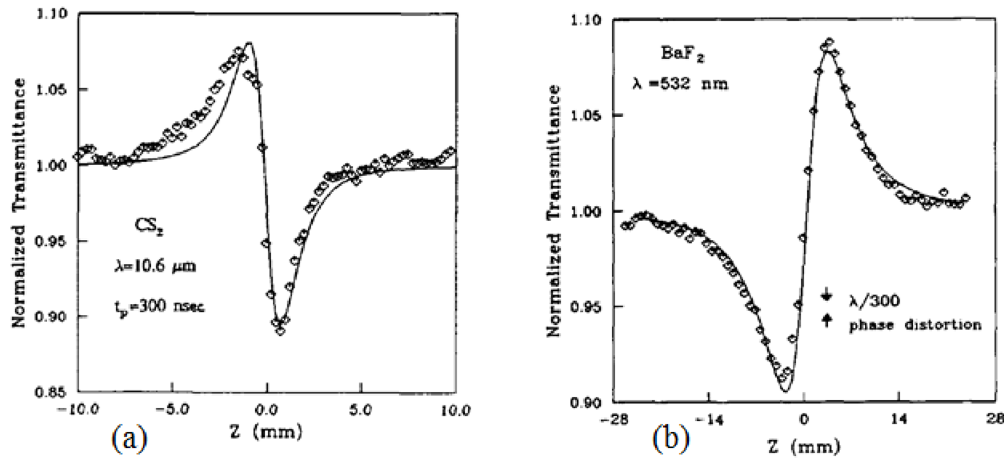

Figure 1.4 (a) Measured Z-scan of a 1mm thick CS_2 sample using 300 ns pulses at wavelength 10.6 μm indicating thermal self-defocusing. (b) Measured Z-scan of a 2.4 mm thick BaF_2 sample using 27 ps pulses at wavelength 532 nm, indicating self-focusing due to electronic Kerr effect [6].

Since the third order electrical susceptibility $\chi^{(3)}$ contains important electrical behavior upon high energy laser excitation, it is also of significance in order to characterize the material. Studies conducted by Liu *et al.* [14] on VO_2 thin films show results for their optical properties by absorption and photoluminescence measurements. They also showed the first ever large polarizability and slow excited state dynamics with the use of degenerate four-wave mixing technique using a 30 ps Nd;YAG laser. A value of $\chi^{(3)}$ in the order of 10^{-10} esu was found for VO_2. This large susceptibility and polarizability is believed to be related to the large offset in the potential well minima between the ground and excited states, supporting the observation by Cavalleri *et al.* [5] where the optically induced PT may not be thermally induced.

Studies conducted on the nonlinear optical properties of VO_2 single crystals by Petrov *et al.* studied the behavior of the third order harmonic optical signal generated from the surface of the material [15]. Using 50 fs pulses and a wavelength of $\lambda = 1250$ nm, the researchers were able

to demonstrate a significant increase in the intensity of the third order harmonic in VO_2 near the phase transition temperature. From the temperature dependent measurements a hysteresis behavior of the phase transition on a microscopic scale was observed. They were also able to show the extremely fast time scale of the phase transition in the order of less than 50 fs.

Using time resolved near-edge X-ray absorption, Cavalleri et al. was able to directly measure the photo-induced insulator to metal phase transition in VO_2 [16]. Using picosecond pulses originating from synchrotron radiation, a detection of the redshift in the vanadium L_3 edge at 516 eV was done. This redshift is associated with the transient collapse of the low temperature band gap. A two component temporal response was also identified, thus corresponding to an ultrafast transformation over a 50 nm surface layer, followed by a 40 m/s thermal growth of the metallic phase in the bulk.

Further studies on the nonlinear optical limiting properties for vanadium oxides were performed by Xu *et al.* [17]. The researchers characterized vanadium oxide nanotubes for the visible an infrared light, and also presented their results from dispersion of the nanotubes in water suspensions and in thin films. They showed that the VO_x nanotubes exhibit strong optical-limiting at a wavelength of 532 nm, but no nonlinear behavior was observed for wavelengths of 1064 nm. The suggested mechanism is that of two photon absorption for the observed nonlinearity at $\lambda = 532nm$.

Using Z-scan technique and pump-probe measurements, Lopez *et al.* [18] compared the ultrafast optical nonlinearities for both VO_2 nanoparticles and thin films in their respective insulating and metallic phase. For their insulating phase both VO_2 nanoparticles and films exhibit the typical self-focusing z-scan trace with a positive nonlinear index of refraction. Moreover, they

presented that the nonlinear effects are larger for the nanoparticles which also revealed a saturable nonlinear absorption. Lopez *et al*. also showed that in the metal phase the VO_2 thin films exhibit a self-defocusing effect and a negative nonlinear index of refraction, but for nanoparticles the nonlinear index was still positive. They also presented equivalent values for both γ and β for thin films at room temperature and at 100 ℃ where they found $\gamma^{22\,℃} = -7.1 \pm x10^{-12}\, cm^2/W$ and $\gamma^{100\,℃} = 7.5 \pm x10^{-12}\, cm^2/W$ using a 120 fs duration pulse. Again the change of sign for the nonlinear index can be seen. An equivalent value for the nonlinear absorption coefficient was found to be $\beta^{22\,℃} = 270 \pm 30\ \ cm/GW$.

Further studies on the dielectric properties of thin VO_2 films in the terahertz frequency range were conducted by Jepsen *et al.* near the vicinity of the I-M phase transition. Using THz spectroscopy they were able to measure the high frequency conductivity during the phase transition in VO_2 [19]. By measuring both the frequency dependent transmission amplitude and phase shift, they were able to follow the gradual growth of conductive domains as the temperature increased near and above the phase transition temperature. The researchers observed that the changes of the dielectric properties at THz frequencies occur at significantly higher temperatures than in the visible range. The transmission amplitude also switches at a slightly higher temperature than the phase shift of the transmitted light. The experimental data obtained was compared with the proposed models for the evolution of the phase transition.

Studies on the monoclinic and correlated metal phase to further study the transition dynamics of VO_2 were conducted by Kim *et al*. using femtosecond pump-probe measurements. They were able to see the appearance of coherent phonon oscillations at 4.5 and 6.0 THz, thus indicating that the rutile metal phase of VO_2 does not occur at the same time as the first order metal to insulator PT [20]. The first order metal to insulator PT is driven not by the structural phase

transition, but by hole carriers in VO_2 and occurs between transient triclinic and monoclinic and correlated metal. The characteristics of this MCM need to be studied in more depth.

Grinolds *et al*. reported direct imaging and diffraction of VO_2 films by using 4D ultrafast electron microscopy with combined spatial and temporal resolutions [21]. From UEM they were able to obtain snapshot images by using timed, single-electron packets, and the ability to obtain a sequence of snapshots or movies with atomic scale spatial resolution and ultrashort temporal resolution. From these spatial and temporal resolution snapshots, the researchers were able to study the ultrafast metal-insulator phase transition of VO_2. They were able to observed structural changes from one phase to the other in a transition characterized by hysteresis. From the temporal changes of the images they were able to illustrate the size selectivity of the first order phase transition on the nanometer scale. Changes in the diffraction patterns provide the atomic scale structural determination.

More studies on the four dimension visualization of translational structures in phase transitions by electron diffractions were performed by Baum *et al*. on VO_2 single crystals [22]. They show the ability to decipher the nature of the atomic motions during a structural phase transition. For VO_2 crystals, the elementary steps follow a non-concerted mechanism with a sequence of translational structures. These translational structures first involve local displacements on the fs and ps time scale followed by long-range shear rearrangements on the sub-ns time scale and at the speed of sound. The initial step of the VO_2 insulator to metal PT is the V-V bond dilation, which provides a dynamical molecular picture.

By tracing the multi THz conductivity of VO_2 during the I-M PT triggered by a 12 fs light pulse. Kübler *et al*. was able to spectrally discriminate femtosecond dynamics of lattice and

electron degrees of freedom [23]. In the earliest stage, the dynamics initiated by the fs pulse starting in the dielectric phase closely resembles the local excitation of molecular V-V dimers into an antibonding state; thus, triggering a coherent wave packet motion of the stretching vibration. Based on this, a qualitative model for the non-thermal phase transition was proposed.

Using optical-pump terahertz-probe spectroscopy, Hilton *et al*. investigated the near-threshold behavior of the photo-induced I-M transition in VO_2 thin films [24]. Near the transition temperature T_c a reduction in the fluence required to drive the IM transition was observed. This observation is consistent of a softening of the insulating state due to an increasing metallic volume fraction. This coexistence of phases facilitates the growth of a homogeneous metallic conducting phase following superheating via excitation. A simple model was proposed to describe the observed initial condition sensitivity.

The light induced insulator to metal phase transition in VO_2 thin films deposited on a single crystal sapphire and amorphous glass substrates was studied by Lysenko *et al*. [4]. It was shown that VO_2 films deposited on crystalline substrates are highly ordered and show a noticeable anisotropy in the optical response upon the phase transition. On the other hand, optical and structural properties are dependent on the shear plane for the sapphire deposited VO_2 films. Also the VO_2 dielectric susceptibility is described via a proposed model. The concept of the $V-O-V$ charge transfer is considered as a major process that contributes to both the linear and non-linear dielectric susceptibility. It was also noted that the PT dynamics are dependent on the film morphology and structural defects.

A continuation of the study on the PT and recovery process in VO_2 deposited on substrates with different thermal conductivities was performed for a time scale ranging from 10^{-11} to 10^{-9}.

The study showed that the contribution on the PT dynamics by the thermal effect due to phonon absorption is small compared to the effect by electronic mechanism on the sub-nanosecond time scale [25]. During the recovery process of metal to insulator after laser excitation, a contribution of both the thermal and non-thermal was identified for the thin film when irradiated at different fluences. Considerably different recovery dynamics was observed depending on the substrate the VO_2 was deposited on.

Non-linear optical properties of VO_2 were studied using the degenerate-four-wave-mixing technique, ultrafast optical pump-probe reflection and scattering [7]. Different measurements for the third order non-linear electrical susceptibility were taken at different excitation powers. At low excitation (below ~ 2 mJ/cm^2) the light induced PT recovery dynamics was shown to be purely governed by electronic rather than thermal contribution. The third order non-linear susceptibility was measured by DFWM technique at a wavelength of 400 nm for thin VO_2 films with varying thicknesses and morphology and was found to be in the order of $10^{-9}\ esu$. It was found that for VO_2 films in the metallic phase the value of $\left|\chi^{(3)}\right|$ was lower in comparison to the insulator phase. It was also noted that above a peak pump power higher than $\sim 10^{10}\,\frac{W}{cm^2}$ the value of $\left|\chi^{(3)}\right|$ for the insulating phase started to decrease. This was attributed to the motion of atoms which in turn alters the linear and non-linear dielectric susceptibility.

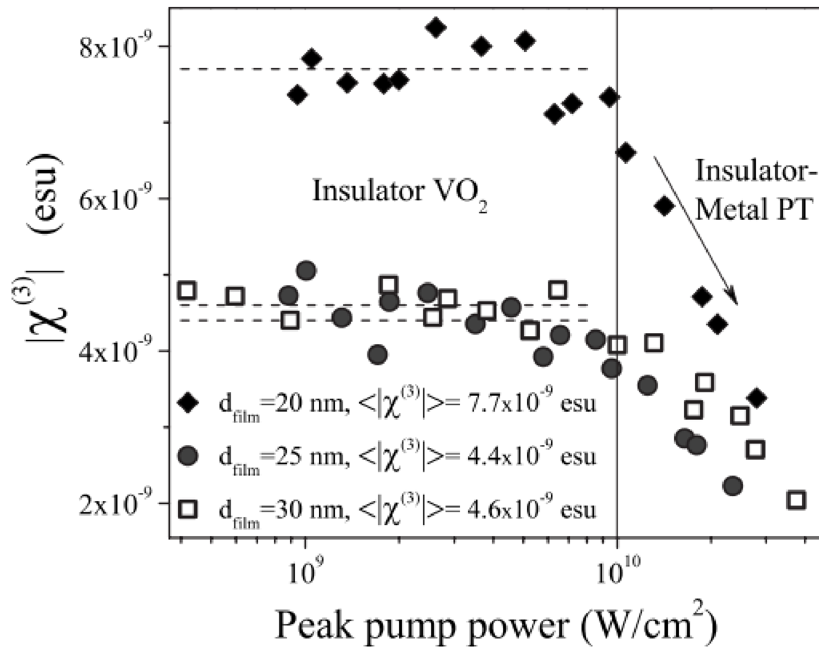

Figure 1.5 Third order nonlinear susceptibility vs peak pump power for insulator VO_2 at $T = 295\ K$ [7].

Further studies of nanostructured VO_2 were performed using femtosecond pump-probe technique [26]. A dependence on the size of nanoparticles and the film morphology was found to be critical for the PT dynamics. This size dependence also affects the third order nonlinear susceptibility at different excitation levels. A reported value for $\chi^{(3)}$ was in the order of $10^{-8}\ esu$ in comparison to Liu *et al.* $10^{-10}(esu)$ [14]. It was also found that the rate of structural phase transition increases due to a confinement effect as the particle size decreases. A formation of metastable VO_2 was found when nucleation of the metallic state occurred. A kinetic model for the metallic rate growth and transient grating evolution was also developed for the VO_2 thin films.

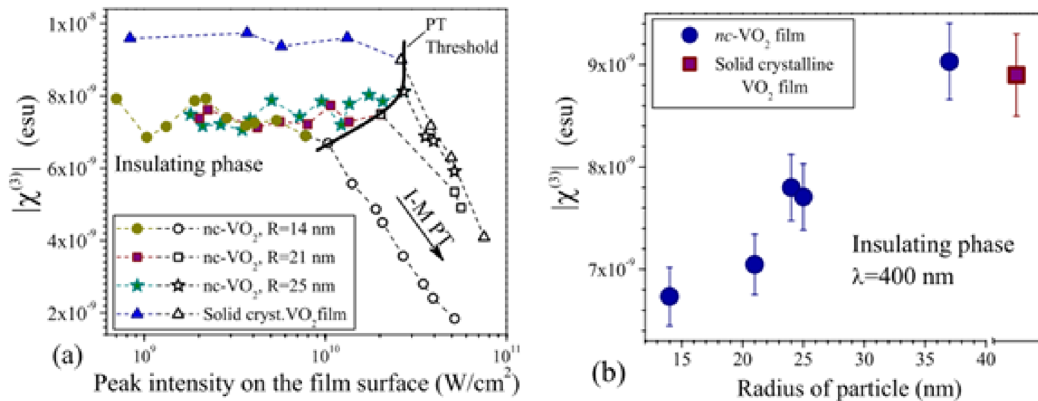

Figure 1.6 (a) $\left|\chi^{(3)}\right|$ as a function of peak intensity of the interference field in the film. (b) $\left|\chi^{(3)}\right|$ as a function of particle radius. [26].

Nakamija *et al*. reported the ultrafast response to the photoexcitation for VO_2 single crystals and thin films using optical-pump THz probe technique at room temperature [27]. From the optical excitation, an ultrafast decrease of the transmittance of the THz radiation within 0.7 ps was observed. This decrease of transmittance was assigned to the appearance of high electronic conductivity due to free carriers. An increase of ten times was observed for the conductivity in the picosecond time scale after photo-excitation, and it was concluded that the electronic states are metallic.

Using static and time resolved X-ray diffraction Hada *et al.* was able to measure the lattice motion and displacement in the unit cell in VO_2 grown on c-cut Al_2O_3 [28]. From these measurements the researchers were able to observe the monoclinic tetragonal phase transition of the VO_2 unit cell and the twist motion of vanadium atoms in the unit cell. Using a high repetition femtosecond laser, time resolved XRD measurements were obtained. The results suggest that the unit cell of the low temperature monoclinic VO_2 transformed into the high temperature tetragonal

phase extremely fast, within 25 ps. Despite this fast transition, the atoms in the unit cell fluctuated or vibrated about the center of the tetragonal coordinates, within 100 ps.

Using THz probe pulses, Pashkin *et al*. studied the ultrafast photo-induced I-M phase transition in VO_2 at different temperatures and excitation fluences [29]. From the spectrally resolved mid-infrared response, they were able to separately trace the dynamics of lattice and electronic degrees of freedom with a time resolution of 40 fs. The influence of the fluence which drives the system into a long-lived metallic state is found to increase with decreasing temperature. From all measurements, they were able to observe a modulation of the eigenfrequencies of the optical phonon modes induced by their anharmonic coupling to the coherent wave packet motion of V-V dimers at 6.1 THz. From the electronic response they saw a weak quadratic coupling due to the coherent dimer oscillating resulting in a modulation of the electronic conductivity at twice the frequency of the wave packet motion.

Hada *et al.* reported the photoexcitation of metallic phase vanadium dioxide VO_2 from time resolved X-ray diffraction measurements [30]. They found that throughout the photoexcitation, the metallic phase VO_2 transitioned to the similar transient state, which they reported in the insulator to metallic phase transition in the time scale of approximately 10 ps. The transient state was accomplished only by photoexcitation and not by thermal excitation.

Recently, Kürüm *et al*. [1] studied the nonlinear optical characteristics of amorphous vanadium oxide thin films using both Z-scan technique and pump-probe. Using Z-scan, the researchers were able to extract the nonlinear absorption coefficient β for a 50 nm thick VO_x thin film. A self-defocusing closed aperture Z-scan was observed for both nanosecond and picosecond pulses. No phase transition was observed at the irradiated fluences; thus, the sample was treated

as a semiconductor. Both open aperture scans for both pulses showed saturable absorption for different intensities, but the picosecond scans showed nonlinear absorption at different intensities as well. It was found that the nonlinear absorption coefficient increases with decreasing input intensity.

A similar study performed by Wang *et al.* [31] studied the nonlinear optical properties of VO_2 with a low phase transition temperature of 29 ℃. Using Z-scan with Ti: Sapphire laser pulses, they were able to induce the phase transition. Their nanostructured VO_2 thin films exhibit two photon absorption and a self-defocusing closed aperture scan was indicative of a negative nonlinear index of refraction when the phase transition was induced. They attributed these high nonlinearities to excitation of the electronic subsystem.

Recently, Tao *et al*. reported that VO_2 single crystal microbeams placed over insulated substrates or metal grids exhibit different behaviors. Using optical, TEM and ultrafast electron diffraction experiments, they showed different behaviors with structural and metal-insulator transitions occurring at the same temperature for insulating substrates [32]. Similarly for metallic substrates they demonstrated that a new monoclinic metal phase lies between the insulating and metallic phase. From the experiments the structural and electronic phase transitions are strongly first order.

Further studies on the ultrafast phase transition dynamics of VO_2 were carried out by Cocker *et al.* using time-resolved THz spectroscopy [33]. A phase diagram of critical pump fluence versus temperature for the insulator to metal PT in VO_2 was established for the first time for a broad range of temperatures down to 17 K. They also report that the phase transition process in a non-thermal one. A critical threshold model for the ultrafast photo-induced transition based

on a critical density of electrons and a critical density of coherently excited phonons is proposed. The observed THz dynamics above the photo-induced PT threshold reveal nucleation and growth of metallic nanodomains over pico second time scales.

Recently, Wall *et al.* showed that a time dependent change in the coherent phonon spectrum can probe a change in symmetry of the lattice potential [34]. This in turn is able to provide an all optical probe of structural transitions. They examined the photo-induced structural phase transition of VO_2 and showed that above the PT threshold, photoexcitation changes the lattice potential on an ultrafast timescale. The fact that a loss of the equilibrium-phase phonon modes occurs promptly, indicates a non-thermal pathway for the photo-induced PT.

More studies on the photoinduced insulator-metal transition in VO_2 using broadband time-resolved reflection spectroscopy were conducted to separate the response of the lattice vibrations from the electronic dynamics and to observe their evolution [35]. When VO_2 was excited above the photoinduced PT threshold, they found that the restoring forces that describe the ground-state monoclinic structure are lost during the excitation process. This suggest that the ultrafast change in the lattice potential drives the structural transition. From pump-probe measurements during the non-equilibrium transition, they reported that the electronic properties of the material evolve on a different lower time scale. This suggests that the early state of VO_2 after photoexcitation is a nonequilibrium state, defined neither by the insulating or metallic state.

Recently, van Veenendaal explained the occurrence of the I-M PT in VO_2 after photoexcitation [36]. From the photoexcitation a coherent motion of the V-V dimers is induced, thus affecting the electronic structure. After closing of the band gap, electron-electron scattering equilibrates the electron densities. If the electron density exceeds a critical value, a phase transition

occurs to the metallic state. The proposed model could be applied to other transition metal oxides such as V_2O_3.

Liu *et al*. recently reported a conical scanning dark field imaging technique in four dimensional ultrafast electron microscopy. With the technique, the researchers were able to visualize single-particle dynamics of a polycrystalline ensemble undergoing phase transition [37]. Of main interest was the use of this technique for the metal-insulator phase transition of VO_2, induced by laser excitation and followed by taking electron-pulsed, time-resolved images and diffraction patterns. The single particle selectivity was achieved by identifying the origin of all constituent Bragg spots on Debye-Sherrer rings from the ensemble. From the diffraction patterns, the orientation mapping and dynamic scattering simulation was obtained for the monoclinic and tetragonal phase during the transition. In turn, this confirms the behavior that Bragg spots change with time. With increasing particle size, the threshold temperature for phase recovery also increased. This observation was further validated by a theoretical model developed for single particle phase transitions.

Combining ultrafast pump-probe spectroscopy with a diamond anvil cell to decouple the I-M electronic transition from the lattice symmetry, Hsieh *et al*. studied the phase transition of VO_2 [38]. From coherent phonon spectroscopy, the researchers were able to track the photo-excited phonon vibrational frequencies of the low temperature, monoclinic insulating phase that transitions into the metallic phase. They also found that at high pressure, the coherent phonons of the monoclinic phase are still clearly observed upon the photo driven phase transition to the metallic state.

Using femtosecond time-resolved photoelectron spectroscopy Wegkamp *et al*. studied the I-M phase transition of VO_2. From both experimental and theoretical results, the researchers observed the collapse of the band gap in its insulating phase upon photoexcitation due to carrier doping [39]. This revealed ultrasensitivity of VO_2 to variations of the screening by holes at the top of the V valence bands. The collapse of the band gap is then followed by a hot carrier relaxation in the transient metallic phase on a 200 fs time scale. These new insights into the phase transition of VO_2 provide a new perspective into the mechanisms of the phenomenon.

Recently, Appavoo *et al*. demonstrated the use of a mesh of gold nanoparticles acting as a plasmonic photocathode. This was done to induce an ultrafast phase transition in nanostructured VO_2 upon illumination by a femtosecond laser pulse. Due to the optical excitation, hot electrons are created and injected ballistically across the Au/VO_2 interface to induce a subpicosecond phase transition in VO_2 [40]. From theoretical calculations, the researchers showed that upon injecting electrons, this leads to a collapse of the 6 THz phonon mode. This catastrophic collapse of the phonon mode is associated with the phase transition.

A recent study by Lysenko *et al*. [41] on the ultrafast light scattering imaging of multi-scale transition dynamics in VO_2 views the use of angle resolved light scattering with pump-probe spectroscopy to shed some light upon the statistical processes in VO_2 and to further study the dynamics of the material. The approach revealed anisotropic and grain size dependent behavior with high resolution in both space and time. As previously stated by Cavalleri, light induce phase transition occurs within 500 fs, but is dependent on the grain sizes of VO_2 which show different transition rates [5]. A higher rate is found for clusters with lower concentrations of structural defects and deformation. Twinning in VO_2 is also observed for the thermally induced transition

but not observed for the ultrafast light induced transition. Phase coexistence is observed as well during the thermally induced transition.

To further study the nonequilibrium electronic structures of VO_2 thin films upon photoexcitation, Yoshida *et al.* implemented 170 fs pulses with a fluence above $\sim 6\, mJ/cm^2$ to induce the phase transition. They observed that the phase transition is accompanied by a spectral-weight redistribution over a 1 eV scale [42]. This in turn suggests that the phase transition in VO_2 is of an ultrafast nature. They also found that there is an anomalous spreading of the spectral weight near the Fermi level, the reason for this being the spectral broadening due to phonon excitations during the transient process. A presence of phonon excitations on an ultrafast time scale may be attributed to the transient metallic state.

The photo-induced insulator to metal phase transition versus surface statistics of VO_2 was studied by the angle-resolved ultrafast light scattering technique [43]. In order to make a statistical analysis of the non-equilibrium processes for VO_2 epitaxial films a Gerchberg-Saxton error reduction algorithm was applied to calculate the surface autocorrelation function and to reconstruct the power spectral density function of the surface from light scattering data. The study revealed that the transition dynamics are dependent on VO_2 grain size and that transition rate depends on the optical absorption and orientation of the grains with respect to the polarization of the pump pulse. A complex multistage transformation of VO_2 lattice gives rise to a stepwise evolution of surface autocorrelation length and transient anisotropy of the scattering field.

More studies on the ultrafast phase transition of VO_2 were conducted by Mayer *et al*. where they directly traced the near and midinfrared transmission changes of a VO_2 thin film [44]. The nonthermal switching of VO_2 into a metastable metallic state is governed solely by the amplitude

of the applied THz field. Below the threshold fluence, no signature of excitonic self-trapping is observed. Their findings are consistent with the generation of spatially separated charge pairs and a cooperative transition into a delocalized metallic state by the THz induced tunneling.

Recently, Grupp *et al*. demonstrated for the first time the I-M phase transition in VO_2 thin films induced by high field multi THz waveform of 200 nm grown by PLD [45]. They observed sub-100 fs switching timescales and coherent lattice dynamics in VO_2, thus supporting a nonthermal and initially electronic scenario of the field induced phase transition. The degree of metallization is determined by the strength of the electric field and can be described by a tunneling mechanism.

Doping VO_2 with tungsten (W) changes the modulation characteristics of the phase transition. Using time-resolved THz spectroscopy with picosecond time scale, Xiao *et al.* showed that doping slows down the photo induced I-M PT dynamic process in VO_2 thin films [46]. It also reduces the pump fluence threshold for the PT. Besides observing the broadening of the PT temperature, W doping prevents metallic phase domains from percolation. From extracting carrier properties from photo-induced THz conductivity at several transition times, it was found that the electron-electron correlation during the PT is enhanced with W doping.

Using terahertz time domain spectroscopy, Lourembam et al. study the conductivity mechanism in the metastable layered polymorph VO_2 (B) thin films [47]. The appearance of a non zero Drude term in the complex conductivity above 240 K, indicates the evolution from a pure insulating phase to a metallic state. The well-known conductivity of the $VO_2(M_1)$ is fitted by modification of the Drude model to include backscattering. Two different THz conductivity regimes separated by temperature for these two phases of VO_2. From the electronic phase diagram,

it is revealed that the width and onset of the metal-insulator transition in the B phase develops differently from the M_1 phase.

Hemispherical angle-resolved light scattering measurements were performed to provide statistical analysis of the thermally induced Metal Insulator phase transition [3]. Results indicated that thermal hysteresis is strongly correlated on the spatial frequency of surface irregularities. A variation of scattering indicatrix is seen, where it is dependent on the sample's morphology and it varies depending on the thickness of the films. On thin films a higher internal elastic strain was observed, whereas thicker films showed presence of misfit dislocations. Distinctive qualitative changes during the PT were also noted. For example, at T_c disorder of the film reaches a higher level due to the coexistence of both insulator and metallic phases. It also shows more uniform optical properties and smoothness when in its metallic phase in comparison to its insulating phase.

Chapter 2 Theory

2.1 Basic formulation of Nonlinear Optics

2.1.1 Interaction of Light and Propagation through a Medium

To understand the basis of non-linear optics we begin with a quantitative description of the interaction of light with a bulk material based on Maxwell's equations. For a molecular medium, such as an organic crystal or polymeric solid, is generally regarded as non-conducting and non-magnetic and the electrons are regarded as being tightly bound to the nuclei. To explain the interaction of light with this type of media we usually regard them within the frame work of a dielectric subjected to an electric field [48]. This type of approach is referred to as the dipole approximation since the charge distribution induced in the molecule by the field is approximated to that of an induced dipole with moment equal to

$$\mu_{induced} = -e\vec{r} \qquad (2.1)$$

where e is the electron charge and r is the electric field induced displacement. Such induced dipole gives rise to a bulk polarization of the form

$$P = -Ner \qquad (2.2)$$

where N is the electron density in the medium. Inside of the material the electric field is lowered by the polarization that opposes the externally applied electric field. The reduction of field intensity is within the desired volume element containing the molecule is by a factor of $1 + \varepsilon$, where ε is defined as the dielectric constant of the medium. For the case where the field is low, the polarization of the medium is linear and is expressed in terms of the electric susceptibility $\chi^{(1)}$ by

$$\vec{P} = \chi^{(1)} \cdot \vec{E}\,, \qquad (2.3)$$

where this proportionality constant is related to the dielectric constant by

$$n_0^2 = \varepsilon = 1 + 4\pi\chi^{(1)}\,. \qquad (2.4)$$

The quantity $\chi^{(1)}$ is a second-rank tensor that relates all of the components of the polarization vector to all the components of the electric field vector [48].

Both the refractive index and the dielectric constants are complex quantities. Near a resonance corresponding to an electronic absorption, the complex index of refraction is given by

$$n_c = n + ik \qquad (2.5)$$

Where the real part n accounts for refraction while the imaginary part ik, describes the absorption of light in the dielectric medium. In the case of a linear optical medium, the refractive index is independent of the electric field strength [48].

2.1.2 Nonlinear Optical Media

For the case when the medium is subject to an intense electric field such as one from an intense laser pulse, the polarization response of the material is not linear (described by 2.3). For this case, one can express the polarization P in a time t dependent power series of the field strength E as

$$P(t) = \chi^{(1)}E(t) + \chi^{(2)}E^2(t) + \chi^{(3)}E^3(t) + \cdots +$$

$$\equiv\ P^{(1)}(t) +\ P^{(2)}(t) +\ P^{(3)}(t) \qquad (2.6)$$

Here the quantities $\chi^{(2)}$ and $\chi^{(3)}$ are the second and third order nonlinear susceptibilities, respectively $P^{(2)}(t)$ and $P^{(3)}(t)$ are known as the second and third order nonlinear polarizations.

In the case of second order nonlinear optical interactions, they only occur in non-centrosymmetric crystals or crystal that do not display inversion symmetry. Since liquids, gases, amorphous solids and many types of crystals present inversion symmetry, therefore $\chi^{(2)}$ vanishes for this type of media and as a consequence cannot produce second-order nonlinear optical response [49]. But for third order nonlinear optical interactions $\chi^{(3)}$, they can occur for both centrosymmetric and non-centrosymmetric media alike.

2.1.3 Description of Nonlinear Optical Interactions: Third Harmonic Generation

Considering the case of the third order contribution to the nonlinear polarization, we consider the simpler case in which the applied field is monochromatic and is given by

$$E(t) = E_0 \cos(\omega t) \qquad (2.7)$$

where ω is the angular frequency. The nonlinear polarization can be expressed as

$$P^{(3)}(t) = \frac{1}{4}\chi^{(3)}E_0^3 \cos(3\omega t) + \frac{3}{4}\chi^{(3)}E_0^3 \cos(\omega t) \qquad (2.8)$$

The first term from the equation describes a response at frequency 3ω that is the result of an applied field of frequency ω. Such effect leads to third harmonic generation.

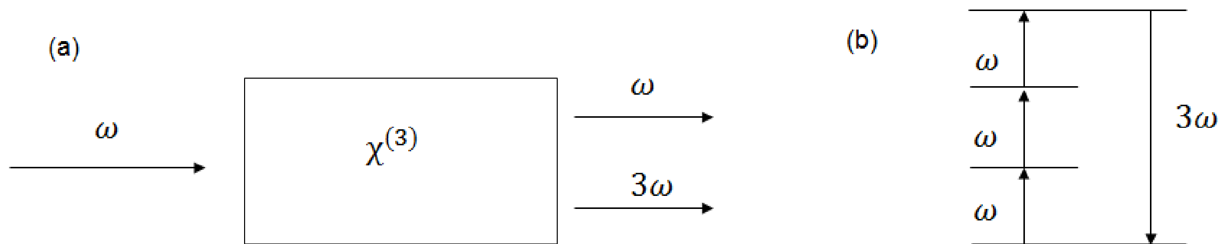

Figure 2.1 Third harmonic generation. (a) Geometry of the interaction. (b) Energy-level description.

From part (b) of figure 2.1, three photons of frequency ω are destroyed and one photon of frequency 3ω is created. The second term from equation (2.8) describes a nonlinear contribution to the polarization at the frequency of the incident field. Due to this, this term leads to a nonlinear contribution to the refractive index experienced by a wave at frequency ω.

2.1.4 Intensity Dependent Refractive Index

The refractive index of many materials depends upon the intensity of the light used to measure the index of refraction. For many materials the index of refraction can be described by the relation

$$n = n_0 + \bar{n}_2 \langle E^2 \rangle \,, \qquad (2.9)$$

Here n_0 denotes the usual, weak field index of refraction and $\bar{n}_2$ is a different optical constant that gives the rate at which the refractive index increases with increasing optical intensity [49]. If the optical field is of the form

$$E(t) = E(\omega)e^{-i\omega t} + constant \qquad (2.10)$$

then the time average is

$$\langle E(t)^2 \rangle = 2E(\omega)E(\omega)^* = 2|E(\omega)|^2 \,, \qquad (2.11)$$

so we can express equation (2.9) as

$$n = n_0 + 2\bar{n}_2 |E(\omega)|^2 \,. \qquad (2.12)$$

This change in the refractive index is known as the optical Kerr effect, where the refractive index of the material changes by an amount that is proportional to the square of the strength of an applied electric field.

The linear and nonlinear index of refractions are related to the linear and nonlinear susceptibilities by

$$n_0 = (1 + 4\pi\chi^{(1)})^{1/2} \qquad (2.13)$$

and respectively

$$\bar{n}_2 = \frac{3\pi}{n_0}\chi^{(3)} \qquad (2.14)$$

In the past discussion it has been assumed that the refractive index has been measured using only a single laser beam.

An alternate way of expressing the intensity dependent refractive index is by

$$n = n_0 + \gamma I\,. \qquad (2.15)$$

Here I denotes the time averaged intensity of the optical field and is given by

$$I = \frac{n_0 c}{2\pi}|E(\omega)|^2\,. \qquad (2.16)$$

For this case, we are assuming that the refractive index is a measure of two separate beams. The presence of a strong beam of amplitude $E(\omega)$ leads to a modification of the refractive index experienced by a weak probe wave of amplitude $E(\omega')$. Since the total refractive index n must be the same using either a single beam or two beams, we have that

$$2\bar{n}_2|E(\omega)|^2 = \gamma I\,. \qquad (2.17)$$

Hence,

$$\gamma = \frac{4\pi}{n_0 c}\bar{n}_2\,. \qquad (2.18)$$

Using equation (2.14) we find that

$$\gamma = \frac{12\pi^2}{n_0^2 c}\chi^{(3)}\,. \qquad (2.19)$$

This term is once again related to optical Kerr effect which correspond to the light intensity dependent refractive index and is potentially important for all high speed optical switching functions and devices.

2.1.5 Self-Focusing of Light

Self-focusing of light is a process in which an intense beam of light modifies the optical properties of a material medium such that it causes the beam to come into focus within the material as shown in figure 2.2. For this case, we have assumed that n_2 is positive. The laser beam induces a refractive index variation inside of the material, thus having a larger index of refraction at the center of the material than at its periphery. This effect is the same as a positive lens. This effect is known as a self-action effect or an effect in which a beam of light modifies its own propagation by means of the nonlinear response of the material [49].

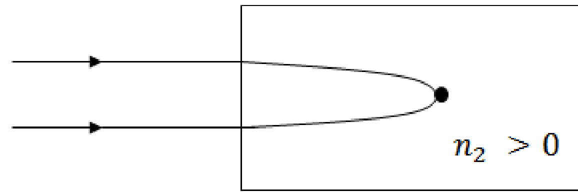

Figure 2.2 Self-focusing representation for a material with a positive nonlinear index of refraction.

2.1.6 Two Photon Absorption

Two photon absorption is the process in which an atom makes a transition from its ground state to an excited state by the simultaneous absorption of two laser photons as shown in figure 2.3. This nonlinear process occurs at relatively high optical intensities. Here absorption coefficient is proportional to the light intensity as

$$\alpha = \alpha_0 + \beta I \qquad (2.20)$$

where α_0 and β are the linear and nonlinear absorption coefficients, correspondingly. Two photon absorption is a useful spectroscopic tool for determining the positions of energy levels that are not connected to the atomic ground state by a one photon transition.

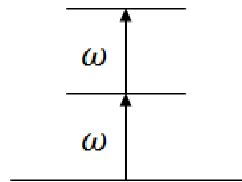

Figure 2.3 Diagram of two photon absorption.

2.2 Z-Scan Technique

Introduced by Sheik-Bahae *et al* [6], Z-scan is a method based on self-focusing to measure the sign as well as the magnitude of $\chi^{(3)}$. Before the introduction of Z-scan, measurements of nonlinear refraction and $\chi^{(3)}$ included nonlinear interferometry, degenerate four-wave mixing, ellipse rotation. Z-scan technique is based on the principles of spatial beam distortion, and offers high sensitivity. In order for Z-scan to be successful, a pure Gaussian beam must be tightly focused by a lens and passed through the nonlinear medium to be studied. The transmittance of the nonlinear medium is measured as a function of the samples position z with respect to the focal plane as shown in figure 2.4.

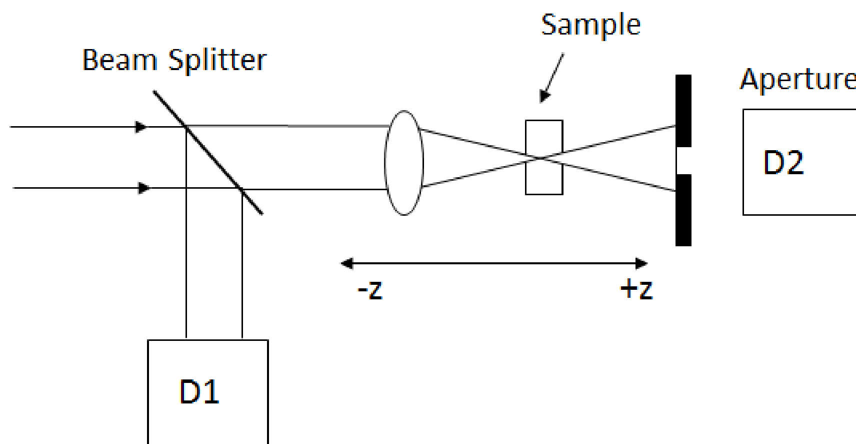

Figure 2.4 Diagram of Z-scan method. D1 and D2 are the detectors in which the ratio $D2/D1$ are recorded as a function of the samples position.

The simplest example of Z-scan technique is, for instance, a material that is known to have a negative nonlinear index of refraction and a thickness that is smaller than the diffraction length of the focused beam ($L \ll z_0$). Such a sample can be treated as a thin lens of variable focal length. Starting the z-scan from a distance far away from the focus, the beam intensity is low and

negligible nonlinear refraction occurs, thus the transmittance remains relatively constant. As the sample is brought closer to the focal point, the beam intensity increases, thus leading to self-focusing of the sample. For example, a self-defocusing prior to focus will collimate the beam, thus causing the beam to become narrower, therefore resulting in an increase of the transmission measured $(D2/D1)$. As the sample passes the focal plane, the same self-defocusing increases the beam divergence, leading to broadening of the incident beam at the aperture and thus a decrease in transmittance. Therefore, there should be a null at the moment the sample crosses the focus. This is similar as placing a lens at or near the focus, resulting in minimal or no change of the far-field pattern. Once the sample crosses the focal plane and gets farther the scan is complete such that the transmittance becomes constant again. The signature of such Z-scan trace is the pre-focal peak (maximum transmittance) and post-focal valley (minimum transmittance) of a negative nonlinear index of refraction. Having a positive nonlinear index of refraction would give rise to a valley-peak Z-scan trace.

For this explanation of Z-scan, purely refractive nonlinearity is taken into consideration assuming there is no absorptive nonlinearities. Examples of absorptive nonlinearities are the case of two photon absorption where the peak is suppressed and we see an enhancement of the valley or saturation where we see the opposite effect as in two photon absorption. For that reason, there is a necessity to always use an aperture. Such sensitivity to nonlinear refraction is due to the aperture, removal of the aperture eliminates nonlinear refraction. Eliminating such aperture will in turn make the Z-scan sensitive to nonlinear absorption. Thus from such scans without aperture or open aperture scans, one can extract the nonlinear absorption coefficient.

2.2.1 Z-Scan Theory

We will now demonstrate the basis on how to analyze Z-scan data according to Sheik-Bahae *et al* [6]. For a Gaussian beam with beam waist radius w_0 and traveling along the z direction, the electric field is given by

$$E(z,r,t) = E_0(t)\frac{w_0}{w(z)} \,.\exp\left[-\frac{r^2}{w^2(z)} - \frac{ikr^2}{2R(z)}\right] e^{-\varphi(z,t)}\,, \quad (2.21)$$

where $w^2(z) = w_0^2(1 + z^2/z_0^2)$ is the beam radius, $R(z) = z(1 + z_0^2/z^2)$ is the radius of curvature at the wave front and $z_0 = \frac{\pi w_0^2}{\lambda}$ is the Rayleigh range. The term $e^{-\varphi(z,t)}$ contains all the radially uniform phase variations. This can be expressed as

$$\Delta\varphi(z,r,t) = \Delta\varphi_0(z,t) exp\left(-\frac{2r^2}{w^2(z)}\right) \quad (2.22)$$

with the changes for $\Delta\varphi_0$ as

$$\Delta\varphi_0(z,t) = \frac{\Delta\Phi_0(t)}{1 + z^2/z_0^2}\,. \quad (2.23)$$

$\Delta\Phi_0(t)$ is the on-axis phase shift at the focus and is defined as

$$\Delta\Phi_0(t) = k\gamma I_0(t) L_{eff} \quad (2.24)$$

with $L_{eff} = (1 - e^{-\alpha L})/\alpha$, where L is the sample's length and α is the linear absorption coefficient. Here γ is the nonlinear index of refraction and I_0 being the on-axis irradiance at the focus.

We now need to find an expression for the transmittance in order to solve for $\Delta\Phi_0(t)$. The transmitted power at the aperture can be expressed as

$$T(z) = \frac{\int_{-\infty}^{+\infty} P_T\big(\Delta\Phi_0(t)\big)\, dt}{S\int_{-\infty}^{+\infty} P_i(t)dt} \qquad (2.25)$$

where P_T is the transmitted power at the aperture, P_i is the instantaneous input power and $S = 1 - \exp(-2r_a^2/w_a^2)$ is the aperture linear transmittance. With w_a being the radius of the beam at the aperture and it depends on how the radius is changed by nonlinear refraction. For a given $\Delta\Phi_0$, the magnitude and shape of $T(z)$ do not depend on the wavelength or geometry as long as the detector's distance is larger than the Rayleigh range z_0 and if the aperture S is small enough ($S = 0$) then the difference between the normalized peak and valley transmittance can be defined such that

$$\Delta T_{p-v} \approx 0.406|\Delta\Phi_0| \qquad (2.26)$$

for $|\Delta\Phi_0| \le \pi$. Also given the far-field condition is met and the sample's length is smaller than the Rayleigh range, the normalized transmittance for a closed aperture scan is described by the following equation

$$T(z, \Delta\Phi_0) = 1 - \frac{4\Delta\Phi_0 x}{(x^2+9)(x^2+1)} \qquad (2.27)$$

where $x = z/z_0$. Once $\Delta\Phi_0$ is known, one can extract γ from equation (2.24). Similarly for an open aperture scan the transmittance is given by

$$T(z, q_0) = \frac{ln\left[1 + \frac{q_0}{1+x^2}\right]}{\left(\frac{q_0}{1+x^2}\right)} \qquad (2.28)$$

where the term $q_0 = \beta I_0 L_{eff}$ contains β, the nonlinear absorption coefficient. By virtue of knowing the nonlinear index of refraction and the nonlinear absorption coefficient one can compute the third order susceptibility $|\chi^{(3)}|$ by the following relations

$$Re\chi^{(3)}(SI) = \frac{4\epsilon_0 c n_0^2 \gamma}{3}\ (SI) \tag{2.29}$$

$$Im\chi^{(3)}(SI) = \frac{2\epsilon_0 c^2 n_0^2 \beta}{3\omega}\ (SI) \tag{2.30}$$

Here we present such quantities in the international system of units (SI), yet for convenience we change them to the more conventional electrostatic unit of charge (esu) by the following conversion

$$Im\chi^{(3)}\ (esu) = \frac{9x10^8\ Im\chi^{(3)}(SI)}{4\pi} \tag{2.31}$$

$$Re\chi^{(3)}\ (esu) = \frac{9x10^8 Re\chi^{(3)}(SI)}{4\pi} \tag{2.32}$$

Finally, using equations (2.31) and (2.32) the magnitude of $|\chi^{(3)}|$ can be obtained as

$$|\chi^{(3)}| = \left|(Re\chi^{(3)})^2 + (Im\chi^{(3)})^2\right|^{1/2} \tag{2.33}$$

2.3 Scattering Data and Surface Statistics

Using angle-resolved light scattering technique one can obtain statistical information about surface irregularities of different sizes. Since each scattering angle corresponds to specific spatial frequency of the surface $f = 1/d = \sin(\theta/\lambda)$, where θ is the polar scattering angle and d is the

characteristic size of irregularities. Using this technique one can collect the scattering images from the samples and use this data to calculate the bidirectional scatter distribution function (BSDF), power spectral density function (PSD), and for reconstruction of autocorrelation function (ACF) of the surface. These functions reflect general statistical properties of the surface [43].

The BSDF can be directly calculated from angle-resolved light scattering by the following relation

$$BSDF(\theta,\varphi) = \left(\frac{dI_{scatt}(\theta,\varphi)}{d\Omega}\right)\frac{1}{I_0 cos\theta} \qquad (2.34)$$

where I_0 is the intensity of incident light, dI_{scatt} is the intensity of light scattered into solid angle $d\Omega$, and φ is the azimuthal angle. The relation between BSDF measured at normal incidence and PSD is given by

$$PSD(f) = \frac{\lambda^4\, BSDF(f)}{16\pi^2 Q\, cos\theta} \qquad (2.35)$$

where Q is an optical factor that depends on light polarization, scattering angle, and dielectric constants. The PSD function represents the statistical distribution of surface roughness versus surface spatial frequency.

The information on the correlation of surface irregularities can be obtained from the ACF

$$ACF(r) = \lim_{L\to\infty}\frac{1}{L}\int_L z(r')z(r'+r)dr' , \qquad (2.36)$$

where r is the translation length in the surface plane, and $z(r)$ is the surface profile defined over an area L. At zero translation, $ACF(0) = \delta^2$, where δ is the rms roughness. The normalized auto correlation function $ACF_s = ACF/\delta^2$ is calculated from scattering data.

The Wiener-Khinchin theorem shows that the ACF is a Fourier transform of the PSD

$$ACF(r) = \int_{-\infty}^{+\infty} PSD(f) e^{i2\pi f\, r} df \ . \qquad (2.37)$$

Despite this simple relation between ACF and PSD, the correct calculation of ACF from PSD can be significantly affected in practice by effective bandwidth limits with absence of PSD data at low spatial frequencies blocked by the sample holder as well as above the frequency $f_{max} = sin(90°/\lambda) = 1/\lambda$. In most cases, absence of experimental data introduces significant artifacts in ACF. Therefore, correct calculation of ACF requires reconstruction of PSD within regions where the experimental data are absent. One of the solutions is to apply the Gerchberg-Saxton error reduction (ER) algorithm, which produces a more neutral precise reconstruction of the ACF and PSD pair.

The n-th cycle of the ER algorithm can be written as

$$ACF_n^*(r) = FFT^{-1}\{PSD_n(f)\}$$

$$ACF_n(r) = \begin{cases} Re[ACF_n^*(r)] & if\ r \in S \\ 0 & if\ r \notin S \end{cases}$$

$$PSD_{n+1}^*(f) = FFT\{ACF_n(r)\} \qquad (2.38)$$

$$PSD_{n+1}(f) = \begin{cases} PSD_{obs}(f)\ if\ f \in f_{obs} \\ Re[PSD_{n+1}^*(f)]\ if\ f \notin f_{obs}, Re[PSD_{n+1}^*(f)] \geq 0 \\ 0 \quad otherwise \end{cases}$$

where PSD_{obs} is the measured PSD function within f_{obs} spatial frequencies, S is the ACF's support (i.e., area where ACF is nonzero), ACF^* is the inverse fast Fourier transform FFT^{-1} of the measured PSD with reconstructed part, and PSD^* is the direct fast Fourier transform FFT of the reconstructed ACF.

The constraints in the ER algorithm are quite strong, since both ACF and PSD functions are real; hence, the ACF phase is 0 or π. This provides reliable and relatively fast convergence to reproducible results. The progress of iterations are monitored with the real-space squared error

$$\varepsilon_n^2 = \frac{\sum_{r \notin S} |ACF_n^*(r)|^2}{\sum_{r \in S} |ACF_n^*(r)|^2} \qquad (2.39)$$

The size of the support S is chosen to be comparable with the size of probe beam so as to provide convergence with minimal ε_n^2. A detailed description of the ER algorithm and its application to phase reconstruction and imaging can be found in [50].

Chapter 3 Methodology

3.1 Thin Film Fabrication by PLD

Thin films were fabricated via pulsed laser deposition method. PLD is a growth technique commonly used for the fabrication of thin films since the late eighties. A typical PLD chamber is shown in figure 3.1. An intense laser beam pulse is passed through an optical window of a vacuum chamber and is focused into a target, either solid or liquid, where it is partially absorbed and reflected. Typically the ablation of the target is performed with a KrF excimer laser of wavelength $\lambda = 248\ nm$. Once the target is illuminated at a specific power density, a significant removal of the material occurs in the form of an ejected luminous plume. This ejection of such plume depends on the material being used, its morphology and the laser pulse and duration. Material ejected from the plume is deposited on a substrate, where film growth occurs. This film growth is usually accompanied by a passive or reactive gas or ion source which may affect the ablation plume species in the gas phase or the surface reaction. [51]

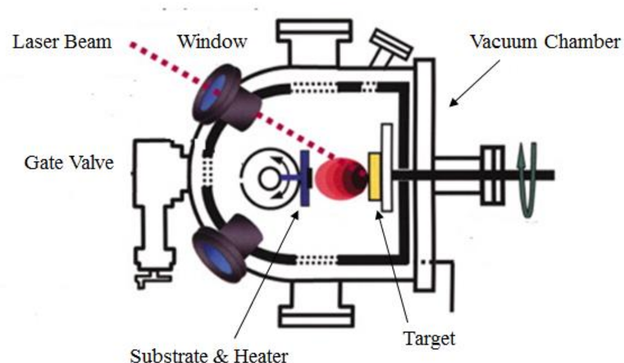

Figure 3.1 Schematic of a PLD system. Taken from [52]

The VO_2 thin films were grown by PLD technique on amorphous SiO_2 and on single crystal Al_2O_3 (A-cut, M-cut and R-cut) sapphire substrates. Such ablation of the metallic vanadium target was performed by excimer laser (Lambda Physik Compex 110, KrF excimer laser) with a wavelength of $\lambda = 248\,nm$, fluence of 4 J/cm^2 and a frequency of $10\,Hz$. For the sapphire deposited films a chamber atmosphere of O_2 and Ar at $30\,mTorr$ was used, and substrate was kept at a constant temperature of $550^{\circ}C$.

3.2 Crystal Structure

To determine the structure of the VO_2 thin films angle resolve x-ray diffraction (XRD) technique was used. The x-ray diffraction measurements were performed using a Bruker D8 Discover diffractometer (Bruker AXS, Karlsruhe, Germany). It is a 4 cycle diffractometer specially configured for thin film studies. The x-ray beam lines include a parabolic multilayer x-ray mirror for increased intensity and collimation. All motions are through computer controlled by stepper motors. Also available is an attachment for grazing-incidence reflectometry measurements [53].

3.3 Reflection Measurements

Angle-resolved reflection measurement technique was used to obtain information about the sample thickness and linear absorption coefficient. A continuous wave semiconductor laser with wavelength of $\lambda = 532\,nm$ was used for the measurements as shown in figure 3.2. Laser beam passes through various mirrors and a polarizer to control the desired polarization. The polarized light hits the sample at normal incidence which is mounted on a custom built motorized goniometer capable of angular measurements with a precision of about 0.001°. Reflected light is collected by a CCD camera whose angular position is controlled via computer.

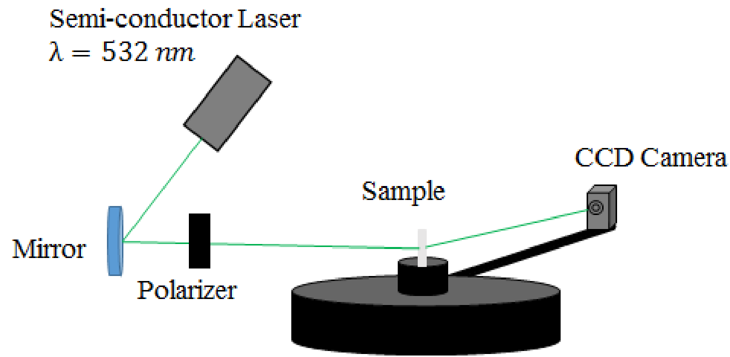

Figure 3.2 Schematic view for reflection measurements for thin films.

3.4 Z-Scan Setup

Measurements of optical nonlinearities were conducted using Z-scan technique. A "Continuum PY61C-10" Nd:YAG laser system with 30 ps pulse duration, 10 Hz repetition rate and a wavelength of $\lambda = 532\ nm$ was used for both open and closed aperture measurements. The beam waist radius was focused to $\omega_0 = 8.70\ \mu m$ with a spatial profile of a Gaussian pulse. A schematic view of the Z-scan setup is shown in figure 3.3. The thin film samples were moved by a home built translational stage where the step, velocity scan length are controlled by a costume program. Set of calibrated filters was used in order to vary the incident light intensity. From there it passes through a pin hole to have a beam with a Gaussian profile, and then it is passed through a lens in order to collimate the beam. In order to align the system more easily a series of iris are used to make sure that the beam is properly aligned and is parallel to the stage. Before hitting the sample the laser beam goes through another lens in order to focus it directly to the sample. The transmitted light is divided by a beam splitter and collected by two detectors with open and closed aperture to measure the desired non-linear absorption and refraction of the samples. These detectors are connected to a gated integrator and boxcar averager module (SRS Model SR250),

and a 500 MHz digital oscilloscope (Tektronics TDS 620B) to record the output signal. Power of the laser to the thin films was controlled by a set of calibrated filters and the energy of the beam was measured using a two channel Joulemeter (Molectron JD 2000). Closed aperture scans were done with an iris where size of the aperture can be controlled ranging from 2 mm to 5 mm to minimize non-linear absorption. Data collected by the detectors are recorded into text files that are later processed and fitted in Origin 9™ software. Fitted quantities obtained from both open and aperture scans are then used to obtain the nonlinear index of refraction, nonlinear absorption coefficient and the third order electrical susceptibility using a written algorithm in MATLAB™.

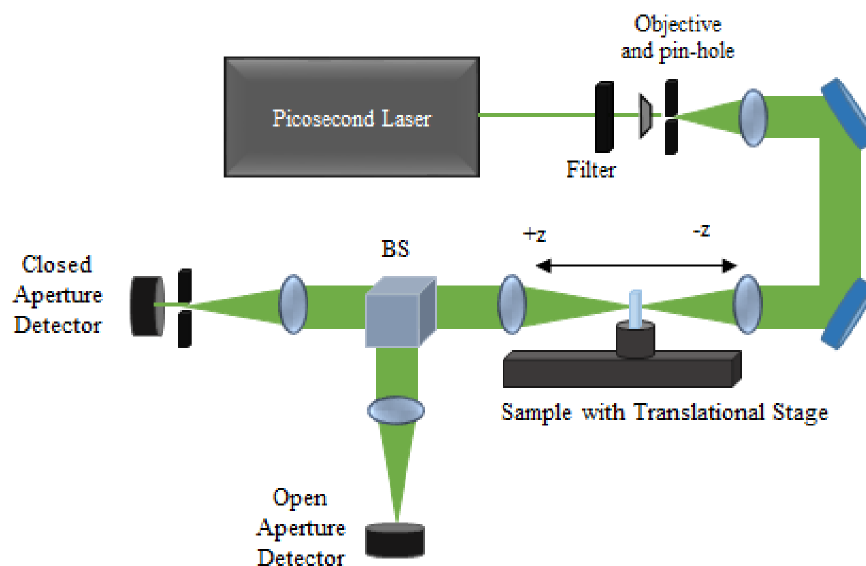

Figure 3.3 Schematic drawing of Z-Scan setup built in the laboratory.

3.5 Laser System

The PY61C-10 laser system by Continuum is a picosecond laser that is a cavity dumped active/passive mode-locked system. It uses an oscillator to give high energy single pulses and provide a nearly Gaussian beam profile. The oscillator cavity employs mode-locking and cavity dumping technique to extract a single pulse from the pulse train. This allows increasing the single pulse energy in picosecond solid state and dye lasers. The cavity dump laser consists of the electro-optic Pockels cell and is triggered by a photodiode. The photodiode sense the intensity buildup inside the cavity. The selected output single pulse is ejected via a polarizer when a certain intensity level is reached.

The laser consists of two main parts: the optical bench and the power supply. When powered by the power supply the optical bench contains all the necessary components for generating an infrared laser beam or its 2nd, 3rd or 4th harmonics. The optical bench has three main parts: an oscillator, amplifier and optional harmonic generators and wavelength separations optics. The oscillator consists of a high quality hard coated concave mirror in the dye cell which contains the passive mode locking dye. An active mode-locker is composed of a modulator crystal and a delay prism arrangement to change the optical path length without affecting the optical alignment. Figure 3.4 shows the PY61C-10 layouts [54].

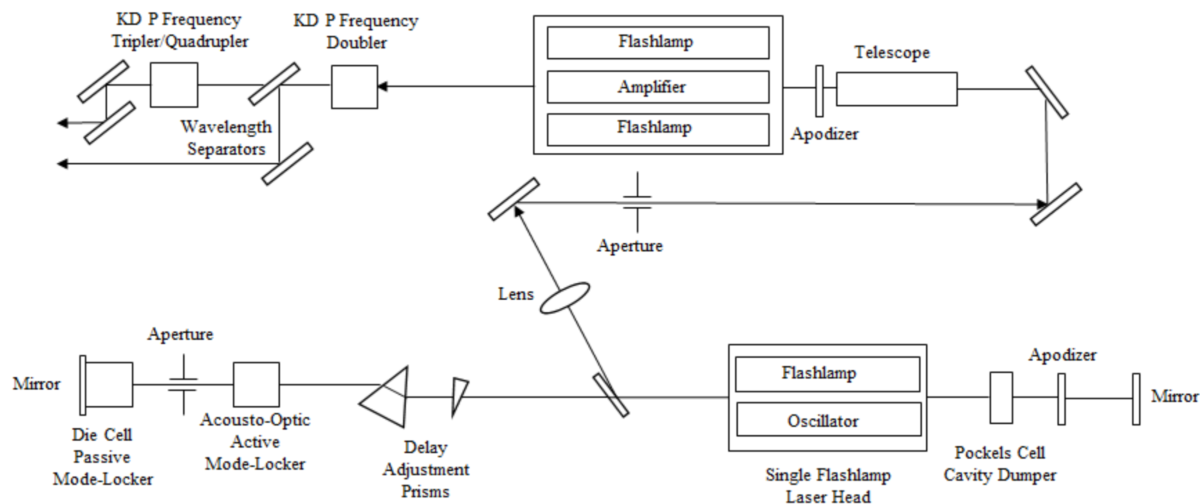

Figure 3.4 PY61C-10 Laser schematic and layout.

3.6 Scattering

In order to study the light induced PT dynamics of vanadium oxides a scatterometer equipped with a Spectra-Physics laser system was used as shown in figure 3.5. The laser system consists of a Ti:sapphire oscillator and a regenerative amplifier operating at wavelength λ =800 nm. Laser pulses are compressed down to 130 fs and split by a beam splitter into pump and probe beams. The probe pulses were frequency doubled by a 100 μm thick BBO crystal to the wavelength $\lambda =$ 400 nm, while the wavelength of pump radiation was λ =800 nm. The shorter probe wavelength allowed monitoring multiscale surface structures with spatial frequencies up to $f = 1/\lambda$ =2.5 μm^{-1}. Incident light was linearly polarized by a Glan-type prisms GP and GP'. The polarization of pump pulse was controlled by a half-wave plate $\lambda/2$ and GP, so the mutual orientation of electric field vectors of pump and probe can be set parallel or orthogonal. To initiate the PT of VO_2 film, the pump pulse was focused to a spot size of 1.2 mm. The spot size of the

probe pulse was less than 100 μm in order to ensure interrogation of only a uniformly excited region of the sample. Intensity of the probe beam was substantially reduced by a neutral density filter to eliminate any nonlinear interaction of the beam with the sample. Scattered light within the hemisphere was projected to a CCD by elliptical mirror. The temporal delay t between the pump and probe pulses was controlled by a motorized translational stage equipped with a retroreflector [43].

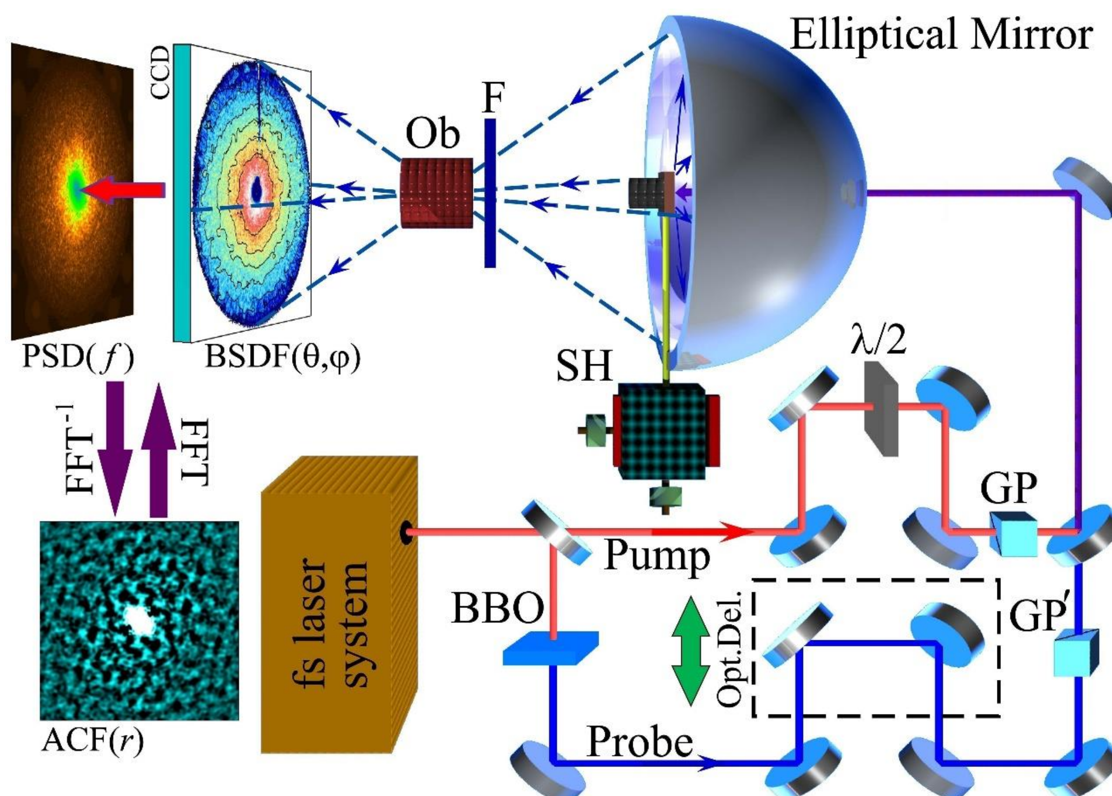

Figure 3.5 Experimental setup for hemispherical angle-resolved light scattering measurements [43].

Chapter 4 Results and Discussion

4.1 Beam waist radius measurements

It is necessary to know the beam waist radius of the beam in order to extract information from Z-scan data. In order for this technique to work, one must have beam with a pure Gaussian spatial profile. Not achieving this will result in Z-scan technique not working at all. In order to extract the beam waist radius parameter ω_0 a Mightex USB camera was used to take several images of the beam close to the focus. The image data file was then analyzed in MATLAB™ using a Gaussian fit. Figure 4.1 shows the graph resulting from the analysis of the picture file from the program.

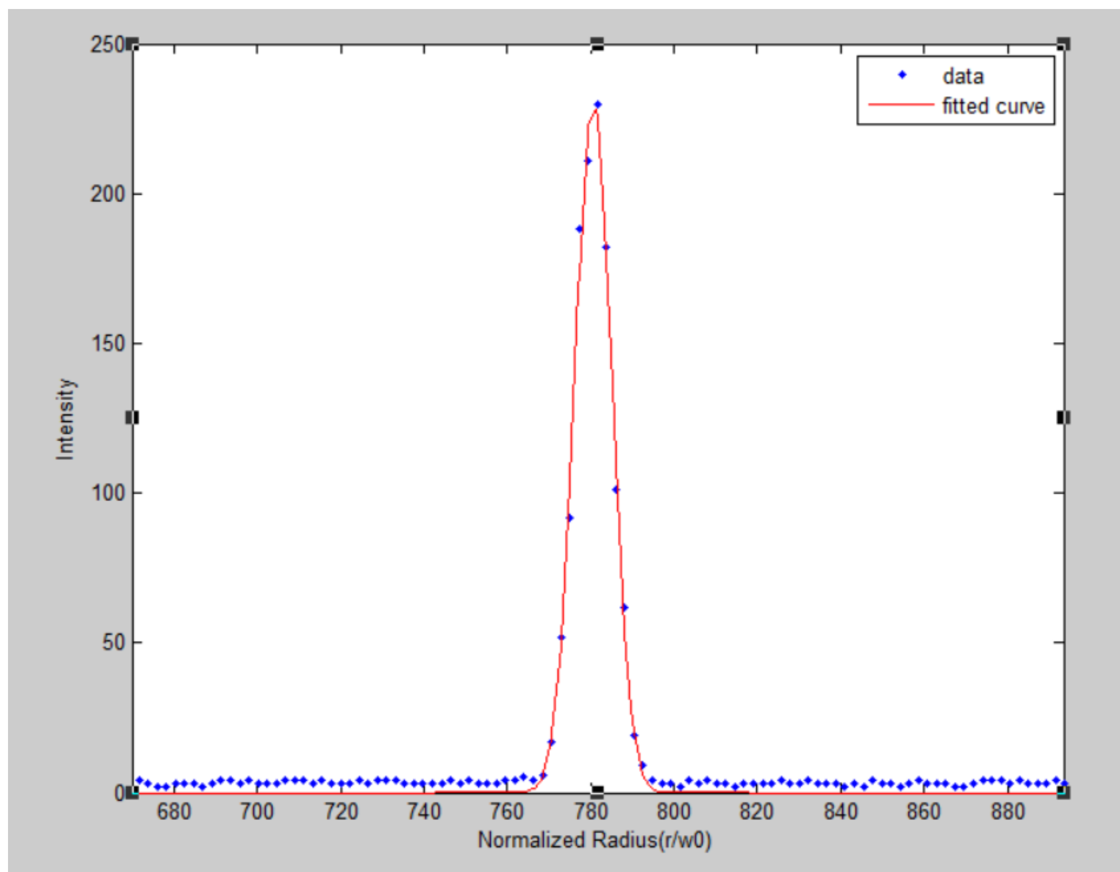

Figure 4.1 The profile at focal plane and Gaussian fit for laser beam with wavelength $\lambda = 532\ nm$.

After fitting the graph, a value of $\omega_0 = 8.70\ \mu m$ was obtained for the beam waist radius. Using this value one can calculate the Rayleigh range given by $z_0 = \frac{\pi\omega_0^2}{\lambda}$, the calculated value for the Rayleigh range was $z_0 = 0.45\ mm$.

4.2 X-Ray Diffraction

In order to analyze the structural properties of the samples used, X-ray diffraction was performed. Figure 4.2 shows the XRD pattern for two samples of VO_2 deposited over amorphous SiO_2.

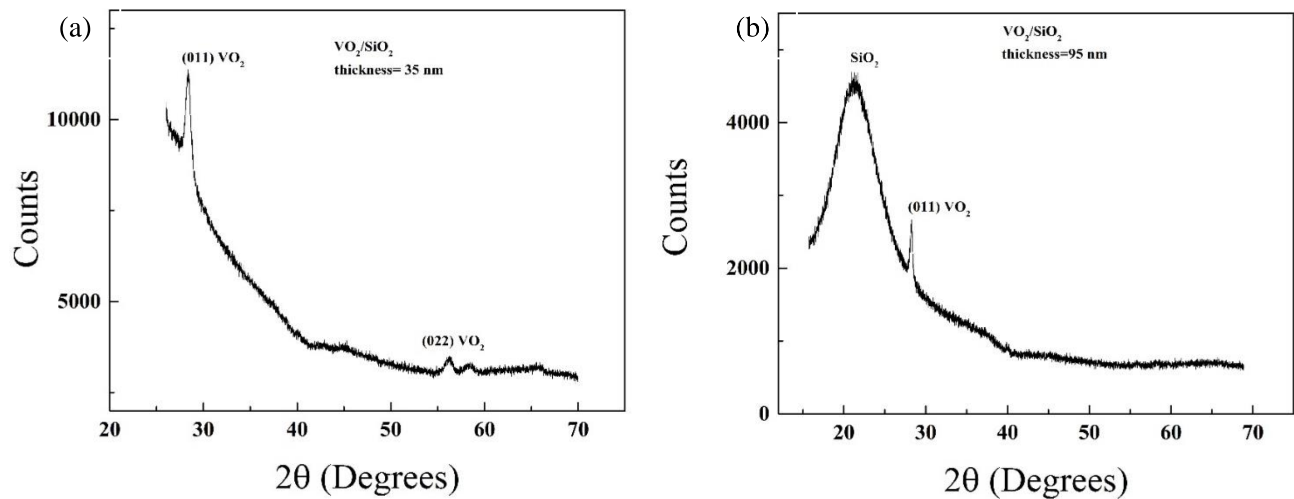

Figure 4.2 X-ray diffraction patterns of VO_2 films of different thickness deposited on amorphous SiO_2 substrates. (a) is for the 35 nm thick film and (b) is for the 95 nm thick film.

From the XRD pattern one can see the typical M_1 phase reflection peak located at $2\theta = 28.33^\circ$ for figure (a) and $2\theta = 28.22^\circ$ for figure (b). These peaks are attributed to reflections from the (011) plane for both films of VO_2/SiO_2. For figure (a) another peak is seen at approximately $2\theta = 56.28^\circ$ belonging to reflections from the (022) plane. On figure (b) a broad peak with a maximum

at exactly $2\theta = 21.29^{\circ}$ can be observed, this corresponds to SiO_2 substrate. The peak is also observed on figure (a) but is not shown since it was cut to only show the VO_2 contribution to the signal.

To further study the orientation of the VO_2 films deposited on sapphire substrates (Al_2O_3) in the surface plane, azimuthal scans were performed. Shown in figure 4.3 are XRD azimuthal scans for both the Al_2O_3 A-cut substrate and VO_2 film.

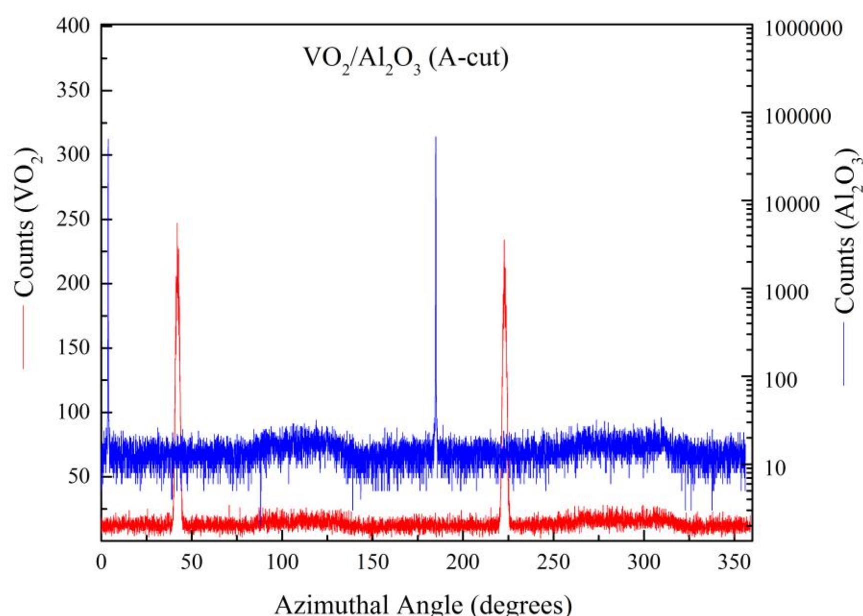

Figure 4.3 X-ray diffraction counts vs azimuthal orientation for VO_2/Al_2O_3 (A-cut) thin film.

To study the surface plane orientation of the substrate, reflections from the R plane (012) with an angle of $\chi = 43.01^{\circ}$ with the A plane (110) was used. Strong peaks can be observed at angles of 3.8° and 185° for the substrate. For the film the planes (011) and (010) was used with and angle of $\chi = 44.95^{\circ}$ in between them. From the graph strong peaks can be seen at 42.2° and 223°.

4.3 Angular Dependence of Reflection Measurements

Quantitative analysis of reflection measurements gives information about the material optical constants and structure. Figures 4.4 shows the results for reflectance as a function of angle of incidence for λ=532 nm and samples of 35 nm, 75 nm and 95 nm thick amorphous VO_2/SiO_2 thin films. Reflection measurements are taken for two orthogonal polarizations, perpendicular (R_s) and parallel (R_p) to the incident plane. Values for the Brewster angle for the thin films is located between 65° and 68°.

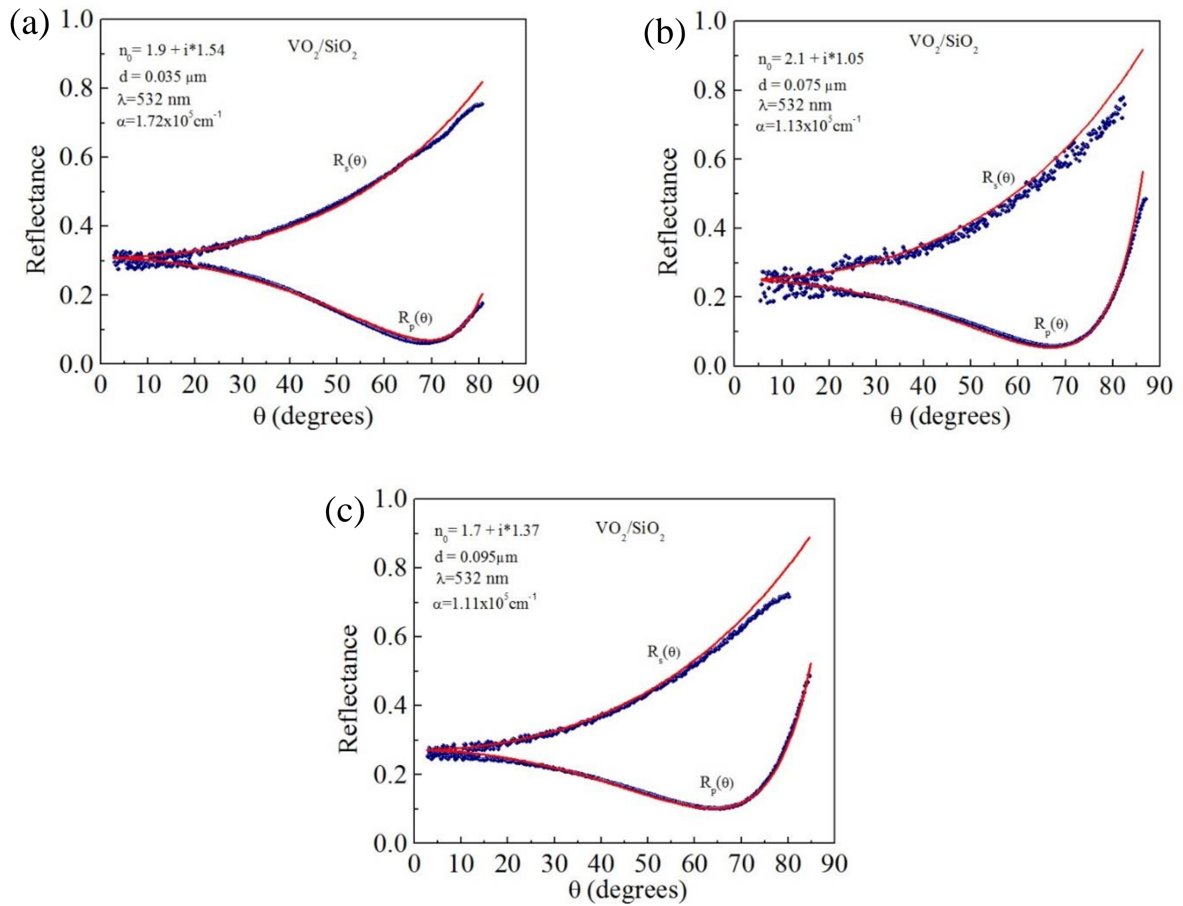

Figure 4.4 Angular dependence of the reflectance for two polarizations for VO_2/SiO_2 at λ=532. (a) is for 35 nm thick film, (b) is for 75 nm thick film and (c) is 95 nm thick film. Symbols are experimental data and lines are calculated reflectance from fit.

Using Fresnel's relations from [55] for thin films, data was fitted in good agreements to the theoretical curves for both orthogonal polarizations. From the fitted curves the real part and imaginary part of the index of refraction for the thin films was found to be $n = 1.9 + i1.54$ for the 35 nm thick film, $n = 2.1 + i1.05$ for the 75 nm thick film and $n = 1.7 + i1.37$ for the 95 nm thick film. Besides knowing the thickness and index of refraction of the material, the absorption coefficient α is of great importance to characterize the material. For the thin films deposited over glass the absorption coefficient is obtained from the following relation:

$$I = I_0 e^{-\alpha d} \qquad (4.1.1)$$

where I is the light intensity after passing through the sample, I_0 is the incident intensity of the beam before passing through the sample and d is the sample's thickness. Table 4.1 summarizes the optical constants for all thin films of VO_2/SiO_2 for λ=532 nm.

Film Thickness	Index of Refraction	Absorption coefficient
35 nm	$1.9 + i1.54$	$1.72x10^5\ cm^{-1}$
75 nm	$2.1 + i1.05$	$1.11x10^5\ cm^{-1}$
95 nm	$1.7 + i1.37$	$1.13x10^5\ cm^{-1}$

Table 4.1 Optical constants for VO_2/SiO_2 thin films of different thickness for a wavelength of λ=532 nm.

These optical constants are necessary to extract the third order nonlinear optical constants of the material.

4.4 Z-Scan Results for VO_2/SiO_2 Thin Films

The following Z-scan results are from a variety of samples of VO_2 films deposited over amorphous glass (SiO_2) and the highly oriented sapphire substrate (Al_2O_3) of different cuts (A-cut, M-cut and R-cut). Thin films of VO_2/SiO_2 were kept at room temperature (Insulating phase) for their Z-scan measurements, while VO_2/Al_2O_3 films measurements were both taken at room temperature and above their phase transition temperature ($T_C \approx 340\ K$).

Closed aperture scans are shown in figure 4.5 for VO_2/SiO_2 thin films at different laser input power or fluence. For all three samples the signature peak to valley profile can be seen, this is an indicator of a self-defocusing effect occurring inside of the sample and of a negative non-linear index of refraction.

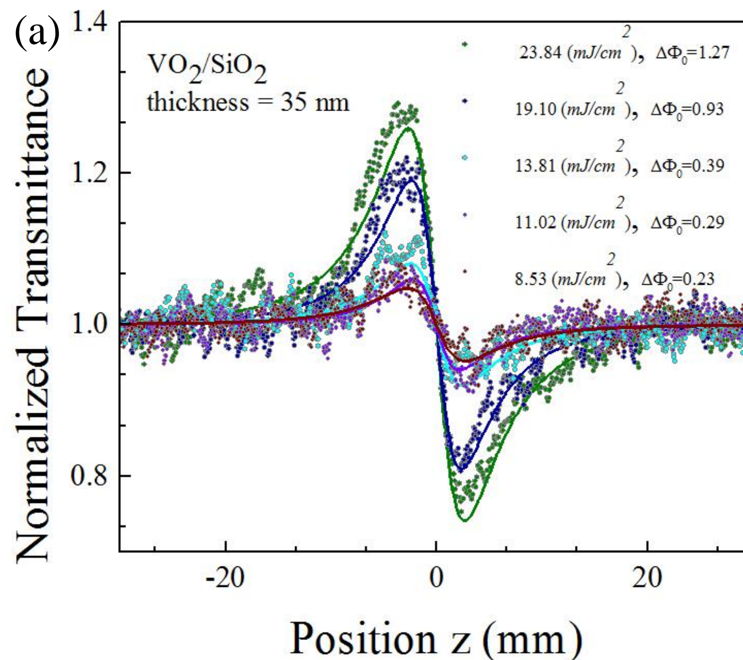

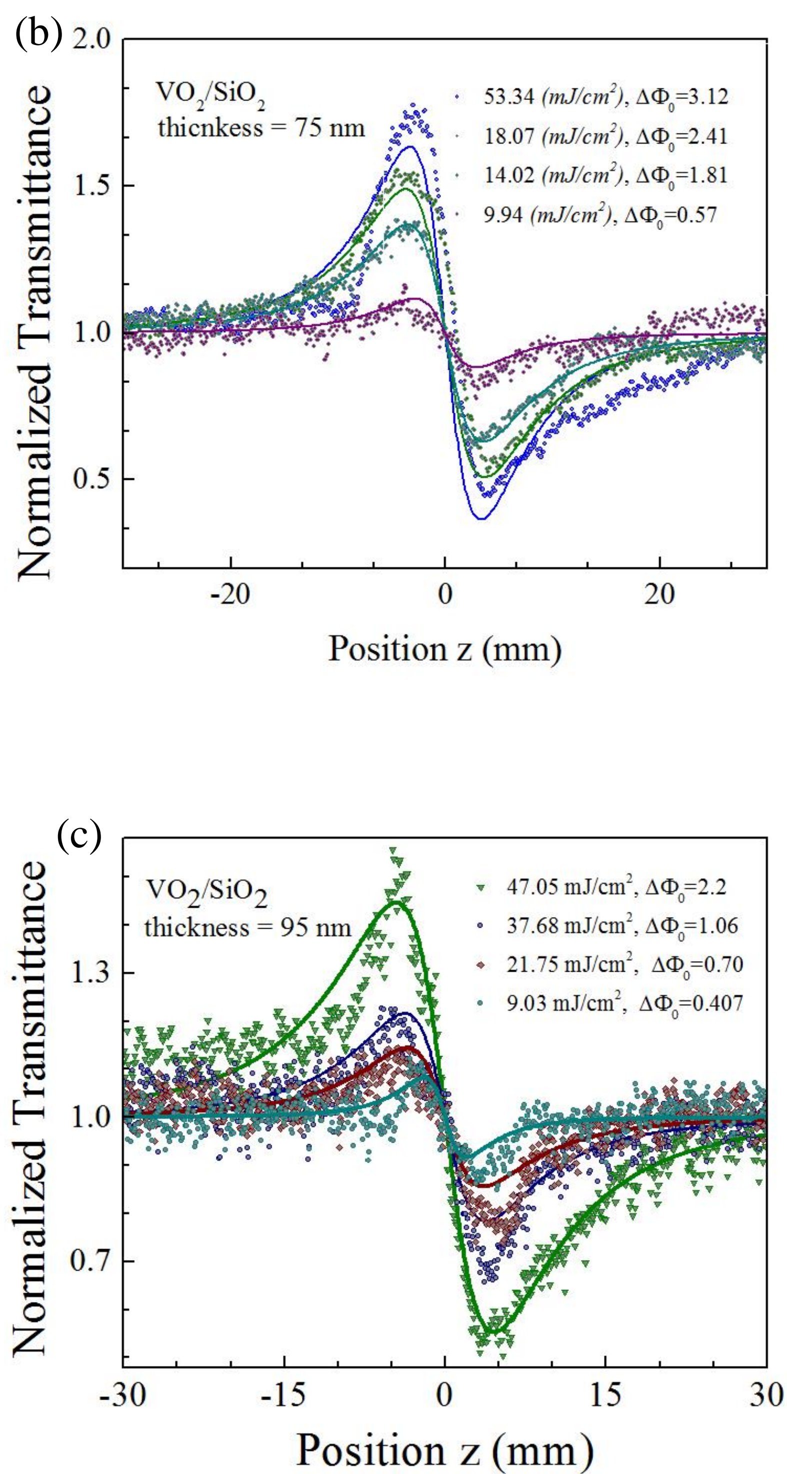

Figure 4.5 Closed aperture Z-scans for VO_2/SiO_2 thin films at different laser fluences. (a) is for a 35 nm thick film at room temperature, (b) is for a 75 nm thick film at room temperature and (c) is for a 95 nm thick film.

For all three samples it was noted that nonlinearity increased with incident laser fluence, and above a certain laser fluence the sample could be damaged. Here the nonlinearity is purely from the VO_2 material and not the substrate. It was found that the thicker samples tended to be more easily damaged because of absorption in comparison to the thinner samples. All curves were fitted using the method from the references [6] [56], [57] and [58], yielding the phase shift parameter $\Delta\Phi_0$.

Similarly figure 4.6 shows open aperture Z-scan for the same samples at different laser fluence. A typical symmetric valley at the focus ($z = 0\ mm$) is observed for certain fluences in all the samples.

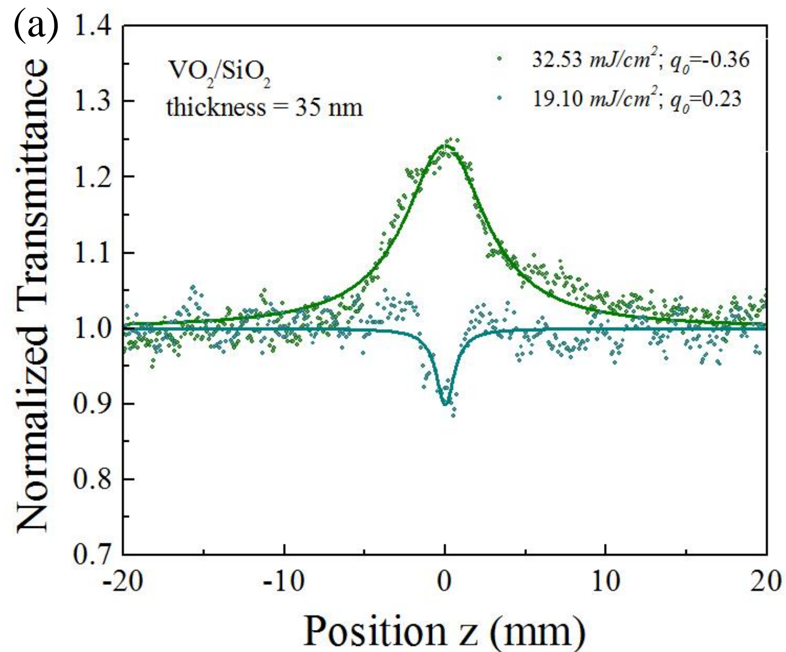

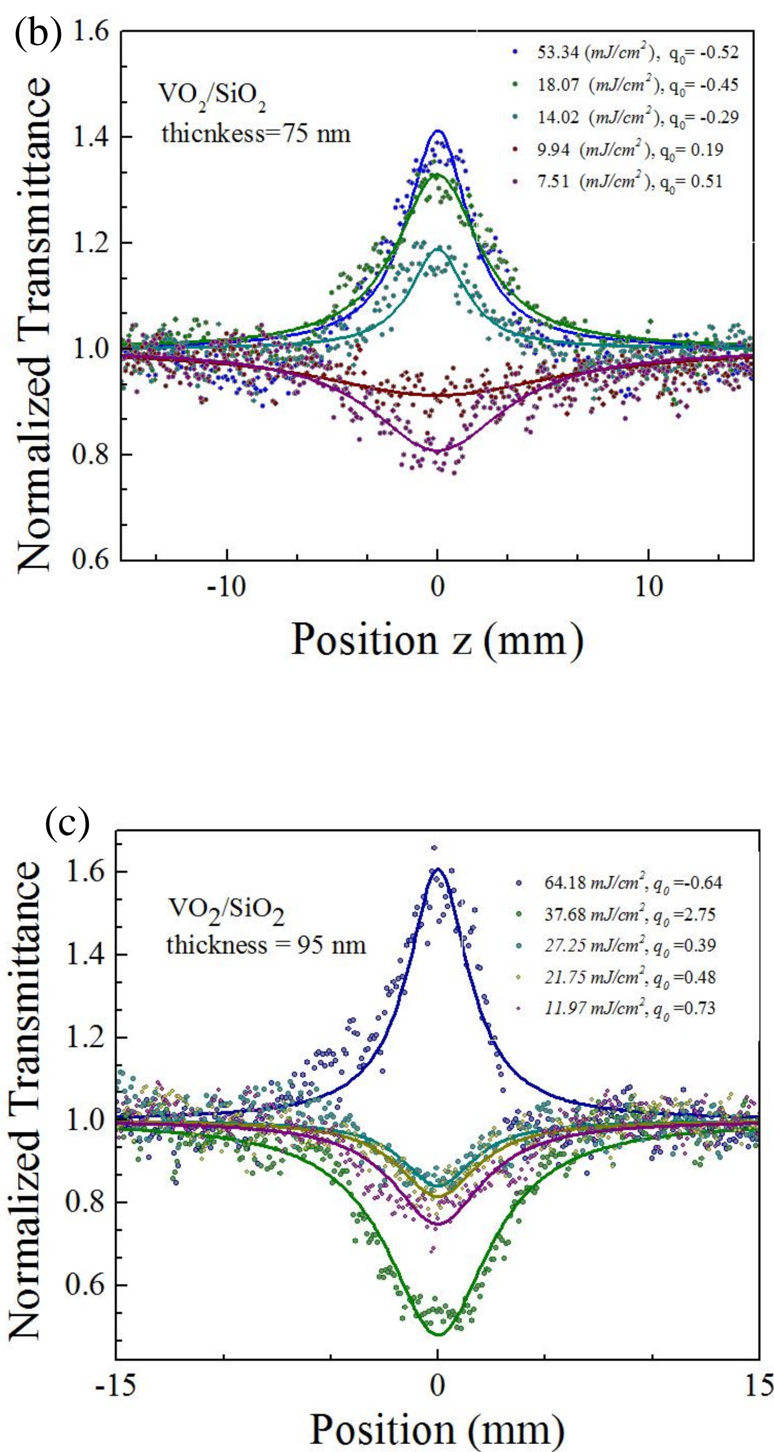

Figure 4.6 Open aperture Z-scans for VO_2/SiO_2 thin films at different laser fluences. (a) is for a 35 nm thick film at room temperature, (b) is for a 75 nm thick film at room temperature and (c) is for a 95 nm thick film.

For all three samples an inversion of the valley at the focal point is seen for a certain threshold value of fluence. For the thicker sample $(95\ nm)$ the threshold value found for the inversion of the peak was 64 mJ/cm^2, for the 75 nm the inversion of the peak was seen at 14 mJ/cm^2 and for the thinner sample it was observed at 33 mJ/cm^2. The difference in fluence value for the threshold is related to the sample's thickness, thicker samples tend to absorb more light. The inversion of peak can be attributed to several effects, including the interference effect inside the thin film at higher intensities. At higher intensities the increased transmittance could be attributed to the phase transition of the material along with saturable absorption, at higher intensities the light-induced phase transition occurs and thus the sample becomes metal. Fitting of these graphs yields the parameter q_0 which is used to extract the nonlinear absorption coefficient β.

Since nonlinearity increases with increasing fluence, then the phase shift parameter $\Delta\Phi_0$ must also increase with respect to the fluence. Figure 4.7 shows $\Delta\Phi_0$ as a function of laser fluence for all three samples. The graphs also show the quantity ΔT_{p-v} which is the difference between the transmission peak and transmission valley as a function of intensity from equation 2.26. For figures (a) and (c) both $\Delta\Phi_0$ and ΔT_{p-v} remain constant until a fluence value of 14 mJ/cm^2 for (a) and 22 mJ/cm^2 for (c). This behavior can be attributed to third order nonlinearity below the threshold fluence value. As fluence increases other effects arise and nonlinearity now is not only of the third order but a combination of first and third order effects. Another explanation could be due to the picosecond pulse of the laser and its electrostriction effect. Such effect would cause a change in the sample due to the high electric field of the pulse, causing the material to either become compressed or stretched due the high field.

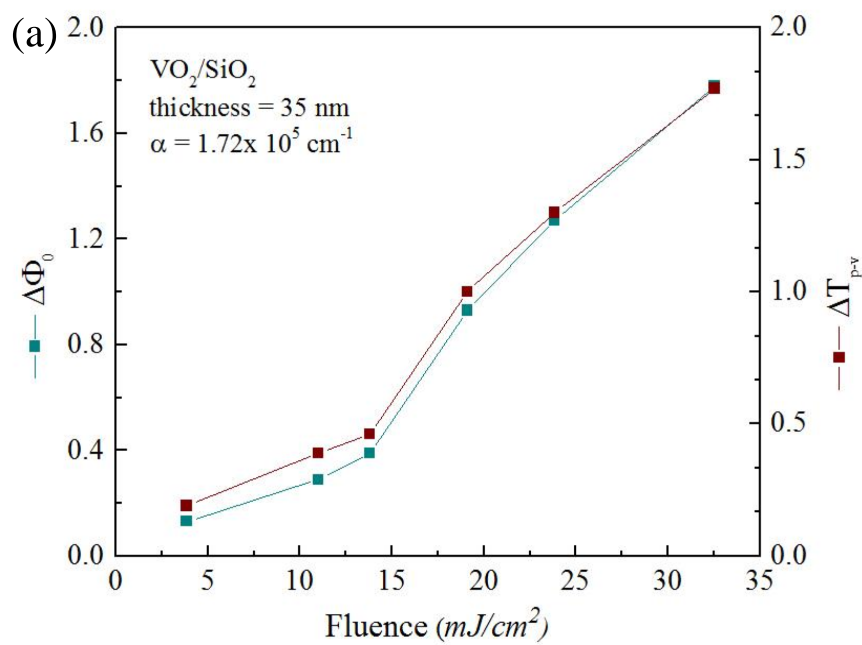
(a)
VO2/SiO2
thickness = 35 nm
α = 1.72x 10^5 cm^-1
ΔΦ0
ΔTp-v
Fluence (mJ/cm^2)
0.0
0.4
0.8
1.2
1.6
2.0
0.0
0.5
1.0
1.5
2.0
0
5
10
15
20
25
30
35

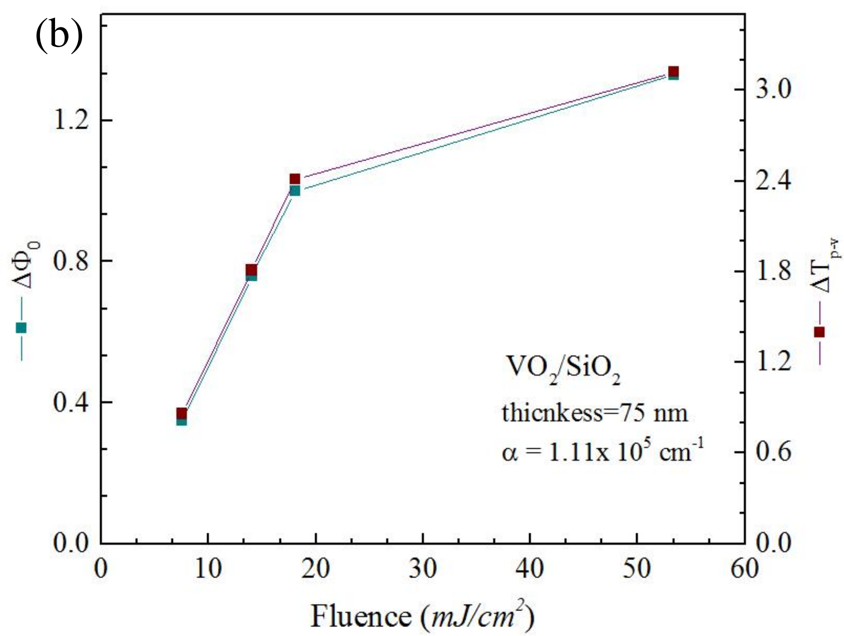
(b)
VO2/SiO2
thicnkess=75 nm
α = 1.11x 10^5 cm^-1
ΔΦ0
ΔTp-v
Fluence (mJ/cm^2)
0.0
0.4
0.8
1.2
0.0
0.6
1.2
1.8
2.4
3.0
0
10
20
30
40
50
60

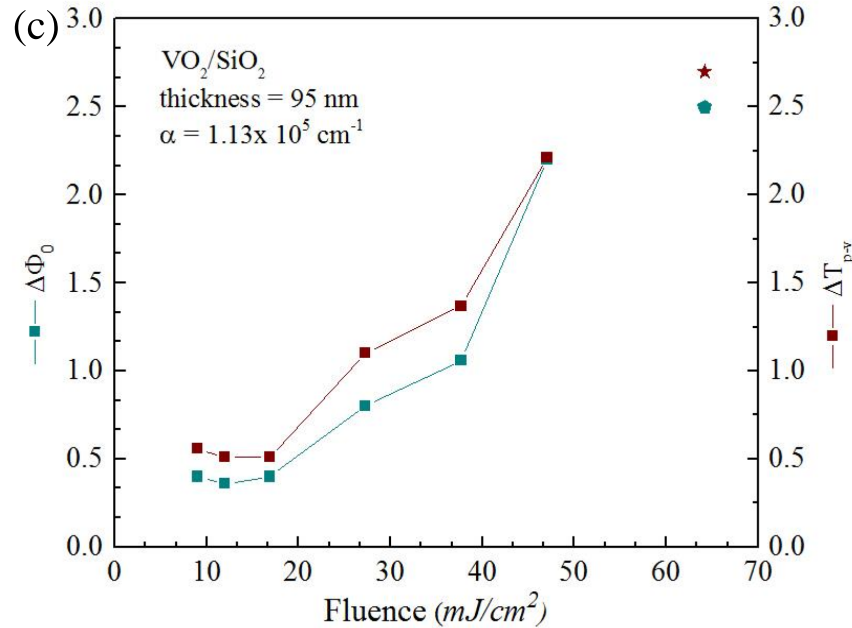

Figure 4.7 Graphs of both $\Delta\Phi_0$ and ΔT_{p-v} as a function of fluence for VO_2/SiO_2 thin films. (a) is for the 35 nm thin film, (b) is for the 75 nm thin film and (c) is for the 95 nm thin film.

As for figure (b) an almost linear behavior can be seen for this thin film, nonlinearity for this sample can be attributed to third order since the laser fluence was below 20 mJ/cm^2. The sudden increase for the values could be because of interference effects in the sample, the high electrostrictive force due to the pulse, or that the sample was damaged due to the high fluence. As seen on figure 4.6 graph (b) at this value of fluence the closed aperture scan shows the highest transmittance peak-valley for all measurements for this sample and the effects mentioned before are more prominent.

Furthermore for each fitting of open and closed aperture the quantity z_0 was a fitting parameter. Figure 4.8 shows the Raleigh range z_0 as a function of fluence for both open and closed aperture.

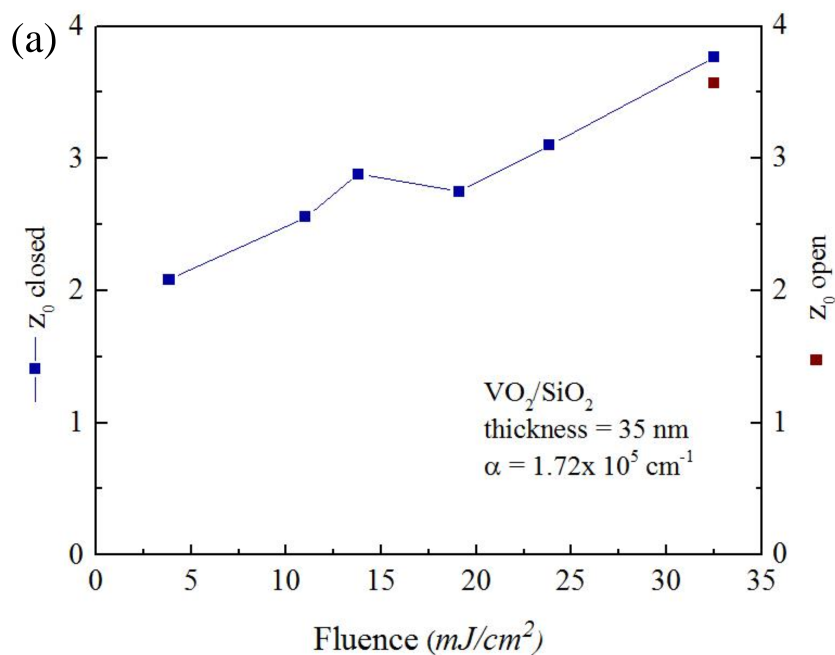

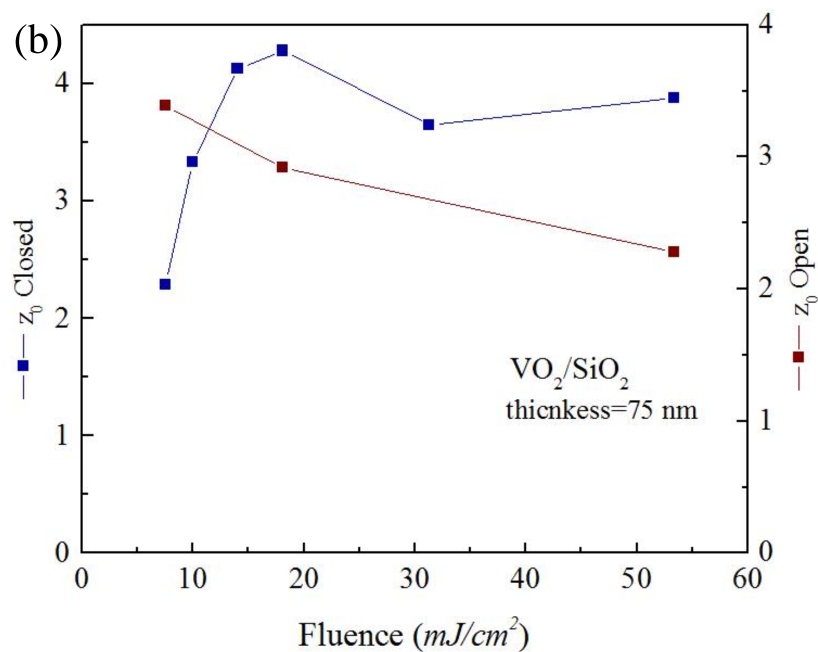

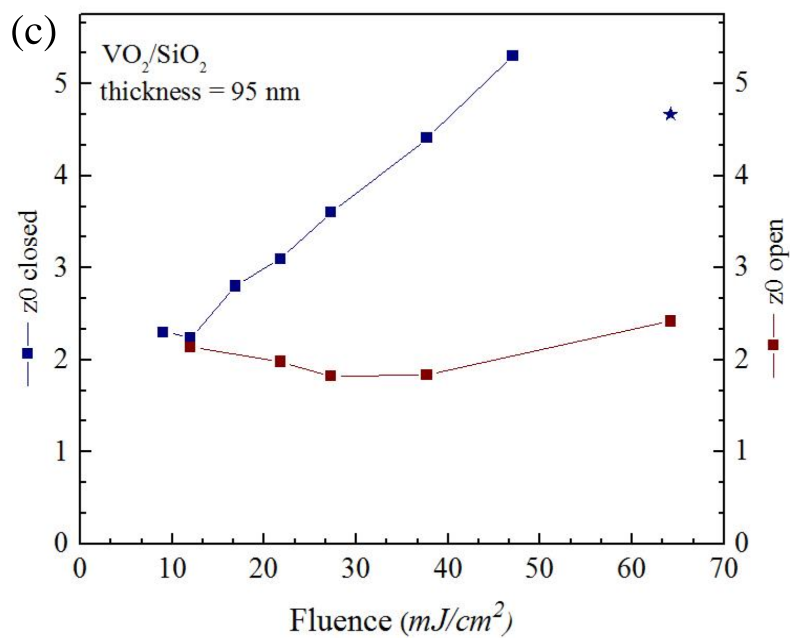

Figure 4.8 Graphs of Rayleigh range parameter z_0 for open and closed aperture as a function of fluence for VO_2/SiO_2 thin films. (a) is for the 35 nm thin film, (b) is for the 75 nm thin film and (c) is for the 95 nm thin film.

For closed aperture from figures (a) and (c) a clear increasing behavior can be seen as fluence increases. The 95 nm thick sample shows a point at a fluence value above $60\ mJ/cm^2$ where the z_0 value decreases with respect to the others. This may be caused by damage inside the sample due to the high fluence. Since it has the biggest thickness from all the samples used, it is prone to absorb more and thus be more easily damaged. A similar behavior can be observed for the 75 nm thick sample, but the fluence threshold was found to be less. An explanation for the increasing behavior could be that with increasing fluence the sample may be in an intermediate state where it is both insulating and metallic, or it could be entirely in its metallic state. The same can be said for the 35 nm thick sample, but no damage was observed for this sample. For open aperture, the z_0 value remained constant for the thicker samples. In the closed aperture measurements the detector is more sensitive to any focusing or defocusing effect caused by the sample. With open aperture scan, the detector receives all light as the sample is moved therefore it is not as sensitive as the closed aperture technique.

Optical constants were obtained for all three samples. Figures 4.9 and 4.10 show various optical constants and third order susceptibility plotted as a function of fluence for the 35 nm and 95 nm thick samples. $\Delta\Phi_0$ and q_0 are the first parameters obtained from fitting. These quantities are then used to obtain both the nonlinear index of refraction γ in $(\frac{m^2}{W})$ and the converted to $n_2(esu)$ by the relation $n_2(esu) = \frac{cn_0\gamma}{40\pi}$ and in turn this is converted to $n_2eff(esu)$ by the relation $n_2eff(esu) = \sqrt{2}\, n_2(esu)$. Similarly, the nonlinear absorption coefficient is obtained from q_0.

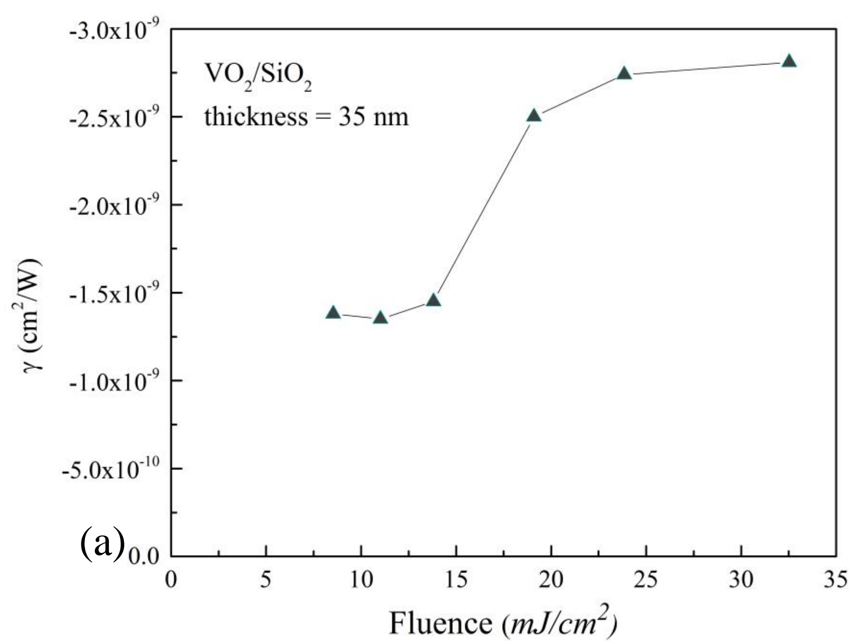

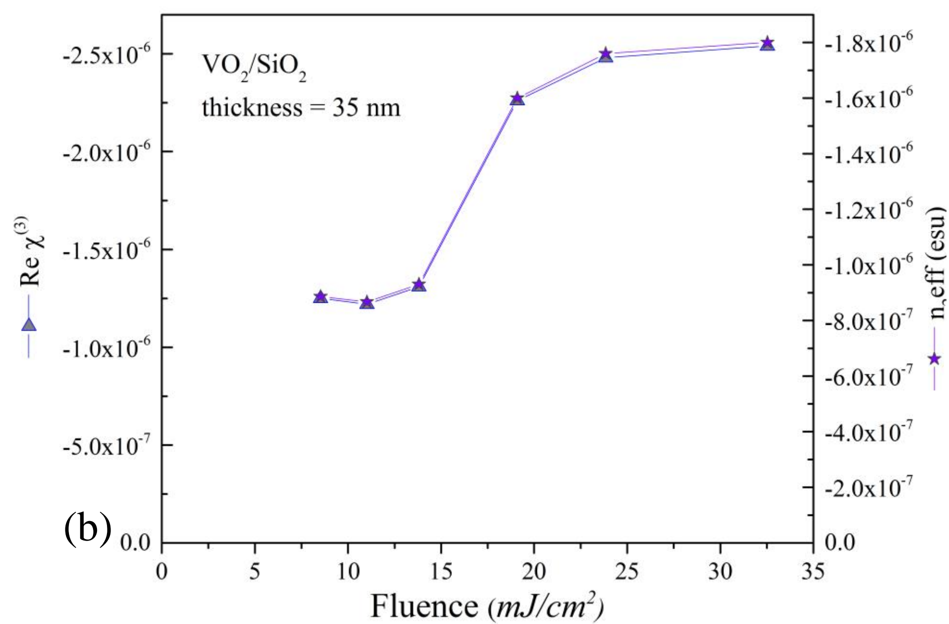

Figure 4.9 (a) Graph of nonlinear index of refraction $\gamma\ (m^2/W)$ for the 35 nm thick sample. (b) Graph of $n_2eff(esu)$ and real part of the third order susceptibility $Re\chi^{(3)}(esu)$ as a function of fluence for the 35 nm thick sample.

For figures 4.9 (a) and (b) a similar behavior is observed for all values of fluences. The nonlinear index of refraction γ and n_2eff and the real part of the third order electrical susceptibility start out as constant until a fluence value of $14\ mJ/cm^2$. Below this threshold fluence and average value for both nonlinear indexes of refraction was found to be $\gamma = -1.39x10^{-9}\ cm^2/W$ and $n_2eff = -8.94x10^{-7}esu$. For the real part of $\chi^{(3)}$ the average value below this fluence was found to be $Re\chi^{(3)} = 1.26x10^{-6}\ esu$. There is a clear trend for these three curves at low fluences, at higher fluences all constants were found to increase and average values were found to be $\gamma = -2.68x10^{-9}\ cm^2/W$, $n_2eff = -1.72x10^{-6}esu$ and $Re\chi^{(3)} = 2.42x10^{-6}\ esu$ with the nonlinear index of refraction increasing about ten times. One possible explanation for the sudden change on the optical constants is that at higher fluences the material undergoes insulator-to-metal phase transition, while at lower fluences the optical nonlinearity is due to mainly electrostriction effect and or switching of VO_2 into an intermediate excited state. Above this threshold fluence the obtained value for the nonlinear absorption coefficient is $\beta = 7.4x10^4\ cm/GW$. Using this value and the value obtained for γ, the third order nonlinear susceptibility was found as $\left|\chi^{(3)}\right| = 2.57x10^{-6}\ esu$. This value in 10^2 and 10^4 times higher as compared to $\left|\chi^{(3)}\right|$ previously obtained by Liu *et al.* [14] and Lysenko *et al.* [26]. Possible explanations for this can be attributed to the observation of strong electrostriction effect in the present work using relatively long 30 ps pulses at 532 nm wavelength, and also possible excitation of intermediate transient state of VO_2. The high electric field would cause the molecules of the material to orientate along the given field within less than 30 ps, thus creating a stress on the material and changing its optical constants. In comparison, a femtosecond pulse or low intensity ps pulse, would not cause this kind of effect, as it only moves the electrons with its associated electric field and not the atoms. From figure 4.9 (b) as mentioned before, $Re\chi^{(3)}$ remains constant until the fluence level is $14\ mJ/cm^2$, when it

increases to $2.3x10^{-6}$ esu. Since the $Re\chi^{(3)}$ and $|\chi^{(3)}|$ should not be dependent on the intensity, the sudden increase for the values must be an indication that the sample as undergo a PT or is in some kind of intermediate state. Below the fluence threshold, the nonlinearity is purely from third order $\chi^{(3)}$ and above the threshold the nonlinearity is now a contribution of first order $\chi^{(1)}$ and third order $\chi^{(3)}$.

Similarly for the 95 nm thick sample figure 4.10 shows the graphs for the calculated optical constants as a function of fluence.

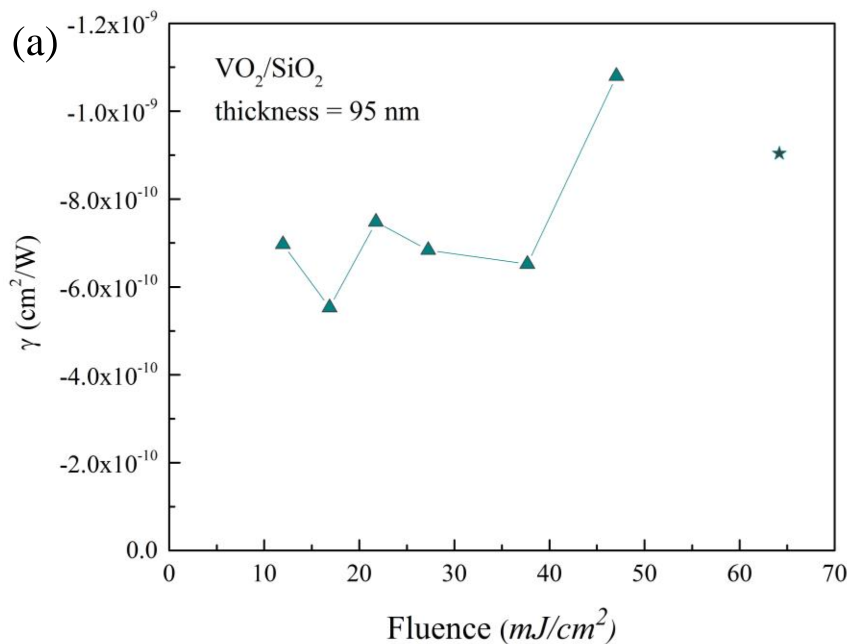

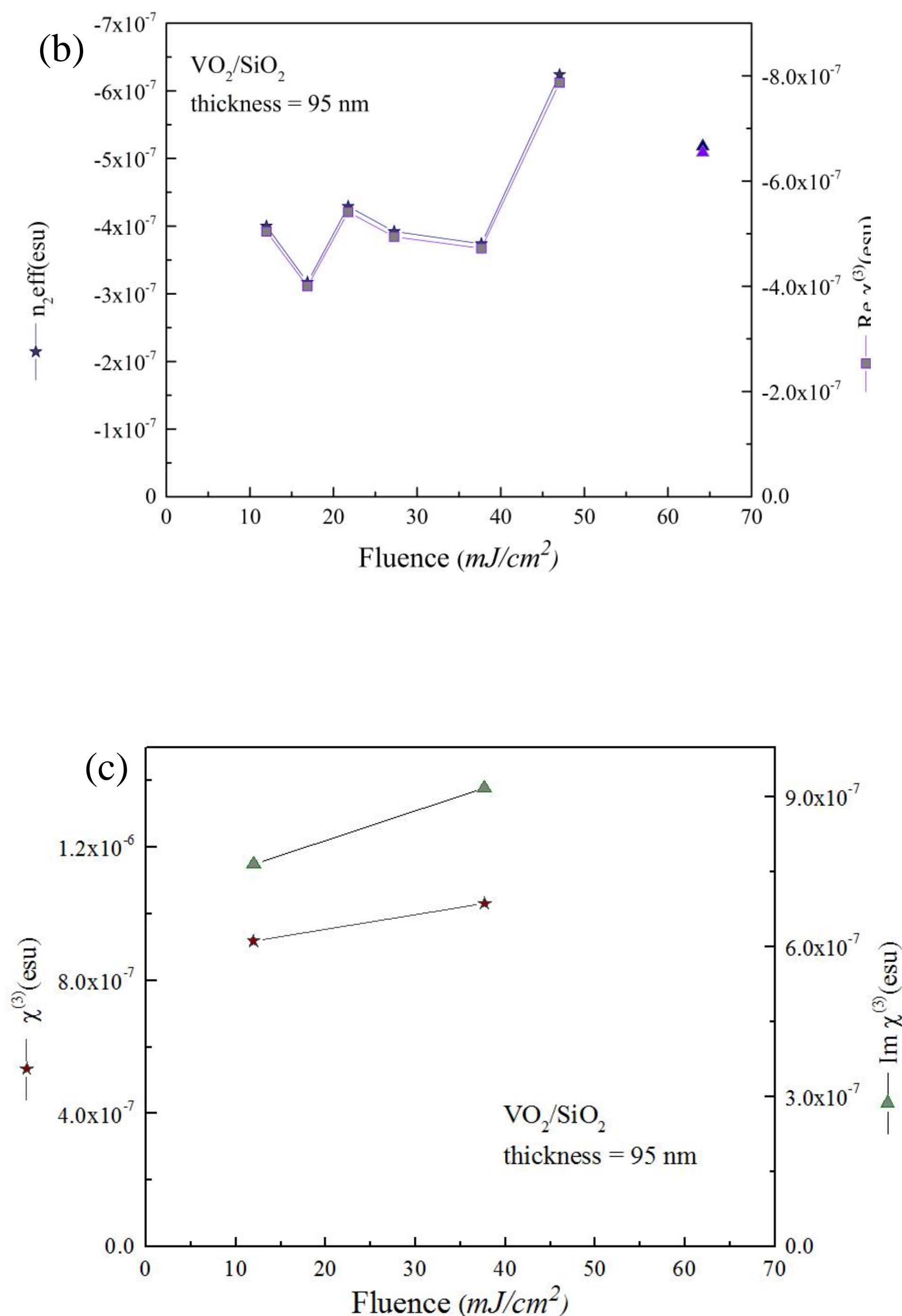

Figure 4.10 (a) Graph of nonlinear index of refraction $\gamma\ (m^2/W)$ as a function of fluence for the 95 nm thick sample. (b) Graph of both $n_2eff(esu)$ and $Re\chi^{(3)}(esu)$ as a function of fluence for the 95 nm thick sample. (c) Graph of both $\left|\chi^{(3)}\right|$ and $Im\chi^{(3)}(esu)$ as a function of fluence for the 95 nm thick sample.

A similar trend is observed for the graphs of nonlinear indexes (γ, n_2eff) and real part of the third order nonlinear susceptibility. Below a fluence value of 38 mJ/cm^2 the optical constants remain in the same order. Below the mentioned fluence value or threshold an average value for both nonlinear indexes of refraction was found to be $\gamma = -6.66x10^{-10}\, cm^2/W$ and $n_2eff = -3.82x10^{-7}esu$. As for the real part of the third order electric susceptibility an average value of $Re\chi^{(3)} = 4.82x10^{-7}\, esu$ was obtained. Above a fluence value of 47 mJ/cm^2 a change in order of ten times for the nonlinear index of refraction γ was observed with a value of $\gamma = -1.09x10^{-9}\, cm^2/W$. This is due to the high fluence of the laser. Similarly at that same fluence a value for the nonlinear index of refraction in esu and the real part of the third order susceptibility was found to be $n_2eff = -6.24x10^{-7}esu$ and $Re\chi^{(3)} = 7.87x10^{-7}\, esu$ with no present change in its order. The points found outside for the graphs represent values found for the nonlinear index of refraction and real part of the third order susceptibility beyond a fluence level were the sample was damaged. As in the case for the 35 nm sample, the trend observed for nonlinearity below the threshold value is from the third order susceptibility $\chi^{(3)}$ and above this fluence the contribution to nonlinearity is from both first order $\chi^{(1)}$ and third order $\chi^{(3)}$ electrical susceptibility. As mentioned before at high fluence levels the electrostriction effect is higher and thus the compression due to the electric field changes the optical constants of the material. For the values below the threshold fluence and average for the nonlinear absorption coefficient was found to be $\beta = 4.9x10^4\ cm/GW$, similarly the average value found for the third order susceptibility is $|\chi^{(3)}| = 6.84x10^{-7}\, esu$. In comparison to the value obtained for the 35 nm thick sample which is in the order 10^{-6} and is ten times bigger than for this sample. Again the reasons for the magnitude of $|\chi^{(3)}|$ are the same as for the other sample explained above.

4.5 Z-Scan Results for VO_2/Al_2O_3 Thin Films in Insulating and Metallic Phase

Closed and open aperture Z-scans measurements for VO_2 in both insulating and metallic states were conducted for the film deposited on different sapphire substrates: VO_2/Al_2O_3 (M-Cut) and VO_2/Al_2O_3 (A-Cut). Data obtained for VO_2/Al_2O_3 (M-Cut) are shown in figure 4.11. At room temperature a self-defocusing Z-scan trace indicative of a negative nonlinear index of refraction can be seen for the closed aperture scan on figure 4.11 (a). As seen before for the amorphous SiO_2 deposited thin films, a fluence dependence on optical nonlinearity is observed. At higher fluence the difference between peak and valley on the transmittance $\left(\Delta T_{p-v}\right)$ is observed. At higher fluences no visible damage of the sample or a visible disk diffraction pattern (indicative of damage) is observed.

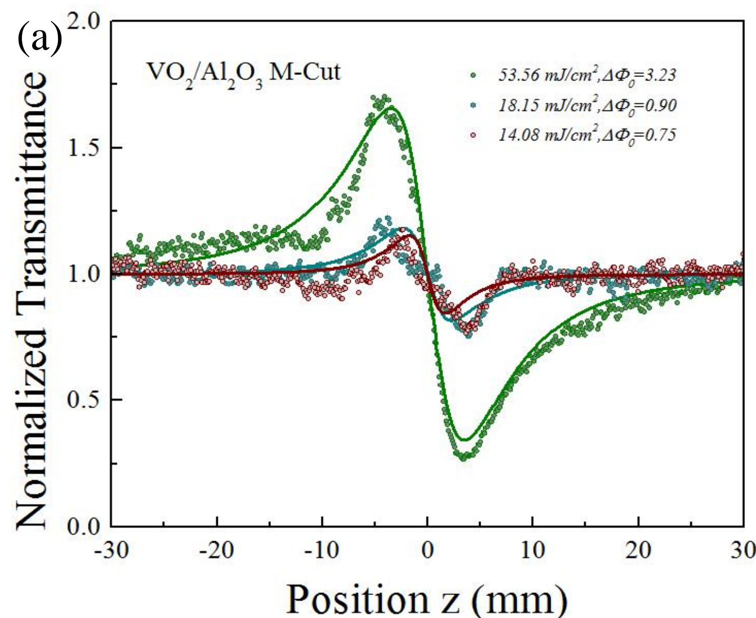

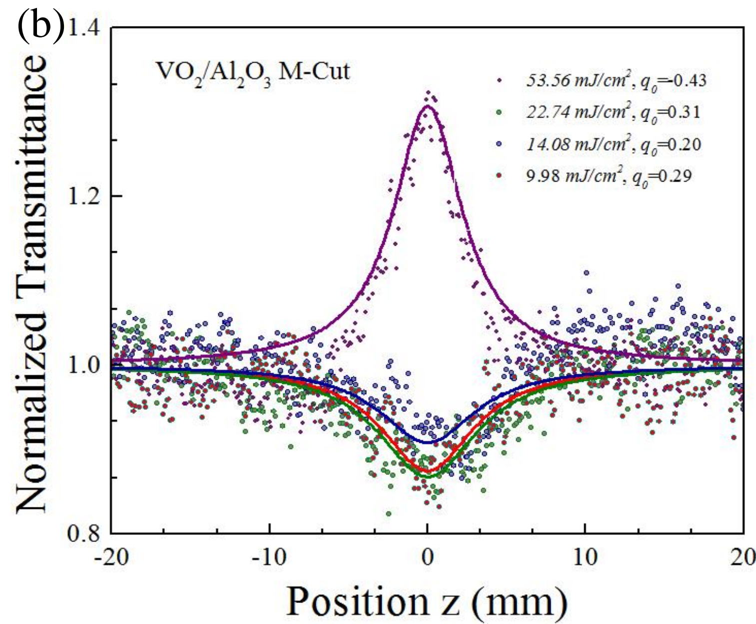

Figure 4.11 (a) Graph of closed aperture Z-scan trace at room temperature for VO_2/Al_2O_3 (M-Cut). (b) Graph of closed aperture Z-scan trace at room temperature for VO_2/Al_2O_3 (M-Cut).

Figure 4.11 (b) shows the open aperture scans of the same sample at different fluences. At lower fluences the typical valley at $z = 0$ can be seen. At higher fluences $(54\ mJ/cm^2)$ this peak is inverted, the reasons for this are attributed to the saturated absorption in photo-induced metallic state, interference effects within the sample some intermediate excited state. Despite this inversion of peak, no film damage was observed.

After measurements were taken at room temperature, the sample was mounted on a heater in order to induce the phase transition thermally and keep the sample in metallic state during z-scan measurements at a temperature of $T = 393\ K$. Figure 4.12 shows both open and closed z-scans for the same VO_2/Al_2O_3 (M-Cut) but in metallic state.

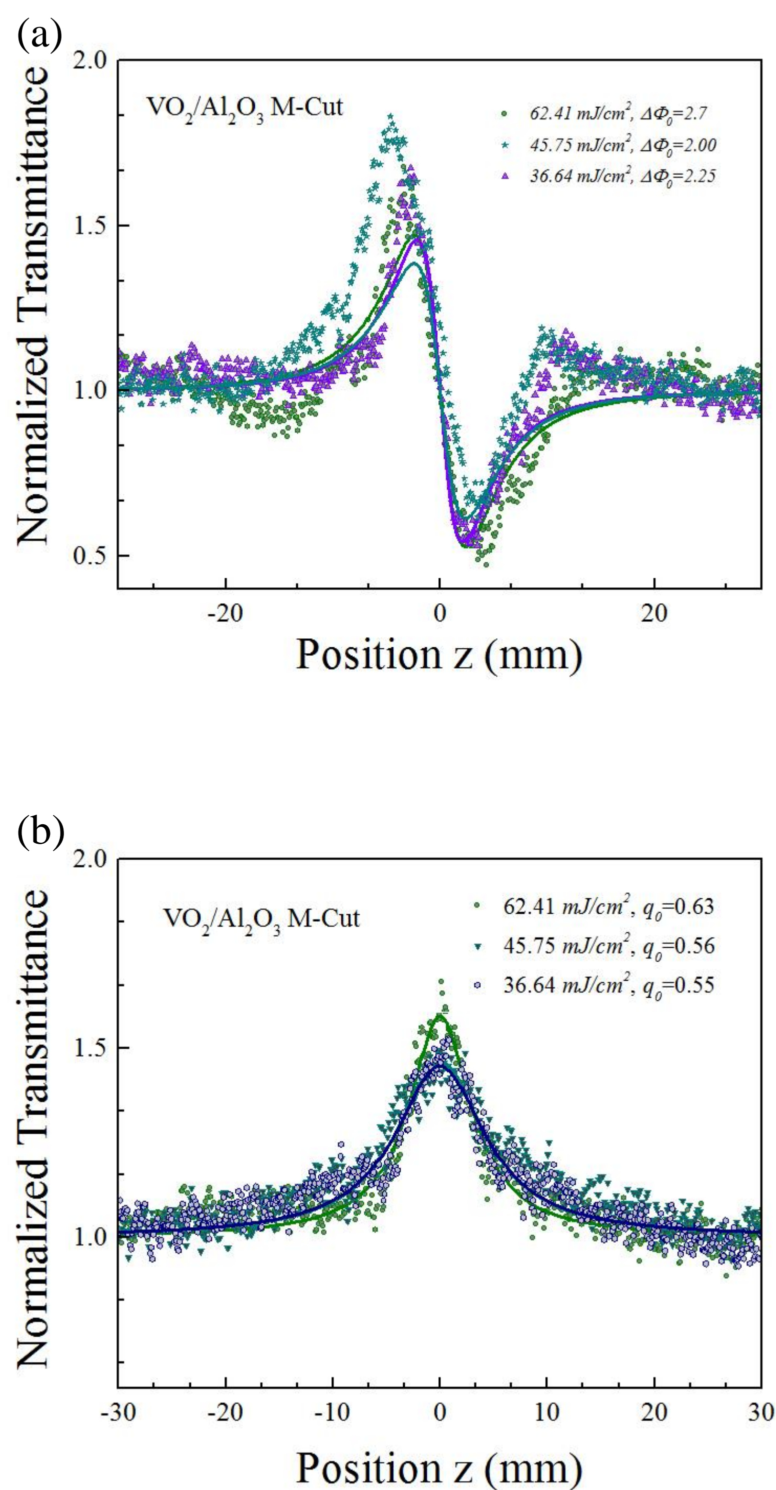

Figure 4.12 (a) Closed aperture Z-scan for metallic VO_2 on $Al_2O_3(M-cut)$. (b) Open aperture Z-scan for metallic VO_2 on $Al_2O_3(M-cut)$.

As seen on figure 4.12 (a) closed aperture Z-scan shows a self-defocusing trace with a negative nonlinear index of refraction. Higher nonlinearity is observed for higher fluences. Despite been in its metallic state the closed aperture scan is similar to the open aperture regarding the peak to valley orientation. Lopez *et al*. reported that after heating the samples to 100 ℃ an inversion to valley peak with self-focusing was observed for his closed aperture scan due to smaller index of refraction of the sample in its metallic state thus creating an effective negative self-focusing [18]. It must be noted that Lopez *et al*. report was based on VO_2/SiO_2 thin films of 210 nm thickness, using 120 fs pulses with a wavelength λ =800 nm in comparison to 30 ps pulses with $\lambda = 532\ nm$ used in our experiments. For figure 4.12 (b) a peak at the focus $(z = 0)$ can be seen for all fluences. As seen in the previous open aperture scan at room temperature were a peak was observed for higher fluences, the peaks observed are caused by the sample being in its metallic form and thus the transmittance increases. Interference effects inside of the film could also give some contribution into the rise to the inversions of the valleys at this temperature. No visible damage was found for this sample during measurements.

Z-scan traces at room temperature for both open and closed aperture for the VO_2/Al_2O_3 (A-Cut) with 60 nm thickness are shown in figure 4.13. At room temperature the similar self-defocusing with a negative nonlinear index of refraction is observed for all fluences. For open aperture figure 4.13 (b) shows one scan at low fluence. The symmetric valley at $z = 0$ is observed. At higher fluences for this sample open aperture scans tended to be noisier and not symmetric, something that is attributed to the alignment of the set up and due to the high noise of the signal.

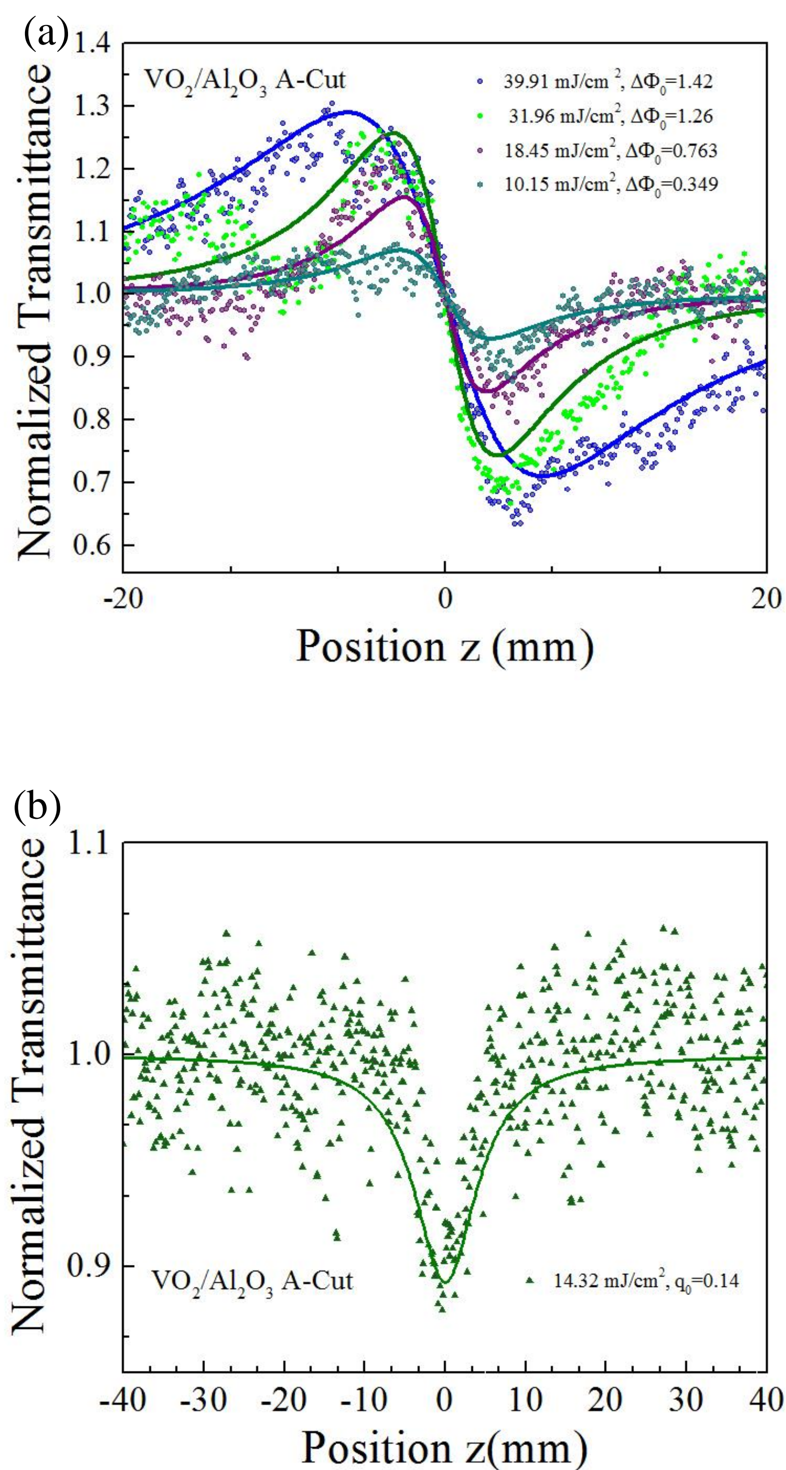

Figure 4.13 (a) Graph of closed aperture Z-scan trace at room temperature for VO_2/Al_2O_3 (A-Cut). (b) Graph of closed aperture Z-scan trace at room temperature for VO_2/Al_2O_3 (A-Cut).

Figure 4.14 shows the open and close aperture scans for the VO_2/Al_2O_3 (A-Cut) film in metallic state.

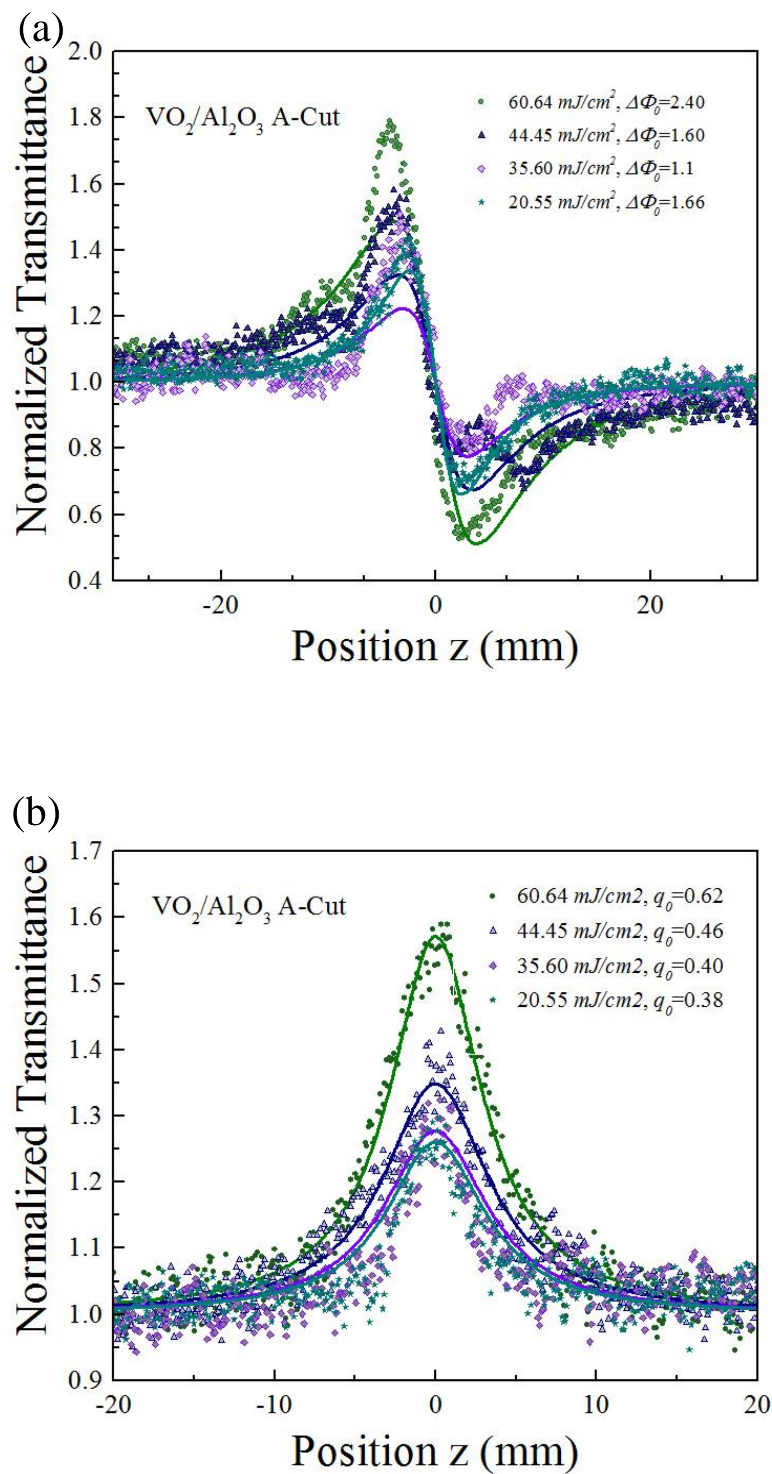

Figure 4.14 (a) Closed aperture Z-scan for metallic VO_2 on $Al_2O_3(A-Cut)$. (b) Open aperture Z-scan for metallic VO_2 on $Al_2O_3(A-Cut)$.

Again, the typical self-defocusing trace is observed for this sample in its metallic phase. No inversion of the peak-valley symmetry was observed above the PT temperature and no visible damage was found for higher fluences. For the case of open aperture a symmetric peak was observed at $z = 0$ for all fluences. As mentioned before the sample is in its metallic state and thus an increase of the transmittance was found. No visible damage was found or visible disk diffraction pattern indicative of damage in the sample was observed.

As in the case for the VO_2/SiO_2 thin films, parameters obtained from the closed aperture fit $(\Delta\Phi_0,\ \Delta T_{p-v})$ and Rayleigh range for both cases were plotted as a function of fluence at room temperature.

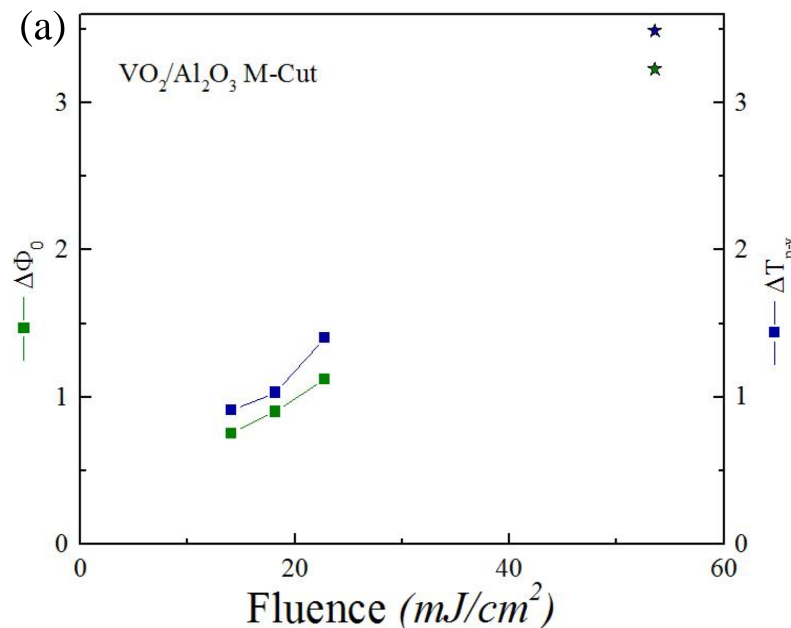

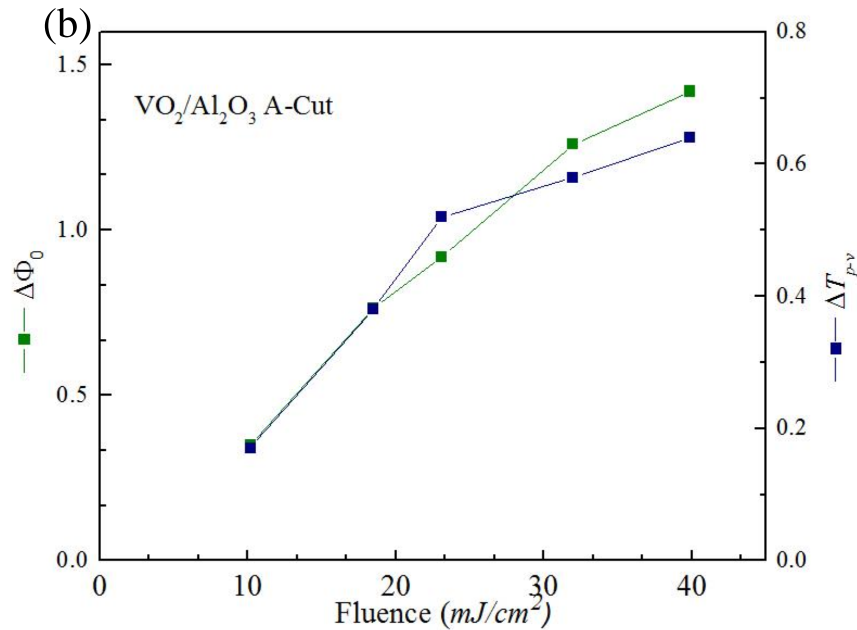

Figure 4.15 $\Delta\Phi_0$ and ΔT_{p-v} as a function of fluence at room temperature for VO_2/Al_2O_3 (a) is for the M-cut thin film, (b) is for the A-cut thin film.

From figure 4.15 (a), a linear behavior can be seen for fluences below 23 mJ/cm^2. After this fluence value the points seen on the graph are points corresponding to the sample being in an intermediate phase as explained before. At the fluence of 54 mJ/cm^2 closed aperture scans stay with the same peak to valley profile but the open aperture scan at this fluence is inverted due to the high fluence, thus validating the fact that the material may not be in its insulating phase anymore. For the A- cut film a linear behavior is observed with no points been out of the graph. No damage that results in permanent disk diffraction pattern was observed for this sample.

Figure 4.16 shows the Rayleigh range fitting constant z_0 for both open and closed aperture for both thin films at different fluences.

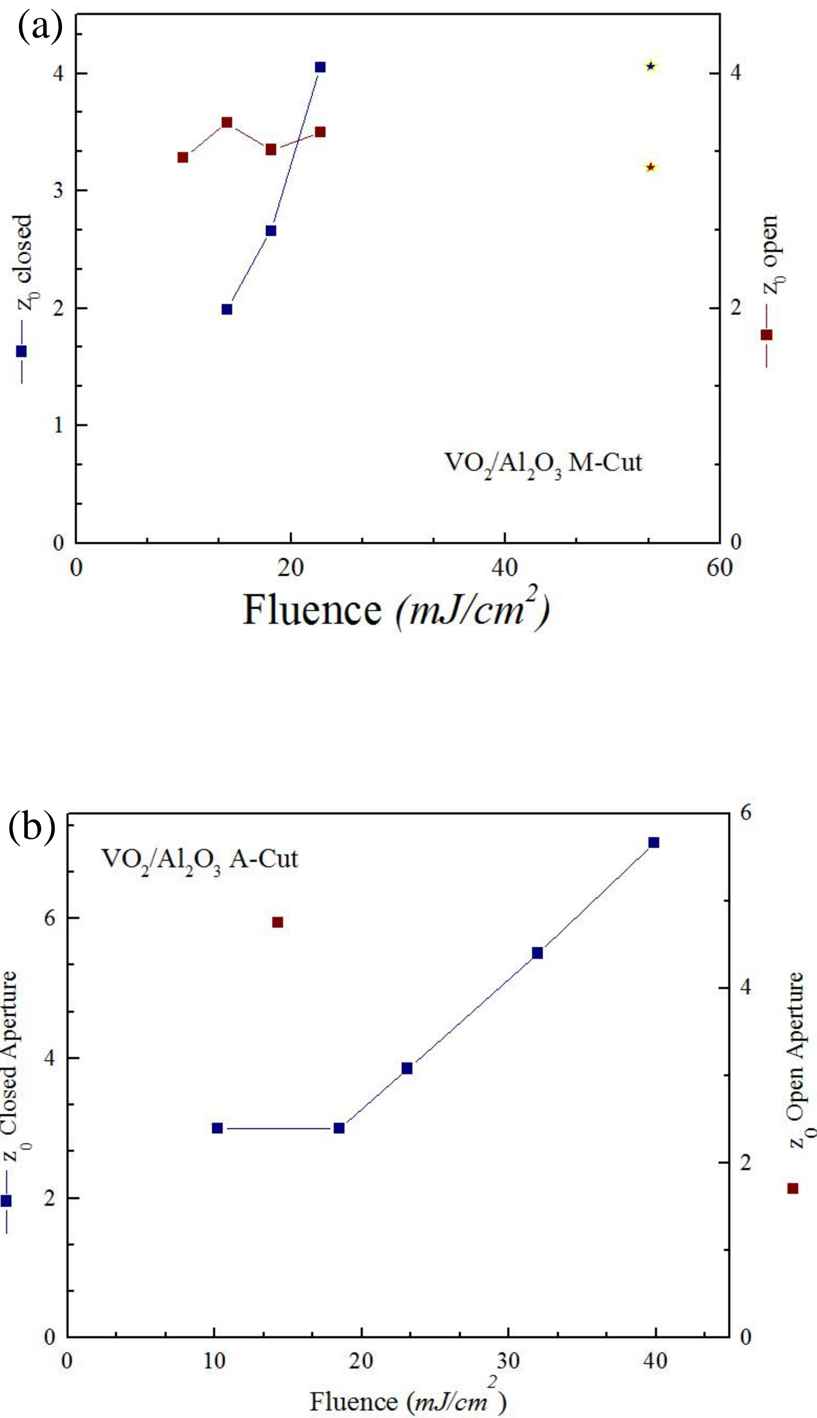

Figure 4.16 Rayleigh range fitting constantz_0 for both open and closed aperture as a function of fluence at room temperature for VO_2/Al_2O_3 (a) is for the VO_2/Al_2O_3 (M-cut) thin film, (b) is for the VO_2/Al_2O_3 (A-cut) thin film.

The increased of the z_0 parameter seen for both samples can be attributed to the change in the material due to the laser pulse and its increasing fluence. For figure 4.16 (a) the point at fluence of $54\ mJ/cm^2$ is the point where the sample is no longer in its insulating phase as previously stated. For the open aperture the Rayleigh range remains constant until the fluence value mentioned before where the sample may be in its intermediate phase. As for the case of open aperture shown in figure 4.16 (b) only one point is shown in the graph, this is due to the high noise of the scans and since the Rayleigh range parameter z_0 is less accurate at lower laser fluence.

Figure 4.17 (a) and (b) shows plots of both nonlinear indexes of refraction and third order electric susceptibility as a function of fluence for the VO_2/Al_2O_3 (M-cut) sample at room temperature.

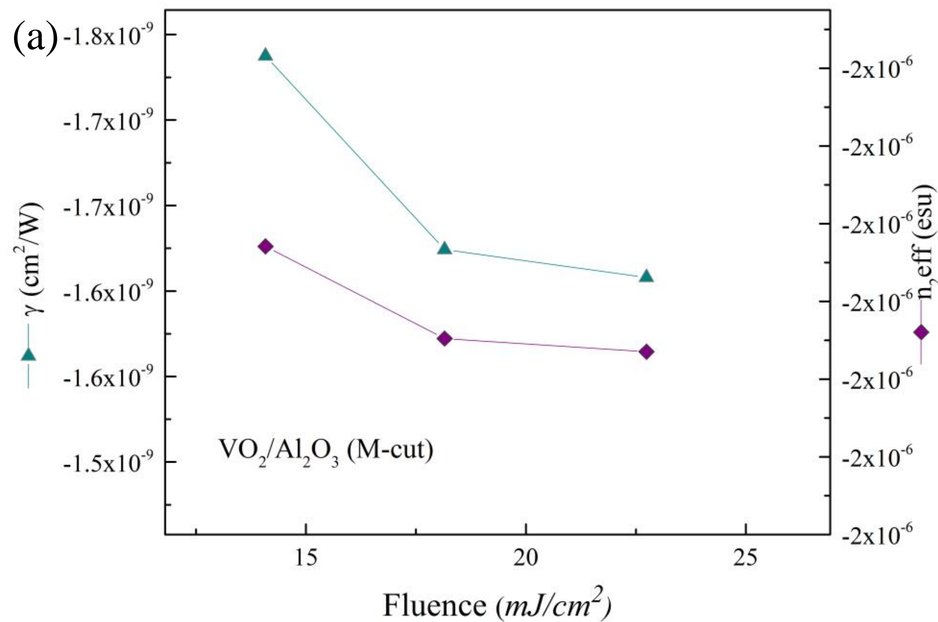

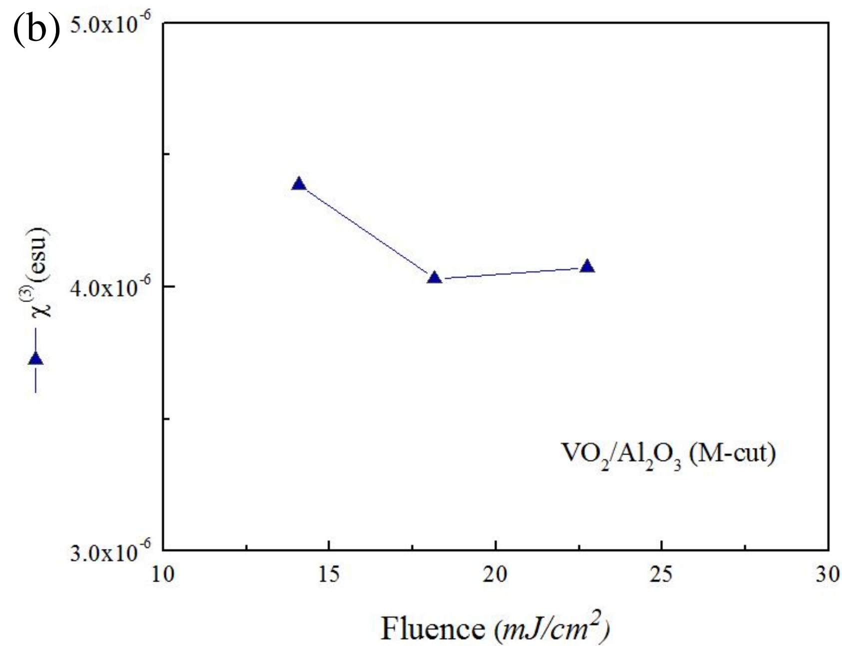

Figure 4.17 (a) Graph of nonlinear index of refraction $\gamma\ (m^2/W)$ and $n_2eff(esu)$ as a function of fluence for the VO_2/Al_2O_3 (M-cut) sample below the PT temperature. (b) Graph of the third order nonlinear susceptibility $\chi^{(3)}(esu)$ as a function of fluence for the VO_2/Al_2O_3 (M-cut) sample below the PT temperature.

An average value for both nonlinear indexes was found to be $\gamma = -1.7x10^{-9}\ cm^2/W$ and $n_2eff = -1.78x10^{-6}esu$. From the open aperture scans, the calculated value of the nonlinear absorption coefficient is $\beta = 3.8x10^4\ cm/GW$. Similarly the magnitude of the third order nonlinear susceptibility was calculated and a value of $|\chi^{(3)}| = 4.16x10^{-6}\ esu$ was found.

For the same sample in metallic phase, at temperature above T_C optical constants are shown in figure 4.18. A value of $\gamma = -1.94x10^{-9}\ cm^2/W$ which is in the same order as for the insulating phase, similarly a value of $n_2eff = -1.25x10^{-6}esu$ was calculated. A higher value for the nonlinear absorption coefficient $\beta = 5.7x10^4\ cm/GW$ and the third order nonlinear susceptibility $|\chi^{(3)}| = 3.61x10^{-6}\ esu$ are obtained.

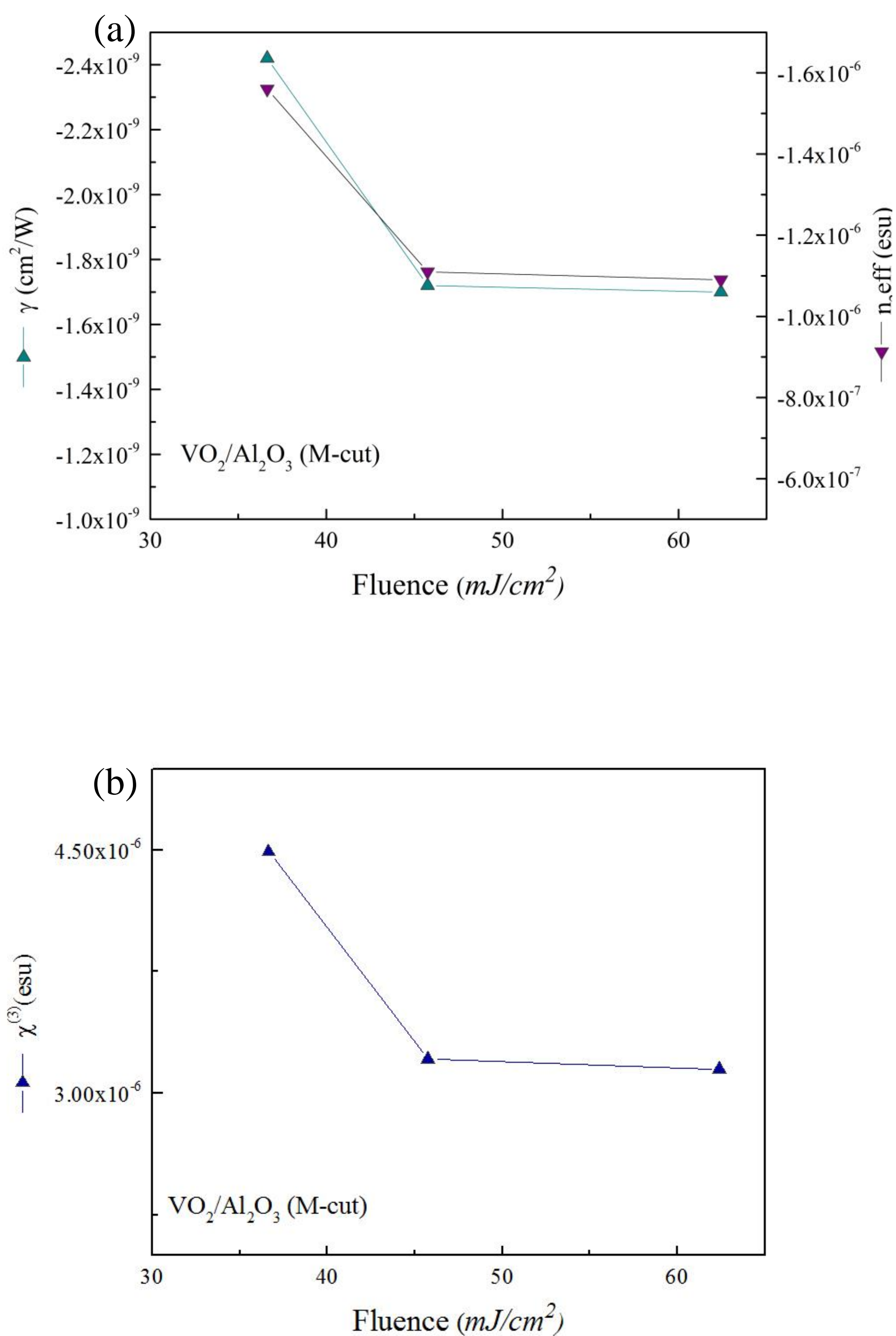

Figure 4.18 (a) Nonlinear index of refraction $\gamma\ (m^2/W)$ and $n_2eff(esu)$ as a function fluence for the VO_2/Al_2O_3 (M-cut) sample in its metallic state. (b) Third order nonlinear susceptibility $|\chi^{(3)}|(esu)$ as a function of fluence for the VO_2/Al_2O_3 (M-cut) sample in its metallic state.

For the VO_2/Al_2O_3 (A-cut) sample figure 4.19 shows the optical constants obtained for VO_2 in insulating phase at room temperature of the sample. Average values for nonlinear optical constants were obtained to be $\gamma = -1.35x10^{-9}\,cm^2/W$ and $n_2eff = -1.41x10^{-6}esu$, $\beta = 5.1x10^4\ cm/GW$ and $\left|\chi^{(3)}\right| = 3.39x10^{-6}\ esu$.

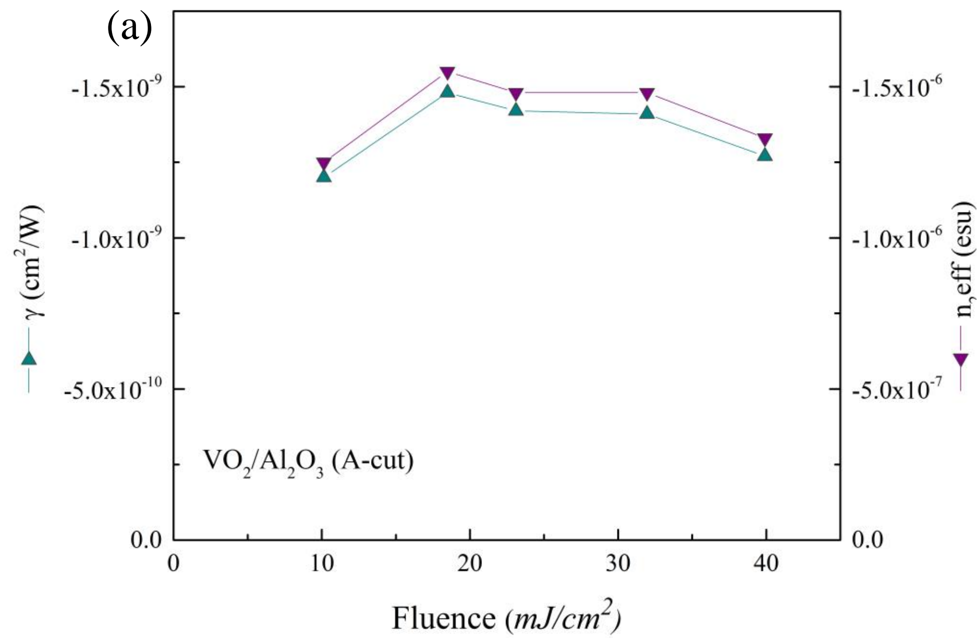

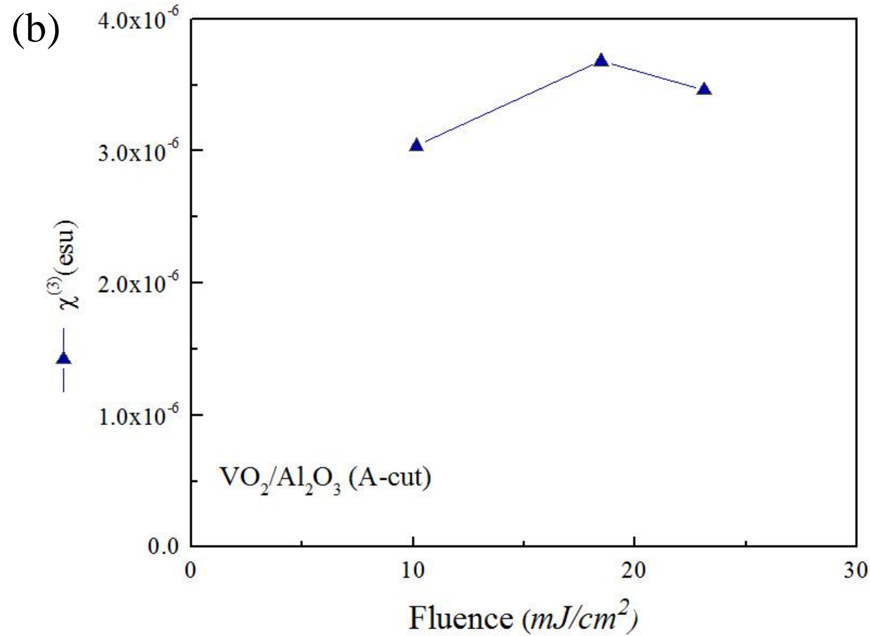

Figure 4.19 (a) Graph of nonlinear index of refraction $\gamma\ (m^2/W)$ and $n_2eff(esu)$ as a function of fluence for the VO_2/Al_2O_3 (A-cut) sample below the PT temperature. (b) Graph of the third order nonlinear susceptibility $|\chi^{(3)}|(esu)$ as a function of fluence for the VO_2/Al_2O_3 (A-cut) sample below the PT temperature.

Figure 4.20 shows the same graphs as before but above the PT temperature for the A-cut sample. Average values for both indexes were obtained to be $\gamma = -1.35x10^{-9}\ cm^2/W$ and $n_2eff = -1.23x10^{-6}esu$ which is the same value obtained for γ in its insulating phase, $\beta = 5.6x10^4\ cm/GW$ with no bigger difference from the insulating phase value and $|\chi^{(3)}| = 2.53x10^{-6}\ esu$ was found, a smaller value but still in the same order in comparison to its insulating phase.

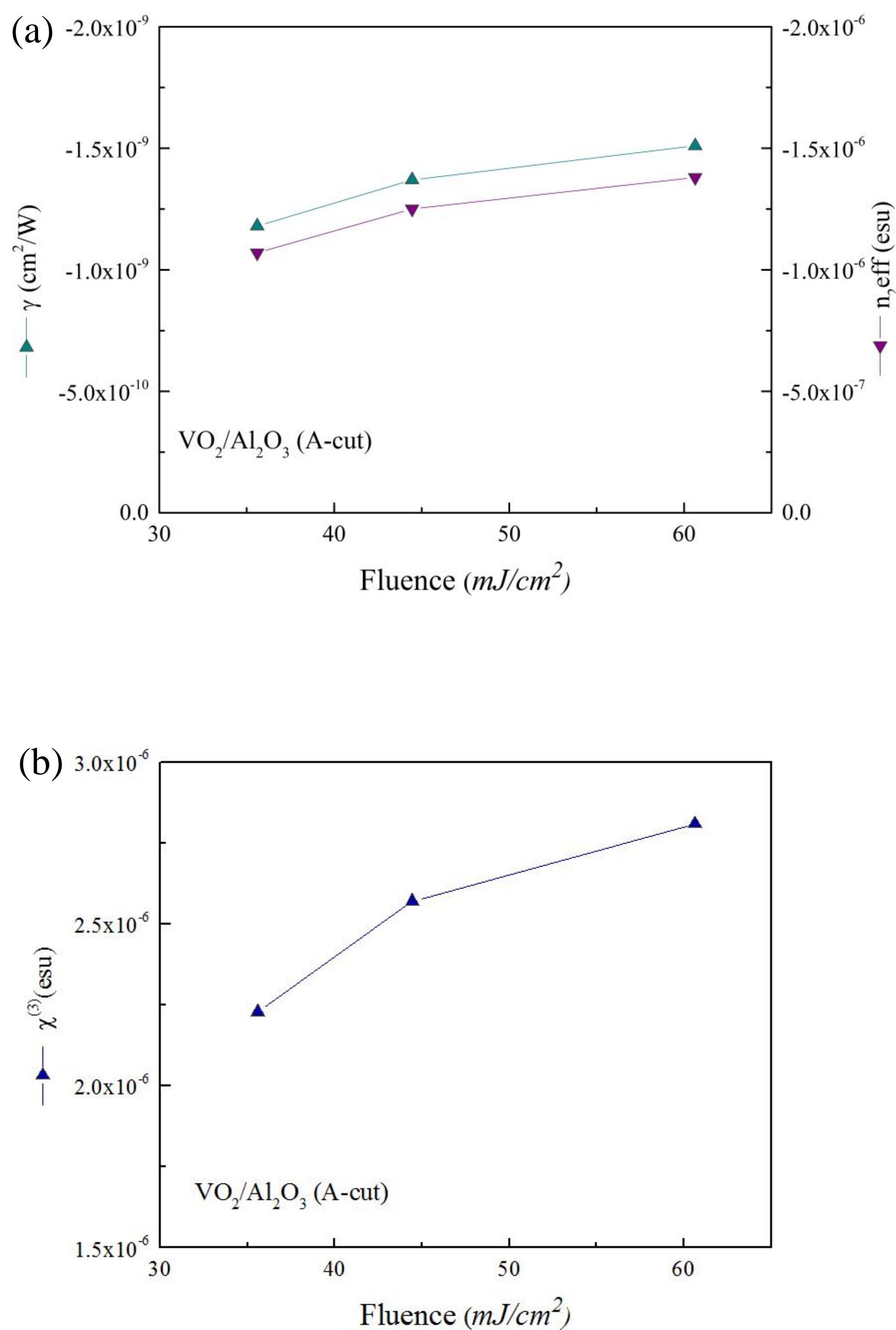

Figure 4.20 (a) Nonlinear index of refraction $\gamma\ (m^2/W)$ and $n_2eff(esu)$ as a function fluence for the VO_2/Al_2O_3 (A-cut) sample in its metallic state. (b) Third order nonlinear susceptibility $|\chi^{(3)}|(esu)$ as a function of fluence for the VO_2/Al_2O_3 (A-cut) sample in its metallic state.

Results obtained for the nonlinear index of refraction and nonlinear absorption coefficient are quite of higher magnitude in comparison to other materials. Typical Z-scan results on semiconductors have shown values for the nonlinear index of refraction of similar orders. Results by Dvorak *et al.* [59] on $GaAs$ using Z-scan technique with 100 ps pulses have yielded a value for the nonlinear index of refraction in the order of $10^{-12}\ cm^2/W$. Using ns pulses with λ =1550 nm and fs pulses with λ =830 nm Hernández *et al.* [60] showed that the nonlinear index of refraction for Si thin films was in the order of $10^{-8}\ cm^2/W$ for ns pulses, a result that is 10 times bigger than the value reported on this work for VO_2. As previously stated Lopez et al. [18] reported values for the nonlinear index of refraction in the order of $10^{-12}\ cm^2/W$ for VO_2 thin films and nanoparticles using fs pulses. In our work the relatively long 30 ps laser pulses give rise to electrostriction, and very likely produce switching of VO_2 into an intermediate state during the pulse interaction in both, insulating and metallic states. For insulating VO_2 the evolution of optical constants versus laser fluence indicates that the pure insulator-to-metal transition becomes to be noticeable at laser fluences above 15 mJ/cm^2.

4.6 Scattering Results for VO_2/Al_2O_3 (R-cut and C-cut)

Scattering data was obtained for highly oriented epitaxial films of VO_2/Al_2O_3 (R-cut and C-cut). Figure 4.21 shows the BSDF indicatrices of hemispherical light scattering for the R-cut, 30 nm thick film as a function of both polar θ and azimuthal φ angles.

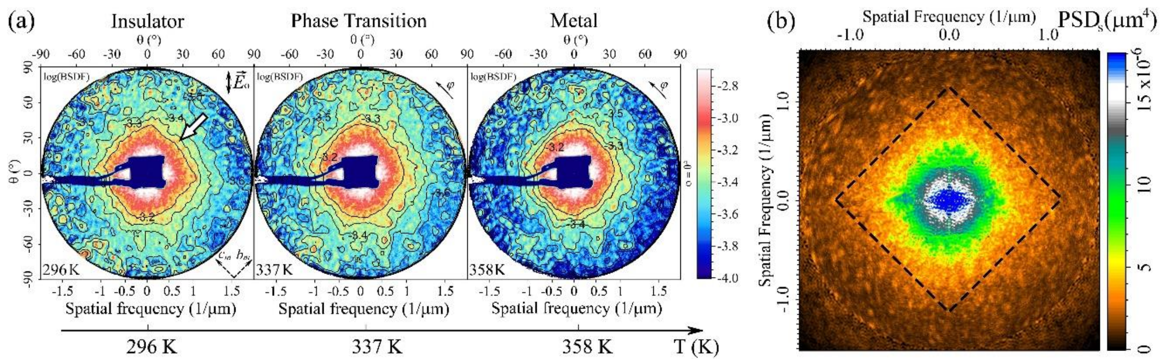

Figure 4.21 (a) Temperature dependent evolution of light scattering indicatrix for 30 nm thick film VO_2/Al_2O_3 (R-cut). Arrow marks square like pattern at $T = 296\ K$. (b) Power spectral density of the surface at $T = 296\ K$. Central and periphery region was reconstructed using the Gerchberg-Saxton ER algorithm.

From figure (a) a square like pattern of equal intensity points can be observed in the central area within $0^\circ < \theta < 55^\circ$. These points are parallel to the (010) and (001) planes on the epitaxial film. The sharpness of the lines is lost at larger angles. At $\varphi = 90^\circ$ and 270°an elongation of such lines is observed, this is due to the polarization anisotropy of the scattering process, since the polarization was oriented along the azimuthal angle. From (b) the PSD of the surface calculated from the scattering indicatrix eliminates this polarization effect. Still the pattern of same intensity lines remains in the center of the PSD. This in turn indicates the highly orientation of the film.

To further demonstrate that the texture of the films is dependent on the substrate and film thickness figure 4.22 shows scattering indicatrices for VO_2/Al_2O_3 C-cut 50 nm and 30 nm thin

films. These films undergo 3 fold twinning by previous XRD results. From the figure symmetric directions of scattering can be observed with 60° separation. Due to the higher orientation of the R-cut film it makes it an optically isotropic film with a local morphology more uniform than that of the C-cut.

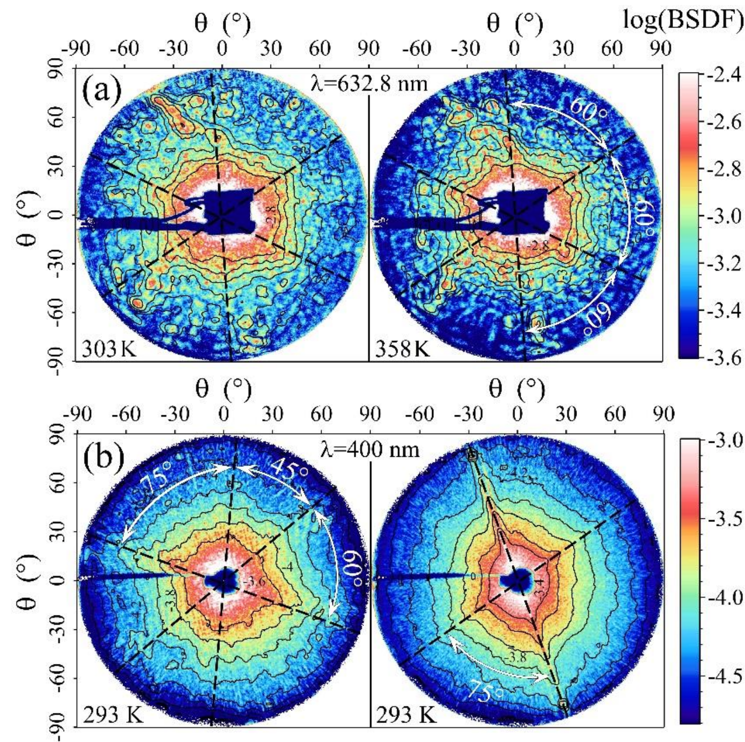

Figure 4.22 Light scattering for VO_2/Al_2O_3 C-cut thin films. (a) log(BSDF) for 50 nm thick film in insulating and metallic state. (b) log(BSDF) for different areas of 30 nm thick film. Dashed lines indicate preferential directions of scattering.

Figure 4.23 shows the AFM date for the 30 nm thick VO_2/Al_2O_3 (R-cut) film with the surface ACF_{AFM} and PSD as a function of the spatial frequency. From AFM a value for the rms roughness of the surface was obtained as $\delta = 96$ Å. From figure (a) a rectangular shape on the lateral grains of VO_2 can be observed. The average size for the VO_2 grains is $d_{av} \cong 305\ nm$ which corresponds

to a spatial frequency $f_g = {}^{1}/_{d_{av}} = 3.3\ \mu m^{-1}$. This value cannot be obtained in the scattering measurements since the maximum allowed spatial frequency by the He-Ne laser is $f_{max} = 1/\lambda = 1.58\ \mu m^{-1}$. But from figure 4.22 (a) the observed square like pattern at $\theta < 55^{\circ}$ corresponding to a spatial frequency of $f < 1.3\ \mu m^{-1}$ indicates that the VO_2 crystallites are organized into highly ordered clusters. Above 55° the pattern is more distorted due to the increased randomness in orientation of smaller surface irregularities.

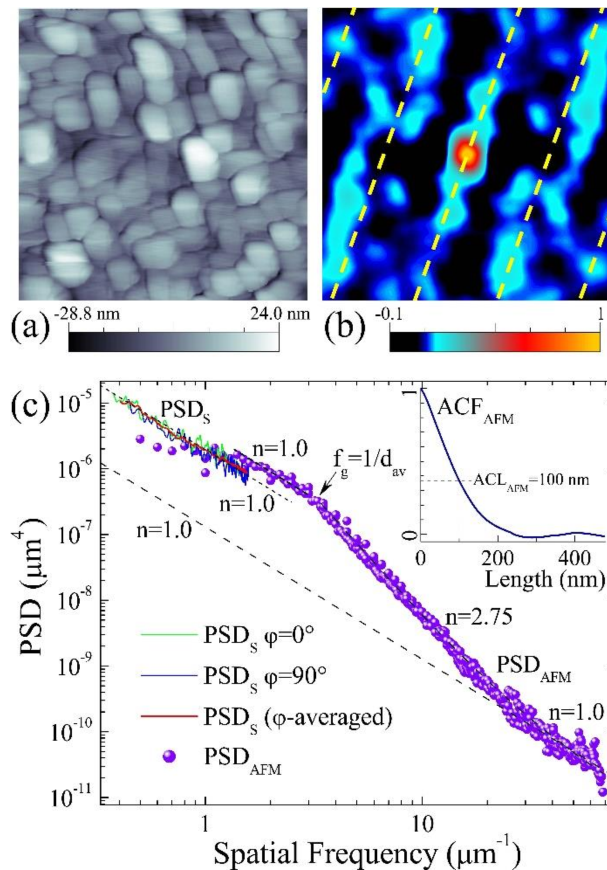

Figure 4.23 Morphology of the 30 nm thick film of VO_2/Al_2O_3 (R-cut). (a) $2x2\mu m^2$ AFM topography and (b) $2x2\mu m^2$ surface autocorrelation function ACF_{AFM}. Periodical fringes are marked by dashed lines. (c) Power spectrum extracted from AFM and light scattering data at $T = 296\ K$. Dashed lines are fit from equation (2.35). The inset shows a cross section of 2D ACF_{AFM}.

From figure 4.25 (b) the autocorrelation function calculated from the AFM topography is presented. A high presence of isotropic and weak anisotropic components can be seen. From the AFM data one can characterize the scattering indicatrix from figure 4.21 (a) for VO_2/Al_2O_3 R-cut as fractal surface scattering, where the scattered field or pattern contains information about the subwavelength VO_2 crystallites organized into highly ordered square like structures due to the anisotropic ordering on the single crystal R-cut substrate [3].

Using the PSD_{AFM} and PSD_S calculated from AFM and scattering data one is able to obtain information about the fractal properties of the sample. From figure 4.23 (c) one can see the overlap between the PSD_{AFM} and PSD_S. The slope of the PSD_{AFM} and PSD_S coincide within $f = 1.4 - 3.0\mu m^{-1}$. Therefore both techniques (AFM and light scattering) yield the same information about the fractal dimension surface. Below $f = 1.3\ \mu m^{-1}$ the PSD_{AFM} has fewer data points, and thus the accuracy of AFM measurements is slightly lower as compared to higher frequencies.

From the inset on figure 4.24 (a) the averaged power spectra PSD_s for the 30 nm thick film shows a difference between the slope for the insulating phase and metallic phase. This in turn indicates a smoothing of surface irregularities during the metallic phase. From 4.24 (a) the surface BSDF(f) is the scaled down PSD function. For this reason a statistical distribution of surface inhomogeneity's can be obtained directly from the data of the BSDF. Therefore this method functions as a scatter prediction that allows reconstruction of the evolution of surface irregularities.

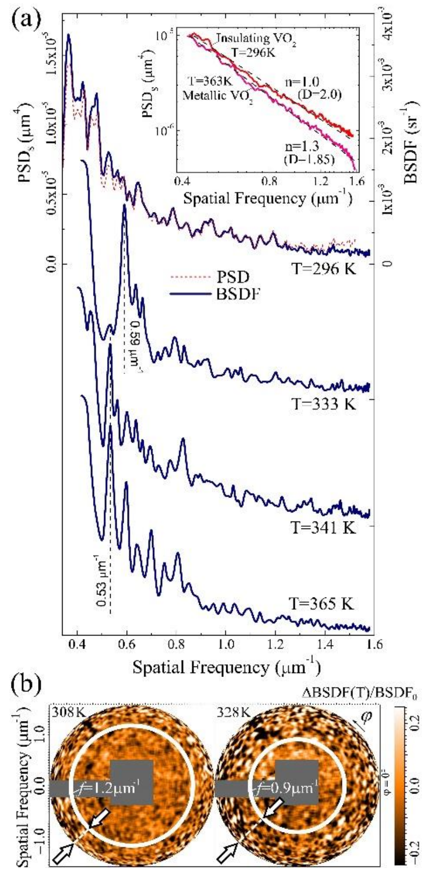

Figure 4.24 Evolution of scattering pattern and PSD of the surface roughness for the 30 nm thick VO_2/Al_2O_3 R-cut. (a) Cross sections of the BSDF scattering indicatrix and PSD_s at $\varphi = 0^{\circ}$. Inset shows the azimuthally averaged PSD_s function for insulating and metallic phases. Dashed lines are fit. (b) The relative change $\Delta BSDF(T)/BSDF_0$ near the PT point, where $BSDF_0$ is obtained for insulating phase and $\Delta BSDF(T) = BSDF(T) - BSDF_0$. Arrows mark the region of noticeable emergence of diffraction peaks.

New diffraction peaks can be observed in figure 4.24(b) at higher spatial frequencies above $f = 1.2\ \mu m^{-1}$. Anisotropic domains form with sizes less than $d = 1/f = 0.83 \mu m^{-1}$. As the temperature increases the region that is affected by the phase transition uniformly spreads to $f = 0.9\ \mu m^{-1}$. As the temperature increases new diffraction peaks fill up the scattering indicatrix. Thus

this temperature dependent process corresponds to the realignment of domains and it is different from sample to sample.

Figure 4.25 shows the ACF_s distribution for insulating and metallic phases versus the translation length. From the figure the distinctive feature of such ACF_s is the presence of spatial oscillations with ordered maxima due to domain formation in the epitaxial film.

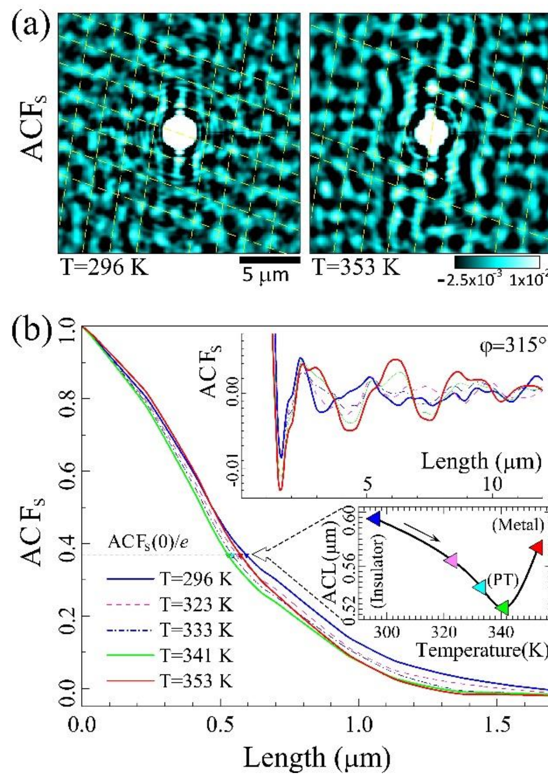

Figure 4.25 (a) Autocorrelation function of VO_2 surface for insulating phase at T=296 K and metallic phase (T=353 K). (b) Cross section of ACF_S distribution at different temperatures. Upper inset shows oscillatory component of ACF_s. Lower inset shows evolution of autocorrelation length versus temperature.

From figure 4.25 (a) in insulating phase the maxima are aligned in a mesh like pattern separated by 2.2 μm. This structure of ACF_s is very similar to the one presented in figure 4.23 for the ACF_{AFM} separated by 0.55 μm.

The measure of surface inhomogeneity can be referenced to the autocorrelation length (ACL) of the surface. The autocorrelation length is defined as the autocorrelation function halfwidth at the $ACF(0)/e$ point. It is related to the uniform isotropic component of roughness and is calculated from the central peak of ACF map [3]. The ACL from AFM, ACL_{AFM} = 100 nm is five times less than the ACL from the surface ACL_S = 595 nm. As the temperature increases the ACL_S decreases and reaches a minimal point at exactly 529 nm at the phase transition critical temperature of $T_C = 341\ K$. This in turn means a gradual increase of disorder in the VO_2 film. But passed the critical temperature the ACL_S recovers to 574 nm. From figure 4.25 (a) in the metallic phase the maxima are not strictly aligned in a mesh as in the insulating phase. The average separation between maxima in the metallic phase shrinks to 1.8 μm which indicates noticeable surface reconstruction.

4.7 Ultrafast Light Scattering Results for VO_2/Al_2O_3 and VO_2/SiO_2 Thin Films

Using femtosecond angle-resolved light scattering technique, the relation between morphology of VO_2 film and size-dependent PT dynamics on the mesoscale was studied. Figure 4.26 shows the thermally induced scattering indicatrix for both VO_2 films deposited over Al_2O_3 and SiO_2. The BSDF indicatrix for VO_2/Al_2O_3 (figure 4.26- a) shows numerous diffraction peaks due to the presence of twinned ferro-elastic domains in the strained epitaxial film. As for the non-epitaxial VO_2/SiO_2 film, these peaks are not present.

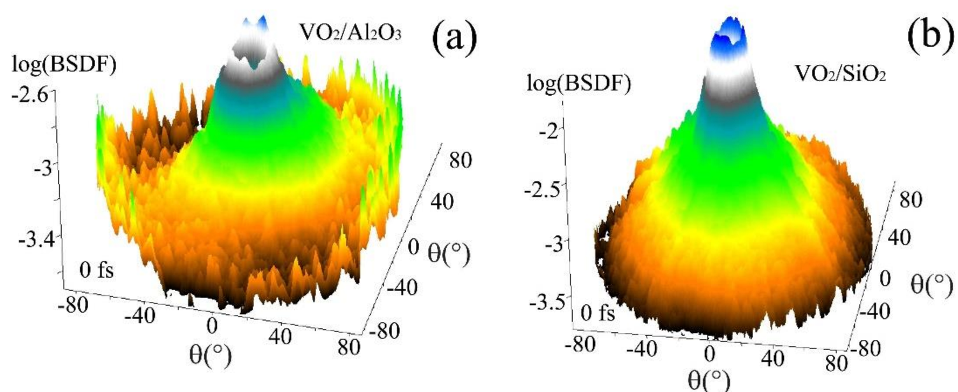

Figure 4.26 Thermally induced BSDF indicatrix for (a) VO_2/Al_2O_3 and (b) VO_2/SiO_2 thin films.

Figure 4.27 shows the evolution of the relative change $\Delta BSDF(t)/BSDF(0)$ for VO_2/Al_2O_3 and VO_2/SiO_2 thin films in both insulating and metallic phase.

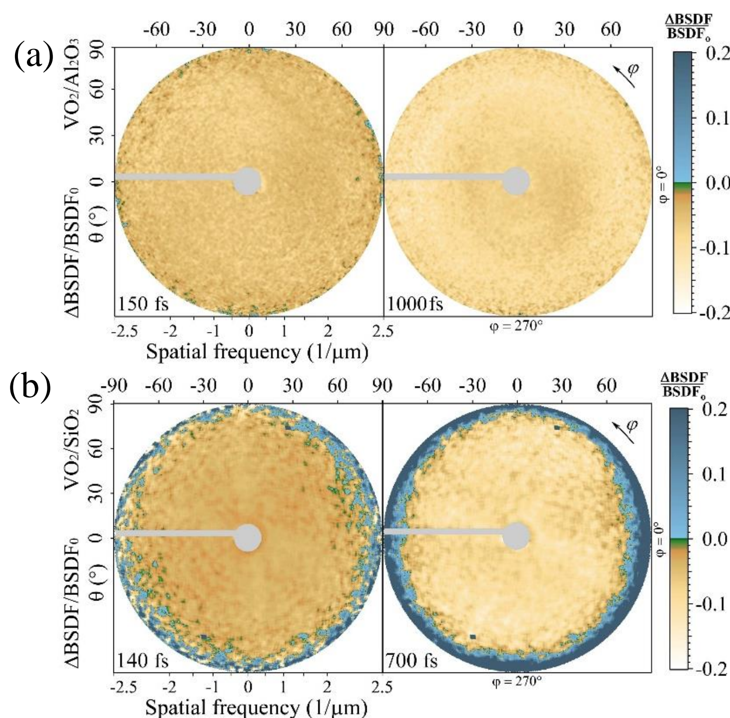

Figure 4.27 Relative change $\Delta BSDF(t)/BSDF(0)$ of the scattering signal upon light induced PT for (a) VO_2/Al_2O_3 and (b) VO_2/SiO_2 thin films; $\Delta BSDF(t) = \Delta BSDF(t) - \Delta BSDF(0)$.

In the central part of the scattering indicatrix for VO_2/Al_2O_3 (figure 4.27 (a)), at lower polar angles $\approx 15°$ ($f = 0.65\,\mu m^{-1}$), the PT rate was found to be ~55% faster than for $\theta \approx 90°$ ($f = 2.5\,\mu m^{-1}$). Comparing the scattering indicatrices with atomic force microscopy data shows that the higher PT rate occurs in the largest VO_2 grains, which are expected to have lower structural defects. This further gives more evidence that that the transient optical properties and the PT dynamics both depend on local crystallinity of the film on the mesoscale.

In contrast the evolution of $\Delta BSDF(t)/BSDF(0)$ for VO_2/SiO_2 (figure 4.27 (b)) shows different qualitative behavior below and above $\theta \approx 70°$ ($f = 2.35\,\mu m^{-1}$). The increase of the scattering intensity at higher polar angles for this sample originates from growing structural imperfections. A major difference between the PT dynamics for both epitaxial VO_2/Al_2O_3 and non-epitaxial VO_2/SiO_2 films. Taking into account the evolution of the dielectric constant during the PT from $\varepsilon_i = 7.38 + i5.5$ to $\varepsilon_m = 4.71 + i5.46$ for probe wavelength $\lambda = 400\ nm$ [11], the estimation shows a decrease of scattering cross section over 35% as the VO_2 film switches from insulating to metallic stage. Thus depending on the film morphology, dielectric constants can vary significantly for different samples, and the change of scattering signal during PT process can be reduced to several percent only. Still, the tendency of the light scattering to diminish upon the light induced I-M PT remains pure for VO_2. Thus the increase of the scattering intensity for the VO_2/SiO_2 film above $\theta \approx 70°$ ($f = 2.35\,\mu m^{-1}$) is a consequence of increased local optical inhomogeneity of the film, and not a result of the uniform change of the dielectric constant as VO_2 changes from insulator to metal.

The optical inhomogeneity of the film during the PT process could originate from several factors such as non-stoichiometry of VO_2, partial nucleation of VO_2 sites or from the film twinning

and geometrical reconstruction of the surface. It is proposed that the most probable origin of the transient increase of the scattering signal in VO_2/SiO_2 is the non-stoichiometry of smaller grains with spatial frequencies $f > 2.35\ \mu m^{-1}$. The non-epitaxial growth of VO_2 on SiO_2 results in a quite disordered structure with numerous oxygen vacancies and other point like defects. The concentration of structural defects is higher in the smallest grains of the films.

Chapter 5 Conclusion

Using a single beam technique we have characterized the nonlinear absorptive and refractive properties of VO_2 thin films of varying thickness and substrate. From open and closed aperture graphs of transmittance as a function of position we have been able to deduce the nonlinear index of refraction and nonlinear absorption coefficient of the material. The closed aperture Z-scan results with 30 picosecond pulses and $\lambda = 532\ nm$ revealed self-defocusing characteristics for both VO_2/SiO_2 and VO_2/Al_2O_3 thin films. Closed aperture Z-scans for VO_2/Al_2O_3 in insulating and metallic states did not show a self-focusing effect as expected, instead a self-defocusing of laser beam was observed.

Open aperture scans for the study of the nonlinear absorptive properties of the material revealed a decrease of transmittance below a certain fluence threshold for the VO_2/SiO_2 samples. Interference effects inside of the film along with light-induced phase transition of the material may contribute to the sudden rise of the transmittance above the fluence threshold. Effective values for both the nonlinear index of refraction and nonlinear absorption coefficient where extracted from fitting of open and closed aperture scans. A value in the order of 10^{-9}~$10^{-10}\ cm^2/W$ was obtained for both VO_2/SiO_2 and VO_2/Al_2O_3 thin films. The difference in order of magnitude for the nonlinear index of refraction reported on this work with the literature is due to the electrostriction effect caused by the picosecond pulse which in turn causes the optical constants of the material to change, and due to possible switching of VO_2 into an intermediate excited state during laser pulse interaction. From nonlinear optical constants, the third order nonlinear electrical susceptibility was obtained for both VO_2/SiO_2 and VO_2/Al_2O_3 thin films. A value of $\left|\chi^{(3)}\right|$ in the order of 10^{-6}~10^{-7} (esu) was obtained from calculations. For the VO_2/Al_2O_3 thin films in both

insulating and metallic phase, no significant difference in the order of magnitude for the third order nonlinear susceptibility $|\chi^{(3)}|$ was observed. Both phases yielded a same value in the order of 10^{-6} (esu). In contrast to past publications we have obtained a higher order for the third order nonlinear susceptibility, as mentioned before, the electrostriction effect is the main cause for this change in order for the optical constants.

From angle-resolved light scattering technique we have demonstrated that the scattering indicatrix, surface power spectral density and autocorrelation function demonstrate a distinctive change during the phase transition. Light scattering measurements show that the elastic strain affects the thermal transition from insulating to metallic. These effects result in a temperature dependent twinning of microcrystallites and the formation of domains for temperatures below the phase transition. For a 30 nm thick VO_2/Al_2O_3 (R-cut) film at the critical temperature of $T_C = 341\,K$ the surface autocorrelation length drops to its minimum value and disorder of the film reaches its highest level due to the coexistence of both insulating and metallic phases. After VO_2 goes into its metallic phase the autocorrelation length recovers back, close to its initial value in the insulating phase. Along the phase transition the fractal dimension of the surface decreases, this in turn is an indication of a smoother surface with more uniform optical properties in the metallic phase.

Form ultrafast light scattering we have shown the evolution of multiscale photo induced optical inhomogeneities in VO_2 films during the ultrafast phase transition. The transient surface statistics and mesoscale structural PT are noticeably different for epitaxial and non-epitaxial films. The non-stoichiometry and higher concentration of structural defects in the smallest VO_2 grains of the non-epitaxial film both result in non-uniform metallic phase nucleation.

Appendix

A.1 Beam waist radius parameter extraction program.

```
clc, close all, clear all

nrow=1920;                %%%these first three columns are for creating the
dimensions of the matrix that will include the data of the image.
ncolumn=2560;             %%If you have an image with different dimensions
then just change the numbers of the
n=nrow*ncolumn;
 %imshow('16bits_bmp_bw_Filter740__fp_et_15ms_0.bmp') %it will output the
image that is reading

z=imread('2_16bits_bmp_bw_Filter600_0.bmp'); %transfer the data from the
image the variable z.

p= z(:,:,2);            %p have the picture information from the second layer
(Green=G) of the RGB format.
                        %For black and white pictures all layers should have
the same data.
[R, C]= det_max(p);   %Call the user define function 'det_max' to determine
the row=R and column=C that have the peak of intensity in the picture.

        %%%%%%%%%
%This section includes the matrix that works as x for the fitting function
rowtofit= p(R,:);
rowtofit=rowtofit';
coltofit=p(:,C);
rowx=1:1:size(rowtofit);
rowx=rowx';
rowx=rowx*2.199074;  %it is mmultiply by the pixel size in microns
(horizontal mesuarement of the pixel)
colx= 1:1:size(coltofit);
colx=colx';
colx=colx*2.201646;       %it is mmultiply by the pixel size in
microns(vertical mesuarement of the pixel)

%%%%%%%%%%%%%%%%%%%%%%%%%%%%%%%%%%%%%%%%%%
%This section fits the data from the column with the maximum peak,
y0c=0% mode(coltofit); %vertical displacement of the data
col=coltofit-y0c; % data use for fitting
[columnfit, cfitdata]= fit(colx,col, 'gauss1');
colparamval=coeffvalues(columnfit); %%%Extract parameters from 'columnfit'.
w_column=colparamval(3); % Gives 'w' parameter from 'columnfit'.
A_column=colparamval(1); %Gives 'A' parameter from 'columnfit'.
recalculated_waist_radius_column=sqrt(2*(w_column.^2)); %This is the waist
radius of the beam in microns from 'columnfit' data.
waist_column_amplitude= A_column/(exp(2));
figure (18)
plot(columnfit,colx, coltofit);
columnfit; %will output the values of the parameters of 'columnfit' and other
infromation of the fitting.
```

```
cfitdata ; %will output the values of the parameters of 'columnfit' and other
infromation of the fitting.
            %%%%%%%
%This section fit the data from the row with the maximum peak.
y0r=0% mode(rowtofit); % vertical displacement of the data
row= rowtofit-y0r; % data use for fitting
[rowfit,rfitdata]= fit(rowx, row, 'gauss1');
rowparamval=coeffvalues(rowfit);  %%%Extract parameters from 'rowfit'.
w_row=rowparamval(3);  % Gives 'w' parameter from 'rowfit'.
A_row=rowparamval(1);  % Gives 'A' parameter from 'rowfit'.
recalculated_waist_radius_row= sqrt(2*(w_row.^2)); %This is the waist radius
of the beam in microns from 'rowfit' data.
figure(19);
plot(rowfit,rowx,rowtofit);
rowfit ;  %will output the values of the parameters of 'rowfit' and other
infromation of the fitting.
rfitdata; %will output the values of the parameters of 'rowfit' and other
infromation of the fitting.

average_WR=
(recalculated_waist_radius_column+recalculated_waist_radius_row)/2;
%%%%%%%%%%%%%%%%%%%%%%%%%%%%%%%%%
%[w,gaussfit_data]=gauss_zscan(colx,coltofit)


% % % % This is an incomplete userdefine funtion for the gaussian profile.
% % % % It would output the waist radius without the need of recalculation.
% % % % However I could not finished. (may be wrong)
% % gauss_2= fittype(@(A,xc,w,x) A*exp(-2*((x-xc)/w).^2),...
% %                     'coefficients', {'A', 'xc','w'});
% % %           A=max(coltofit);
% % %           xc= C;
% % f= fit(colx, coltofit, gauss_2);
% % plot (f, colx,coltofit);
% % figure(25);
% % %%%%%%%%%%%%%%%%%%%%%%%%%%%%
```

A.2 Power, Intensity and Fluence extraction program.

```
%%%Power, Peak Power, Intensity and Fluence Extraction%%%


Energy=0.246E-9; %Energy of laser given by Molectron in Joules
%AveragePower= 0.244E-6; %Average Power of laser given by Molectron in Watts
Pulsewidth= 30E-12; %Pulse width of laser in seconds
RepetitionRate= 10; %Repetition rate of laser in hertz
lambda= 532E-9; %wavelenght of laser in meters
w0= 8.70E-6; %beam waist radius in meters
T10= 0.7330;       %
T20= 0.5871;          %
T30= 0.4246;      %
T40= 0.3389;       %
T50= 0.2630;       %
T60= 0.1865;       %
T80= 0.1408;       %
T100= 0.1176;      %
T200= 0.0208;      %Transmittance value of filters
T400= 0.0094;      %
T1= 0.1100;        %
T3= 0.0019;      %
TNG3= 0.0154 ;     %
TNG9= 0.0080;     %
TNG10= 0.00153;   %


Area= pi*(w0^2); %area of cirlce in m^2
E= Energy/T3;
PeakPower= (0.94*E)/(Pulsewidth) %Peak Power for gaussian shaped pulses in
Watts
I0= 2*PeakPower/Area; %Intesity of laser in Watts/m^2 after calibration
filter
%I0= Intensity/((T200)*(T100)); %Original Intensity in Watts/m^2
Ifocus= I0*T60 %Intensity at sample after filter in Watts/m^2
%Fluence= Ifocus*Pulsewidth %Fluence in J/m^2
Efocus= E*T60;  %Energy of laser at sample after filter in J
Fluence= Efocus/Area %J/m^2
Fluence2 = Fluence*0.1 %Fluence in mJ/cm^2

%z0= (pi*(w0)^2)/lambda
```

A.3 Z-scan parameter extraction program.

```
%%%%%%Parameter extraction Program%%%%%%%%%

%%%% Universal Constant

e0= 8.855E-12; %(C^2 N^-1 m^-2), permitivity of free space
c= 3E8; % (m/s), speed of light in vacum
h= 6.63E-34; % (J/s), Planck constant
h_reduced= h/(2*pi); %(J s^-1 rad^-1), reduced planck constant


%%%% parameter that are constant

lambda= 532E-9; % (m), wavelength of laser
Ifocus= 1.28E13; % (W/ m^2), irradiance at focus
w0= 8.7E-6; % (m), waist raidius of the beam at focus
F0= 205.53; % (2*en0)/(pi*(w0^2)) %(J/m^2), fluence at focus
L= 55E-9; % (m), thickness of sample
n0= 2.7 ; %  linear index of refraction
alpha= 1.75E7 ; %(m^-1), linear absorption coeficient
p= 4.57E6; % (g/m^3), density
Cv= 0.656; % (J/(g*K)), especific heat;
%%%% Equations
w= (2*pi*c)/lambda;
k= (2*pi)/lambda; % (rad/m), wave vector
q0= 0.38 ; % parameter extracted from open aperture fit
Df= 1.66 ; % parameter extracted from close aperture fit
%  Tpv= 0.39; % parameter extracted from close aperture scan
%  Df= Tpv/(0.406*((1-.05)^0.25));
Leff= (1-exp(-(alpha*L)))/alpha; % (m), effective lenght of sample



betta=q0/(Ifocus*Leff) % (m/W), nonlinear absorption coefficient
sigmar= (Df*h_reduced*2*w)/(alpha*Leff*F0) % (m^2)
sigmaexc= (q0*2*h_reduced*w)/(alpha*F0*Leff) %(m^2), excited state absorption
cross-section

gamma= (Df/(Ifocus*k*Leff)) %(m^2/W), nonlinear index of refraction
n2_esu= (c*n0*gamma)/(40*pi)
n2eff_esu=sqrt(2)*n2_esu
avg_delta_n0= (gamma*Ifocus)/(sqrt(2)); %averege on-axis nonlinear index
change
dNdT= (avg_delta_n0*2*p*Cv*10000)/(F0*alpha) % (1/K), thermo-optic
coefficient

Xr= (4/3)*((n0)^(2))*e0*c*gamma % (m^2/V^2), real part of third order
suceptibility
Xresu= Xr* 7.068E8 % Real part in esu
Xi= ((n0^2)*betta*e0*(c^2))/w % (m^2/V^2), imaginary part of third order
suceptibility
Xiesu= Xi* 7.06E8 % Imaginary part in esu
```

```
X3= sqrt((Xr^2) + (Xi^2)) % (m^2/V^2), Third order suceptibility
X3esu= sqrt((Xresu^2) + (Xiesu^2))  % (esu), Third order suceptibility
```

Bibliography

[1] U. Kürüm, R. M. Öksüzoğlu, M. Yüksek, H. G. Yaglioglu, H. Çınar, and A. Elmali, Appl. Phys. A **104**, 1025 (2011).

[2] F. J. Morin, Phys. Rev. Lett. **3**, 34 (1959).

[3] S. Lysenko, F. Fernández, A. Rúa, J. Aparicio, N. Sepúlveda, J. Figueroa, K. Vargas, and J. Cordero, J. Appl. Phys. **117**, 184304 (2015).

[4] S. Lysenko, V. Vikhnin, F. Fernandez, a. Rua, and H. Liu, Phys. Rev. B - Condens. Matter Mater. Phys. **75**, 1 (2007).

[5] A. Cavalleri, C. Tóth, C. W. Siders, J. A. Squier, F. Ráksi, P. Forget, and J. C. Kieffer, Phys. Rev. Lett. **87**, 237401 (2001).

[6] M. S. Bahae, a a Said, T. H. Wei, D. J. Hagan, and E. W. Van Stryland, IEEE J. Quantum Electron. **26**, 760 (1990).

[7] S. Lysenko, a. Rua, F. Fernandez, and H. Liu, J. Appl. Phys. **105**, 1 (2009).

[8] V. Eyert, Ann. Phys. **11**, 650 (2002).

[9] J. M. Longo and P. Kierkegaard, Acta Chem. Scand. **24**, 420 (1970).

[10] R. M. Wentzcovitch, W. W. Schulz, and P. B. Allen, Phys. Rev. Lett. **72**, 3389 (1994).

[11] H. W. Verleur, A. S. Barker, and C. N. Berglund, Rev. Mod. Phys. **40**, 737 (1968).

[12] W. R. Roach and I. Balberg, Solid State Commun. **9**, 551 (1971).

[13] F. A. Bugaev, A.A.; Gudyalis, V.V.; Zakharchenya, B.P.; Chudnovskii, 3 (1982).

[14] H. Liu, O. Vasquez, V. R. Santiago, L. Diaz, and F. E. Fernandez, J. Lumin. **108**, 233 (2004).

[15] G. I. Petrov, V. V Yakovlev, and J. a Squier, Opt. Lett. **27**, 655 (2002).

[16] A. Cavalleri, H. H. W. Chong, S. Fourmaux, T. E. Glover, P. A. Heimann, J. C. Kieffer, B. S. Mun, H. A. Padmore, and R. W. Schoenlein, Phys. Rev. B - Condens. Matter Mater. Phys. **69**, 1 (2004).

[17] J.-F. Xu, R. Czerw, S. Webster, D. L. Carroll, J. Ballato, and R. Nesper, Appl. Phys. Lett. **81**, 1711 (2002).

[18] R. Lopez, R. F. Haglund, L. C. Feldman, L. a Boatner, and T. E. Haynes, Appl. Phys. Lett. **85**, 5191 (2004).

[19] P. U. Jepsen, B. M. Fischer, A. Thoman, H. Helm, J. Y. Suh, R. Lopez, and R. F. Haglund, Phys. Rev. B - Condens. Matter Mater. Phys. **74**, 1 (2006).

[20] H. T. Kim, Y. W. Lee, B. J. Kim, B. G. Chae, S. J. Yun, K. Y. Kang, K. J. Han, K. J. Yee, and Y. S. Lim, Phys. Rev. Lett. **97**, 10 (2006).

[21] M. S. Grinolds, V. A. Lobastov, J. Weissenrieder, and A. H. Zewail, Proc. Natl. Acad. Sci. **103**, 18427 (2006).

[22] P. Baum, D.-S. Yang, and A. H. Zewail, Science (80-.). **318**, 788 (2007).

[23] C. Kubler, H. Ehrke, R. Huber, R. Lopez, A. Halabica, R. F. Haglund, and A. Leitenstorfer, Phys. Rev. Lett. **99**, 1 (2007).

[24] D. J. Hilton, R. P. Prasankumar, S. Fourmaux, A. Cavalleri, D. Brassard, M. A. El Khakani, J. C. Kieffer, A. J. Taylor, and R. D. Averitt, Phys. Rev. Lett. **99**, 1 (2007).

[25] S. Lysenko, a. Rúa, V. Vikhnin, F. Fernández, and H. Liu, Phys. Rev. B **76**, 1 (2007).

[26] S. Lysenko, V. Vikhnin, a. Rúa, F. Fernández, and H. Liu, Phys. Rev. B - Condens. Matter Mater. Phys. **82**, 1 (2010).

[27] M. Nakajima, N. Takubo, Z. Hiroi, Y. Ueda, and T. Suemoto, Appl. Phys. Lett. **92**, 011907 (2008).

[28] M. Hada, K. Okimura, and J. Matsuo, Phys. Rev. B - Condens. Matter Mater. Phys. **82**, 2 (2010).

[29] A. Pashkin, C. K??bler, H. Ehrke, R. Lopez, A. Halabica, R. F. Haglund, R. Huber, and A. Leitenstorfer, Phys. Rev. B - Condens. Matter Mater. Phys. **83**, 1 (2011).

[30] M. Hada, K. Okimura, and J. Matsuo, Appl. Phys. Lett. **99**, 1 (2011).

[31] B. Wang, S. Chen, Z. Huang, and M. Fu, Appl. Surf. Sci. **258**, 5319 (2012).

[32] Z. Tao, T.-R. Han, S. Mahanti, P. Duxbury, F. Yuan, C.-Y. Ruan, K. Wang, and J. Wu, Phys. Rev. Lett. **109**, 1 (2012).

[33] T. L. Cocker, L. V. Titova, S. Fourmaux, G. Holloway, H. C. Bandulet, D. Brassard, J. C. Kieffer, M. A. El Khakani, and F. A. Hegmann, Phys. Rev. B - Condens. Matter Mater. Phys. **85**, 1 (2012).

[34] S. Wall, D. Wegkamp, L. Foglia, K. Appavoo, J. Nag, R. F. H. Jr, J. Stähler, and M. Wolf, 1 (1807).

[35] S. Wall, L. Foglia, D. Wegkamp, K. Appavoo, J. Nag, R. F. Haglund, J. St??hler, and M. Wolf, Phys. Rev. B - Condens. Matter Mater. Phys. **87**, 1 (2013).

[36] M. Van Veenendaal, Phys. Rev. B - Condens. Matter Mater. Phys. **87**, 1 (2013).

[37] H. Liu, O. H. Kwon, J. Tang, and A. H. Zewail, Nano Lett. **14**, 946 (2014).

[38] W. P. Hsieh, M. Trigo, D. A. Reis, G. Andrea Artioli, L. Malavasi, and W. L. Mao, Appl. Phys. Lett. **104**, 1 (2014).

[39] D. Wegkamp, M. Herzog, L. Xian, M. Gatti, P. Cudazzo, C. L. McGahan, R. E. Marvel, R. F. Haglund, A. Rubio, M. Wolf, and J. Stähler, Phys. Rev. Lett. **113**, 2 (2014).

[40] K. Appavoo, B. Wang, N. F. Brady, M. Seo, J. Nag, R. P. Prasankumar, D. J. Hilton, S. T. Pantelides, and R. F. Haglund, Nano Lett. **14**, 1127 (2014).

[41] S. Lysenko, F. Fernández, A. Rúa, and H. Liu, J. Appl. Phys. **114**, (2013).

[42] R. Yoshida, T. Yamamoto, Y. Ishida, H. Nagao, T. Otsuka, K. Saeki, Y. Muraoka, R. Eguchi, K. Ishizaka, T. Kiss, S. Watanabe, T. Kanai, J. Itatani, and S. Shin, Phys. Rev. B - Condens. Matter Mater. Phys. **89**, (2014).

[43] S. Lysenko, F. Fern, R. Armando, N. Sep, and J. Aparicio, 1 (2014).

[44] B. Mayer, C. Schmidt, A. Grupp, J. B??hler, J. Oelmann, R. E. Marvel, R. F. Haglund, T. Oka, D. Brida, A. Leitenstorfer, and A. Pashkin, Phys. Rev. B - Condens. Matter Mater. Phys. **91**, 1 (2015).

[45] A. Grupp, B. Mayer, C. Schimdt, J. Oelmann, R. E. Marvel, R. F. Haglund, A. Leitenstorfer, and A. Pashkin, Springer Proc. Phys. **162**, 572 (2015).

[46] Y. Xiao, Z. H. Zhai, Q. W. Shi, L. G. Zhu, J. Li, W. X. Huang, F. Yue, Y. Y. Hu, Q. X. Peng, and Z. R. Li, Appl. Phys. Lett. **107**, 0 (2015).

[47] J. Lourembam, A. Srivastava, C. La-O-Vorakiat, H. Rotella, T. Venkatesan, and E. E. M. Chia, Sci. Rep. **5**, 9182 (2015).

[48] P. N. Prasad and D. J. Williams, *Introduction to Nonlinear Optical Effects in Molecules and Polymers*, 1st ed. (John Wiley & Sons, Inc, 1991).

[49] R. W. Boyd, *Nonlinear Optics*, 2nd ed. (Academic Press, 2003).

[50] J. R. Fienup, Appl. Opt. **21**, 2758 (1982).

[51] P. R. Willmott and J. R. Huber, Rev. Mod. Phys. **72**, 315 (2000).

[52] D. P. Norton, Y. W. Heo, M. P. Ivill, K. Ip, S. J. Pearton, M. F. Chisholm, and T. Steiner, Mater. Today **7**, 34 (2004).

[53] S. Lysenko, http://fisica.uprm.edu/light/Facilities (2015).

[54] Continuum, (1991).

[55] H. G. Tompkins, *Handbook of Ellipsometry* (2005).

[56] Y. Z. Gu, F. X. Gan, S. Q. Wang, and H. J. Xu, Opt. Commun. **197**, 501 (2001).

[57] W. Qu-Quan, S. Jing, Y. Bai-Feng, L. Hai-Lin, X. Gui-Guang, G. Qi-Huang, and X. Qi-Kun, Chinese Phys. Lett. **19**, 677 (2002).

[58] V. Singh, P. Aghamkar, and B. Lald, Acta Phys. Pol. A **123**, 39 (2013).

[59] M. D. Dvorak, B. L. Justus, and A. D. Berry, Opt. Commun. **116**, (1995).

[60] S. Hernández, P. Pellegrino, A. Martínez, Y. Lebour, B. Garrido, R. Spano, M. Cazzanelli, N. Daldosso, L. Pavesi, E. Jordana, and J. M. Fedeli, J. Appl. Phys. **103**, 064309 (2008).